

Dark Matter Working Group

recommendation for Two Higgs Doublet

Model (draft title)

Authorlist to be compiled: **Antonio Boveia,**^{3,*}
Caterina Doglioni,^{8,*} **Kristian Hahn,**^{14,*} **Ulrich Haisch,**^{15,16,*} **Steven**
Lowette,²² **Tim M.P. Tait,**^{25,*}

*DMWG organizers

³Ohio State University, 191 W. Woodruff Avenue Columbus, OH 43210

⁸Fysiska institutionen, Lunds universitet, Lund, Sweden

¹⁴Department of Physics and Astronomy, Northwestern University, Evanston, Illinois 60208,
USA

¹⁵Rudolf Peierls Centre for Theoretical Physics, University of Oxford, Oxford, OX1 3PN,
United Kingdom

¹⁶CERN, TH Department, CH-1211 Geneva 23, Switzerland

²²Physics Department, Vrije Universiteit Brussel, Brussels, Belgium

²⁵Department of Physics and Astronomy, University of California, Irvine, California 92697,
USA

Editor's E-mail: antonio.boveia@cern.ch, caterina.doglioni@cern.ch,
kristian.hahn@cern.ch, ulrich.haisch@physics.ox.ac.uk, ttait@uci.edu

Abstract. Draft abstract.

Contents

1	Introduction	1
2	The model	2
2.1	Evolution of theories for Dark Matter searches at colliders	2
2.2	Scalar Model Description	4
3	Model parameters	7
3.1	Vacuum stability	10
4	Model kinematics and mapping to existing models	12
4.1	Description of experimental searches	12
4.1.1	Signatures including a Higgs boson	12
4.1.2	Signatures including a Z boson	12
4.1.3	Signatures including heavy flavor quarks	14
4.2	Kinematic distributions justifying the choice of parameter scan	14
4.2.1	Masses of the A , H , and a bosons (M_A , M_H , and M_a)	14
4.2.2	Mixing angle between the two pseudoscalars A and a ($\sin \theta$)	18
4.2.3	Ratio of the doublet vacuum expectation values ($\tan \beta$)	20
4.3	Comparison with existing pseudoscalar models and recasting of $\text{HF}+E_T^{\text{miss}}$ search results	22
5	Parameter grid	26
6	Sensitivity studies	29
6.1	Studies of the $h(bb) + E_T^{\text{miss}}$ signature	29
6.2	Studies of the $Z+E_T^{\text{miss}}$ signature	33
7	Sensitivity of the jet+E_T^{miss} signature	37
7.1	Other signatures	38
7.1.1	Resonant Production at Collider (Comparison)	38
8	Connection with cosmology	39
8.1	Pseudoscalar	39
8.2	Technical setup	39
8.3	Results	40
8.4	Scalar	42
9	Comparisons with non-collider experiments	48
9.1	Direct detection	48
9.1.1	Scalar	48
9.2	Pseudoscalar	49
9.3	Indirect detection	53

10 Conclusions	55
Appendix	55
A Details on MC generation	55
B Additional kinematic distributions	56
C Cross-section and acceptances for selected signatures	58
D Studies of other models of scalar sector	61
E Inert Doublet Model	61

1 Introduction

Reasoning behind this effort

- Simplified models only one signature at a time, sometimes not gauge invariant
- One step beyond this: less-simplified models
- Compare and confront different search sensitivity
- Combinations among different signatures
- Find new kinematic regimes / improve searches by exploring different signatures
- Still keeping the choice of model generic enough that this is reusable for theorists

Reasoning behind this effort

- Reasoning behind the choice of model
- Highlights more than one signature at a time, depending on parameters
- Leaves room for new unexplored kinematic signatures within existing searches (left for future work)
- Complete enough, still simplified so that one can choose grid planes
- Existing theory effort (HXSWG)

We investigate in detail the kinematics of three experimental signatures that are sensitive to this model:

- the Higgs+ E_T^{miss} signature, where the E_T^{miss} is produced by the decay of the pseudoscalar that couples to dark matter and the Higgs is produced either in association with this pseudoscalar or as a product of the decay of the second pseudoscalar;

- the $Z+E_T^{\text{miss}}$ signature, where the E_T^{miss} is produced by the decay of the pseudoscalar that couples to dark matter and the Z boson is either produced in association with this pseudoscalar or radiated by the heavy Higgs boson;
- the $t\bar{t}+E_T^{\text{miss}}$ signature, where pseudoscalar that couples to dark matter is produced in association with a $t\bar{t}$ pair or radiated by one of the top quarks.
-

The sensitivity of searches for this model in those signatures surpasses that of the jet+ E_T^{miss} searches, providing a motivation to explore their parameter space beyond the s -channel simplified models in [1].

Moreover, we identify a number of other signatures that have sensitivity to this model and can be studied in the future, such as ...

2 The model

Description of the model

- Citations: [2–6]
- Particles, masses, couplings, mixing angles

Comparison with existing models How does the model compare with other 2HDMs/scalar models (with and without DM).

- Scalar to SSM to 2HDM evolution
- Other models:
 - S. Ipek, D. McKeen, A. Nelson, [4]
 - Bell, Busoni, Sanderson, [3]
 - No, Goncalves, Machado, [5, 6]
 - Higgs Cross-section Working Group

2.1 Evolution of theories for Dark Matter searches at colliders

For two of the three Dark Matter search strategies -direct and indirect detection- experimental results are presented in terms of effective field theories (EFTs). The operators in these EFTs are build from SM fermions and Dark Matter fields,

$$\mathcal{L}_{\text{EFT}} = \sum_{f=u,d,\ell} \left(\frac{C_1^f}{\Lambda^2} \bar{f} f \bar{\chi} \chi + \frac{C_2^f}{\Lambda^2} \bar{f} f \bar{\chi} \gamma^5 \chi + \frac{C_3^f}{\Lambda^2} \bar{f} \gamma^5 f \bar{\chi} \chi + \frac{C_4^f}{\Lambda^2} \bar{f} \gamma^5 f \bar{\chi} \gamma^5 \chi + \dots \right), \quad (2.1)$$

where χ denotes a Dirac fermion DM candidate and the sum over $f = u, d, \ell$ extends over SM quarks and leptons. The EFT is fully described by the parameters

$$\{m_\chi, \Lambda, C_i^f\}, \quad (2.2)$$

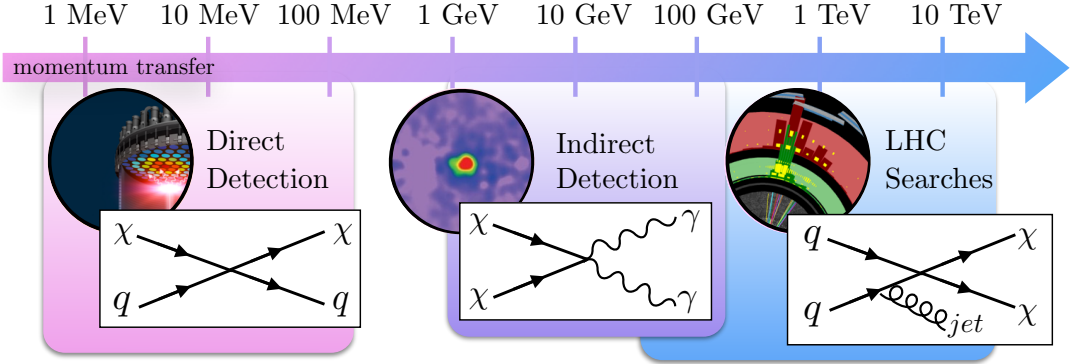


Figure 1: Range of momenta probed in Direct Detection experiments, Indirect Detection experiments and LHC searches for weak scale Dark Matter candidates.

where m_χ is the mass of the DM candidate. This ansatz is justified for the small momentum transfer $q^2 \ll \Lambda^2$ in DM-nucleon scattering (set by the non-relativistic velocities of DM in the halo) and in DM annihilation (set by the mass of the annihilating DM candidate), illustrated in Fig. 1. Early papers on DM searches at colliders refer to these EFTs to quantify the reach of the LHC in the parameter space defined by (2.2) [7–9]. The momentum transfer accessible at the LHC is larger than the suppression scale $\Lambda \ll q_{\text{LHC}}^2$ for many theories of DM. In this case, the mediator of the interaction between the dark sector and the SM can be resonantly produced and predictions derived from the EFT framework are bound to fail [0]. The kinematics of on-shell propagators can be captured in simplified models, which aim to represent a large number of extensions of the SM, while keeping only the degrees of freedom relevant for LHC phenomenology. In the case of a pseudoscalar mediator the corresponding interactions between DM, SM fermions and the mediator a read

$$\mathcal{L}_{\text{simp}} = -i g_\chi a \bar{\chi} \gamma_5 \chi - i a \sum_i \left(g_u y_i^u \bar{u}_i \gamma_5 u_i + g_d y_i^d \bar{d}_i \gamma_5 d_i + g_\ell y_i^\ell \bar{\ell}_i \gamma_5 \ell_i \right), \quad (2.3)$$

in which i is a flavour index. In addition, there is the scalar potential including a potential Higgs portal

$$V(H, a) = \frac{1}{2} m_a^2 a^2 + b_a a H^\dagger H + \lambda_{H a} a^2 H^\dagger H + \lambda a^4. \quad (2.4)$$

The Higgs portal is generally considered irrelevant, otherwise there are constraints from Higgs coupling strength measurements and of the Higgs CP property stronger than all limits from searches for DM at the LHC [0]. The quartic couplings in (2.4) are not relevant for collider searches for DM. This simplified model is therefore fully described by the parameters

$$\{m_\chi, m_a, g_\chi, g_u, g_d, g_\ell\}, \quad (2.5)$$

and matches to the EFT (2.1) with $C_4^f/\Lambda^2 = g_\chi g_f y_f/m_a^2$ and $C_i^f = 0$ for all other Wilson coefficients, but retains the full momentum dependence of the pseudoscalar propagator.

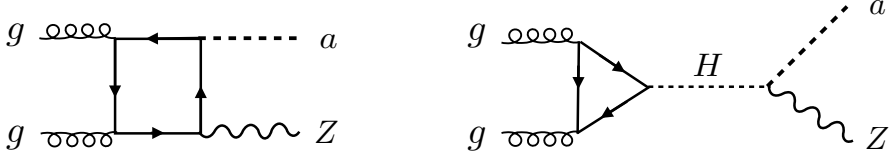


Figure 2: Feynman diagrams contributing to $\sigma(pp \rightarrow aZ)$ in the simplified model with a pseudoscalar singlet mediator a (left) and in the 2HDM+ a model (right).

The operators in both \mathcal{L}_{EFT} and $\mathcal{L}_{\text{simp}}$ violate gauge invariance, because of the chiral SM fermions. In the case of the EFT this suggests the scaling of the Wilson coefficients $C_i^f = c_i^f m_{f_i} / \Lambda$ [], whereas for the simplified model restoring gauge invariance requires the embedding of the mediator a into an electroweak multiplet. The absence of gauge invariance leads to unitarity violating amplitudes. For example on the left of Fig. 2, we show the diagram contributing to the amplitude for the production of the pseudoscalar mediator in association with a Z -boson, which diverges with the center-of-mass energy $\mathcal{M}(pp \rightarrow Za) \propto \log^2(s)$ in the simplified model, signaling the omission of additional diagrams. Since this divergence is only logarithmic, the simplified model does not break down for the energies accessible at the LHC []. More importantly, the additional degrees of freedom necessary to unitarize the amplitudes cannot be arbitrarily heavy and change the phenomenology of the simplified model significantly. For example, the $pp \rightarrow Za$ cross section can be made finite by the exchange an additional scalar H with a coupling to a and Z , and the corresponding diagram is shown on the right of Fig. 2. Since resonant production is strongly enhanced compared to initial state radiation, the hierarchy of initial state mono- X signals, mono-jet > mono-photon > mono- Z > mono-Higgs, can be turned upside-down with different kinematics requiring adapted experimental search strategies. The embedding of the pseudoscalar mediator model (2.3) is not unique. Both the mediator and the DM can be embedded in different electroweak multiplets, resulting in additional model-dependent and model-independent signals []. In this whitepaper, we consider the simplest embedding with a single SM-singlet DM candidate, which captures the maximal number of interesting signatures.

2.2 Scalar Model Description

We shall consider a Dirac DM candidate, χ , and expand the scalar sector of the SM to include two Higgs doublets, Φ_1 and Φ_2 , in addition to a real singlet scalar field, S . Following the discussion in [10], we outline the scalar potential which controls the mixing between the CP even scalars, and the Yukawa structure which dictates the coupling of those scalars to the DM and SM fermions.

It is convenient to rotate $\{\Phi_1, \Phi_2\}$ to the Higgs basis $\{\Phi_h, \Phi_H\}$, which is defined such that only one of the two doublets obtains a vev. Taking $\langle \Phi_H \rangle = 0$ and $\langle \Phi_h \rangle = v \sim 246$ GeV, the two Higgs doublets are then defined by

$$\Phi_h = \cos \beta \Phi_1 + \sin \beta \Phi_2 = \begin{pmatrix} G^+ \\ \frac{v+h+iG^0}{\sqrt{2}} \end{pmatrix}, \quad (2.6)$$

$$\Phi_H = -\sin \beta \Phi_1 + \cos \beta \Phi_2 = \begin{pmatrix} H^+ \\ \frac{H+iA}{\sqrt{2}} \end{pmatrix}. \quad (2.7)$$

The scalar potential consists of the usual 2HDM potential, augmented by terms involving the new singlet scalar S . We will assume that the scalar potential has a spontaneously broken \mathbb{Z}_2 symmetry for the particle S . This may arise naturally, for example, in the case where S is part of a complex scalar charged under a dark $U(1)$ gauge group. The scalar potential is thus given by

$$\hat{V}(\Phi_h, \Phi_H, S) = \hat{V}_{2\text{HDM}}(\Phi_h, \Phi_H) + \hat{V}_S(S) + \hat{V}_{S2\text{HDM}}(\Phi_h, \Phi_H, S), \quad (2.8)$$

where

$$\begin{aligned} \hat{V}_{2\text{HDM}}(\Phi_h, \Phi_H) &= \hat{M}_{hh}^2 \Phi_h^\dagger \Phi_h + \hat{M}_{HH}^2 \Phi_H^\dagger \Phi_H + (\hat{M}_{hH}^2 \Phi_H^\dagger \Phi_h + h.c.) + \frac{\hat{\lambda}_h}{2} (\Phi_h^\dagger \Phi_h)^2 + \frac{\hat{\lambda}_H}{2} (\Phi_H^\dagger \Phi_H)^2 \\ &\quad + \hat{\lambda}_3 (\Phi_h^\dagger \Phi_h) (\Phi_H^\dagger \Phi_H) + \hat{\lambda}_4 (\Phi_H^\dagger \Phi_h) (\Phi_h^\dagger \Phi_H) + \frac{\hat{\lambda}_5}{2} ((\Phi_H^\dagger \Phi_h)^2 + h.c.), \end{aligned} \quad (2.9)$$

$$\hat{V}_S(S) = \frac{1}{2} \hat{M}_{SS}^2 S^2 + \frac{1}{4} \hat{\lambda}_S S^4, \quad (2.10)$$

$$\hat{V}_{S2\text{HDM}}(\Phi_h, \Phi_H, S) = \frac{\hat{\lambda}_{HHS}}{2} (\Phi_H^\dagger \Phi_H) S^2 + \frac{\hat{\lambda}_{hhs}}{2} \Phi_h^\dagger \Phi_h S^2 + \frac{1}{2} (\hat{\lambda}_{hHS} \Phi_H^\dagger \Phi_h S^2 + h.c.). \quad (2.11)$$

In general, there would be mass mixing between all three neutral CP even scalars of the model, h , H , and S . We shall, however, impose a generalized Higgs “alignment limit” which decouples the SM Higgs, h , from the other two states. This is desirable because it reduces the scalar mixing to a 2-state problem and guarantees that h couples like the SM Higgs. We thus set

$$\hat{\lambda}_h = \hat{\lambda}_H = \hat{\lambda}_3 + \hat{\lambda}_4 + \hat{\lambda}_5, \quad (2.12)$$

$$\hat{\lambda}_{hhs} = 0, \quad (2.13)$$

where the first of these conditions is sufficient to impose alignment in a standard 2HDM, and the second clearly prevents h - S mixing (refer to [10] for further discussion of the alignment limit). The remaining H - S mass matrix is then diagonalized to obtain two mass eigenstate scalars, S_1 and S_2 , such that

$$H = \cos \theta S_1 - \sin \theta S_2, \quad (2.14)$$

$$S = v_S + \sin \theta S_1 + \cos \theta S_2, \quad (2.15)$$

where

$$\sin 2\theta = \frac{2\hat{\lambda}_{hHS} v v_S}{M_{S_1}^2 - M_{S_2}^2}. \quad (2.16)$$

The scalar mass spectrum then simplifies to

$$M_A^2 = M_{H^+}^2 + \left(\hat{\lambda}_4 - \hat{\lambda}_5 \right) \frac{v^2}{2}, \quad (2.17)$$

$$M_{S_{1,2}}^2 = \frac{1}{2} \left(M_A^2 + \hat{\lambda}_5 v^2 \right) \left(1 \pm \frac{1}{\cos 2\theta} \right) + \hat{\lambda}_S v_S^2 \left(1 \mp \frac{1}{\cos 2\theta} \right). \quad (2.18)$$

Model	ϵ_d	ϵ_u	ϵ_l
Type I	$\cot \beta$	$\cot \beta$	$\cot \beta$
Type II	$-\tan \beta$	$\cot \beta$	$-\tan \beta$
Type X	$\cot \beta$	$\cot \beta$	$-\tan \beta$
Type Y	$-\tan \beta$	$\cot \beta$	$\cot \beta$
Inert	0	0	0

Table 1: Values of the Yukawa scaling factors, $\epsilon_{u,d,l}$ which correspond to models with discrete Z_2 symmetries.

Taking h to be the observed SM Higgs boson then fixes $\hat{\lambda}_h$ and hence also fixes $\hat{\lambda}_H$ via the alignment condition (2.12). Using the previous equations, we can rewrite M_A and M_{H^+} as a function of $M_{S_{1,2}}$, θ , and $\hat{\lambda}_{4,5}$:

$$M_{H^+}^2 = M_{S_1}^2 \cos^2 \theta + M_{S_2}^2 \sin^2 \theta - (\hat{\lambda}_4 + \hat{\lambda}_5) \frac{v^2}{2}, \quad (2.19)$$

$$M_A^2 = M_{S_1}^2 \cos^2 \theta + M_{S_2}^2 \sin^2 \theta - \hat{\lambda}_5 v^2. \quad (2.20)$$

The only portal between the DM and other fields is via its Yukawa coupling to the singlet scalar,

$$\mathcal{L}_{\text{DM}} = -y_\chi S \bar{\chi} \chi. \quad (2.21)$$

We will assume that the DM particle has no bare mass term, and that its mass is instead generated by the vacuum expectation value of the singlet scalar, i.e. $m_\chi = y_\chi v_s$ with $\langle S \rangle = v_s$. Although this is not strictly necessary, such a scenario arises naturally if DM is a chiral fermion charged under some dark gauge group that is broken spontaneously by the vev of S . This assumption adds a constraint between the DM mass and the DM Yukawa coupling, removing the freedom to accommodate the relic density by varying these two parameters independently.

We will express the Yukawa interactions of the SM fermions with the Higgs doublets as

$$\mathcal{L}_{\text{Yukawa}} = - \sum_{n=h,H} \left(Y_{n,ij}^U \bar{Q}_L^i u_R^j \tilde{\Phi}_n + Y_{n,ij}^D \bar{Q}_L^i d_R^j \Phi_n + Y_{n,ij}^L \bar{L}_L^i l_R^j \Phi_n + h.c. \right), \quad (2.22)$$

and we will assume that the Yukawa matrices of the additional doublet are proportional to the SM ones:

$$Y_h^i \equiv Y_{\text{SM}}^i, \quad (2.23)$$

$$Y_H^i = \epsilon_i Y_{\text{SM}}^i, \quad (2.24)$$

where the ϵ_i are Yukawa scaling factors, with $i = u, d, l$. This Yukawa structure is the so-called Aligned Yukawa model [11–15], which satisfies Natural Flavour Conservation. In special cases where the ϵ_i satisfy certain relationships, the Aligned Yukawa structure can correspond to one of the Z_2 symmetric Yukawa structures (Type I, II, X or Y), as shown

in Table 1. While we will determine constraints for both Type I and Type II Yukawa structures, we will also include results for more general choices of the scaling factors that satisfy the Aligned Yukawa criteria. See [3] for a more detailed discussion of the Yukawa structure in these models.

3 Model parameters

The 2HDM+a model is a two Higgs doublet model with two scalar doublets H_1 and H_2 and an additional pseudoscalar singlet P . It is the simplest renormalizable extension of the simplified pseudoscalar mediator model with SM singlet Dark Matter, which makes the gauge symmetry manifest by coupling to the DM (here a Dirac fermion χ) with the singlet P

$$\mathcal{L}_\chi = -iy_\chi P\bar{\chi}\gamma_5\chi, \quad (3.1)$$

while the Higgs doublets couple to the SM fermions

$$\mathcal{L}_Y = -\sum_{i=1,2} \left(\bar{Q}Y_u^i \tilde{H}_i u_R + \bar{Q}Y_d^i H_i d_R + \bar{L}Y_\ell^i H_i \ell_R + \text{h.c.} \right). \quad (3.2)$$

The dominant mediator of interactions between the dark sector and the SM fermions is a superposition of the CP-odd component of H_1 , H_2 and P . We impose a Z_2 symmetry under which $H_1 \rightarrow H_1$ and $H_2 \rightarrow -H_2$, such that only one Higgs doublet appears in each operator in (3.2). The different ways to construct these operators result in different Yukawa coupling structures and we will remain as general as possible regarding this choice. The Z_2 symmetry is the minimal condition necessary to guarantee the absence of flavour-changing neutral currents (FCNCs) at tree-level [? ?] and such a symmetry is realized in many well-motivated complete ultraviolet theories in the form of supersymmetry, a $U(1)$ symmetry or a discrete symmetry acting on the Higgs doublets. We further choose all parameters in the scalar potential real, such that CP eigenstates are identified with the mass eigenstates, two scalars h and H , two pseudoscalars a and A , and a charged scalar H^\pm . Under these conditions, the most general scalar potential can be written as

$$V(P, H) = V_H + V_{PH} + V_P, \quad (3.3)$$

with the potential for the two Higgs doublets

$$\begin{aligned} V_H = & \mu_1 H_1^\dagger H_1 + \mu_2 H_2^\dagger H_2 + \left(\mu_3 H_1^\dagger H_2 + \text{h.c.} \right) + \lambda_1 (H_1^\dagger H_1)^2 + \lambda_2 (H_2^\dagger H_2)^2 \\ & + \lambda_3 (H_1^\dagger H_1)(H_2^\dagger H_2) + \lambda_4 (H_1^\dagger H_2)(H_2^\dagger H_1) + \left[\lambda_5 (H_1^\dagger H_2)^2 + \text{h.c.} \right], \end{aligned} \quad (3.4)$$

potential terms which connect doublets and singlets

$$V_{HP} = P \left(ib_P H_1^\dagger H_2 + \text{h.c.} \right) + P^2 \left(\lambda_{P1} H_1^\dagger H_1 + \lambda_{P2} H_2^\dagger H_2 \right), \quad (3.5)$$

and the singlet potential

$$V_P = \frac{1}{2} m_P^2 P^2 + \lambda_P P^4. \quad (3.6)$$

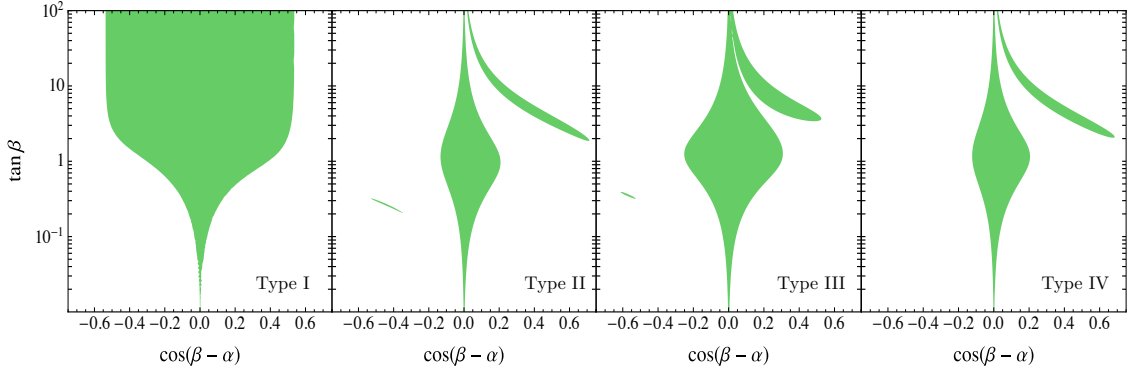


Figure 3: Parameter space allowed by a global fit to Higgs coupling strength measurements for (from left to right) a Yukawa sector of type I ($Y_u^1 = Y_d^1 = Y_\ell^1 = 0$), type II ($Y_u^1 = Y_d^2 = Y_\ell^2 = 0$), type III ($Y_u^1 = Y_d^1 = Y_\ell^2 = 0$), and type IV ($Y_u^1 = Y_d^2 = Y_\ell^1 = 0$).

Upon rotation to the mass eigenbasis, we trade the five dimensionful and eight dimensionless parameters in the potential for physical masses and mixing angles and three quartic couplings

$$\left\{ \begin{array}{l} \mu_1, \mu_2, \\ \mu_3, m_P^2, b_P \\ \lambda_1, \lambda_2, \lambda_3, \lambda_4, \lambda_5 \\ \lambda_{P1}, \lambda_{P2}, \lambda_P \end{array} \right\} \longleftrightarrow \left\{ \begin{array}{l} v, M_h, \cos(\beta - \alpha) \\ M_a, M_A, M_H, M_{H^\pm} \\ t_\beta, \cos(\theta), \\ \lambda_3, \lambda_{P1}, \lambda_{P2}, \lambda_P \end{array} \right\}. \quad (3.7)$$

Out of these parameters, the electroweak scale $v = 246$ GeV and the mass of the SM-like CP-even mass eigenstate $M_h = 125$ GeV are fixed. The mixing angle α between the CP-even scalars h and H is constrained by Higgs coupling strength measurements [1] and we show the allowed parameter space in the $\cos(\beta - \alpha)$ plane in Fig. 3 for the Yukawa sector of a 2HDM of type II. For arbitrary values of $t_\beta = v_2/v_1$ only the limit $\cos(\beta - \alpha) \approx 0$ is allowed, for which the couplings of the CP-even state h align with the couplings of the SM Higgs boson. For the analyses discussed in the remainder of this paper, we choose this so-called alignment limit and treat t_β as a free parameter. Electroweak precision measurements constrain the splitting between the masses M_H, M_A, M_a and M_{H^\pm} , since loops of spin-0 states modify the propagators of the electroweak gauge bosons at one-loop. For $M_H = M_{H^\pm}$ and $\cos(\beta - \alpha) = 0$, these corrections vanish due to a custodial symmetry in the tree-level potential V_H [1] and the masses of the CP-odd mass eigenstates can be treated as free parameters. This custodial symmetry is also present in V_H if $M_A = M_{H^\pm}$ and $\cos(\beta - \alpha) = 0$, but the presence of the pseudoscalar mixing term in V_P softly breaks this symmetry. As a consequence, the pseudoscalar mixing angle θ and the mass splitting between M_H, M_A and M_a are constrained in this situation. In Fig. ??... Flavour observables are mostly sensitive to corrections from one-loop exchanges of the charged scalar H^\pm , whose contributions to $b \rightarrow X_s \gamma$ [2, 3, 4] and $B_s - \bar{B}_s$ mixing [5, 6, 7, 8] lead to the strongest indirect constraints on M_{H^\pm} . Since the couplings of the charged scalar

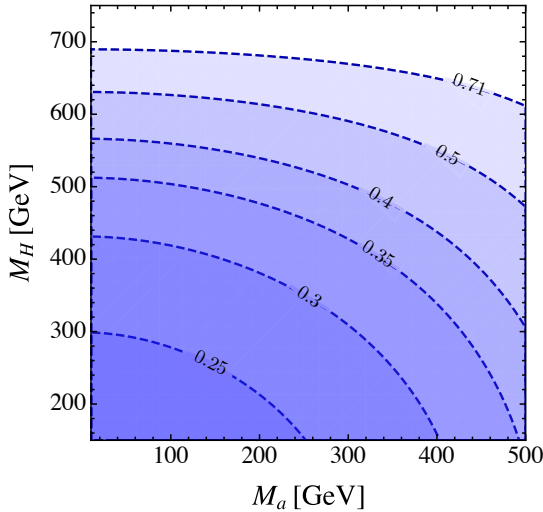


Figure 4: Values of M_H and M_a allowed by electroweak precision constraints for $\cos(\beta - \alpha) = 0$, $M_{H^\pm} = M_A = 750$ GeV, and varying values of the pseudoscalar mixing angle $\sin \theta = 0.25, 0.3, 0.35, 0.4, 0.5$, and maximal mixing angle $\sin \theta = 1/\sqrt{2} \approx 0.71$. The parameter space below and to the left of the dashed contours is excluded.

only depend on t_β , these constraints result in the bound $\tan \beta \gtrsim 0.8$ for $M_{H^\pm} = 750$ GeV, independent of the choice of the Yukawa sector.

In addition to these constraints, the potential V_H needs to give rise to a stable vacuum breaking the electroweak symmetry, whereas the parameters in V_P need not introduce a vacuum expectation value for P , and scattering amplitudes should remain perturbative [16, 17] and unitary [18? ? , 19] up to the UV scale, where the 2HDM+a is UV completed by a more complete theory. These conditions impose additional constraints on the quartic couplings in the potential, which are satisfied for $M_H, M_A, M_a \lesssim \mathcal{O}(1)$ TeV and $\lambda_3, \lambda_{P1}, \lambda_{P2}$ and λ_P of $\mathcal{O}(1)$ as long as t_β is not too much smaller than one. For the case of fixed¹ $\lambda_3, \lambda_{P1}, \lambda_{P2}$, the stability condition therefore leads to additional constraints on the mixing angle θ and the masses. The parameter space of the 2HDM+a is strongly constrained, as summarized below

$v, M_h, \cos(\beta - \alpha)$	\longleftrightarrow	fixed by Higgs measurements,
M_{H^\pm} ,	\longleftrightarrow	constrained by flavour observables,
$\sin(\theta), M_H$ or M_A	\longleftrightarrow	constrained EWPM,
$\lambda_3, \lambda_{P1}, \lambda_{P2}, \lambda_P$	\longleftrightarrow	constrained by stability, perturbativity and unitarity constraints .

This leaves us with effectively three free parameters from the potential, the Dark

¹The singlet quartic λ_P is entirely irrelevant for the phenomenology of the 2HDM+a.

Matter mass and the coupling of the mediator to the DM candidate

$$\{m_\chi, M_a, t_\beta, M_H \text{ or } M_A, y_\chi\}. \quad (3.8)$$

3.1 Vacuum stability

For extension of the Higgs sector (and in general for scalar extensions of the Standard Model) one needs to worry about boundedness from below of the scalar potential, as well as absolute stability of the electroweak minimum².

Regarding boundedness from below of the scalar potential in the present 2HDM + S model, we stress that provided that $\lambda_{P1}, \lambda_{P2} > 0$ in

$$V_P = \frac{1}{2} m_P^2 P^2 + \kappa (i P H_1^\dagger H_2 + \text{h.c.}) + \lambda_{P1} P^2 |H_1|^2 + \lambda_{P2} P^2 |H_2|^2,$$

the study of boundedness from below at tree-level reduces to the corresponding study in the 2HDM. The boundedness from below conditions in this case are well-known [16]:

$$\lambda_1 > 0, \lambda_2 > 0, \lambda_3 > -\sqrt{\lambda_1 \lambda_2}, \lambda_3 + \lambda_4 - |\lambda_5| > -\sqrt{\lambda_1 \lambda_2} \quad (3.9)$$

and can be inferred from analyzing the scalar potential at large field values $H_1, H_2 \gg v$. For $m_{H^\pm} = m_{H_0}$, the first two conditions in (3.9) may be simply written as

$$\frac{m_h^2}{v^2} (1 - t_\beta^2) + \lambda_3 t_\beta^2 > 0, \quad \frac{m_h^2}{v^2} (1 - t_\beta^{-2}) + \lambda_3 t_\beta^{-2} > 0 \quad (3.10)$$

which result in the requirement $\lambda_3 > m_h^2/v^2 = 0.258$. In figure 5 we show the regions of parameter space in the (m_a, m_{H_0}) (left) and (s_θ, m_a) (right) planes for which the tree-level boundedness from below conditions 3.9 are satisfied, assuming $m_{H^\pm} = m_{H_0} = m_{A_0}$.

Figure 5 shows that the region satisfying the tree-level boundedness from below conditions increases as λ_3 increases. At the same time, the choice $\lambda_3 = \lambda_{P1} = \lambda_{P2}$ which we adopt in the present analysis allows the increase in λ_3 not to affect the mono-Higgs sensitivity via a change in the coupling g_{aAh}

$$g_{aAh} = \frac{c_\theta s_\theta}{m_H v} [m_h^2 + m_H^2 - m_a^2 - 2(\lambda_3 - \lambda_{P1} c_\beta^2 - \lambda_{P2} s_\beta^2) v^2] = \frac{c_\theta s_\theta}{m_H v} [m_h^2 + m_H^2 - m_a^2] \quad (3.11)$$

We then fix the value $\lambda_3 = 3$ as benchmark for the rest of our analysis.

A few comments are in order.

- The choice of λ_3 , motivated by boundedness from below conditions, while not affecting the mono-Higgs sensitivity if $\lambda_3 = \lambda_{P1} = \lambda_{P2}$, has an impact on the mono- Z sensitivity since the coupling

$$g_{Haa} = \frac{1}{m_H v} [2 t_{2\beta}^{-1} s_\theta^2 (m_h^2 - \lambda_3 v^2) + s_{2\beta} c_\theta^2 v^2 (\lambda_{P1} - \lambda_{P2})]$$

²We remark here that implications from all indirect constraints - be it flavour, electroweak precision constraints or stability requirements - should be treated as preferred parameter space in a simplified model framework. It would contradict the idea of simplified models were these constraints taken at face value.

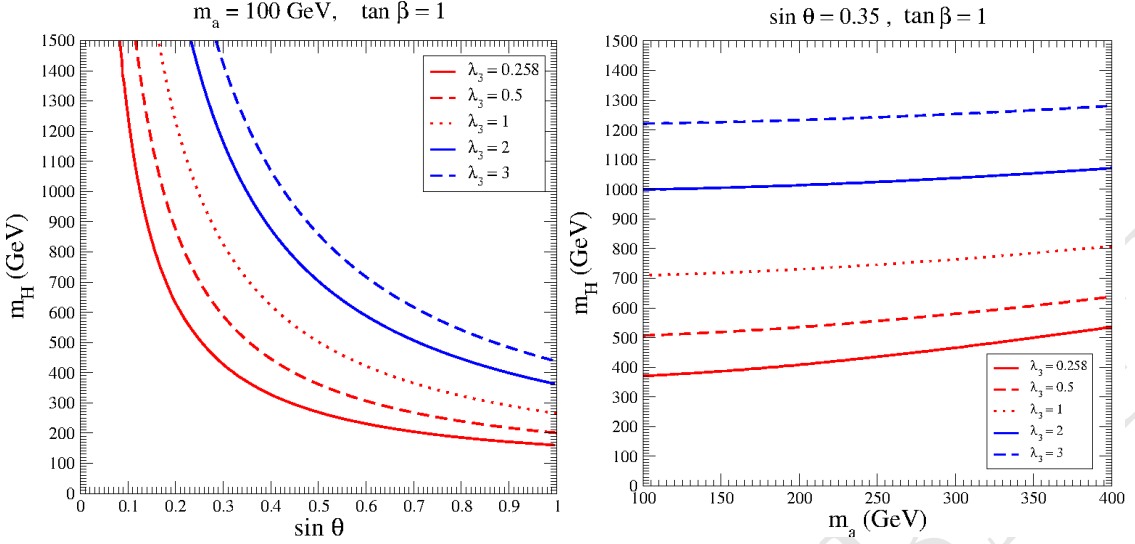


Figure 5: Regions of parameter space in the (m_a, m_{H_0}) (left) and $(\sin \theta, m_a)$ (right) planes for which the tree-level boundedness from below conditions 3.9 are satisfied, assuming $m_{H^\pm} = m_{H_0} = m_{A_0}$.

$$= \frac{1}{m_H v} \left[2 t_{2\beta}^{-1} s_\theta^2 (m_h^2 - \lambda_3 v^2) \right] \quad (3.12)$$

does depend on λ_3 and influences the balance between $\Gamma(H_0 \rightarrow aa)$ and $\Gamma(H_0 \rightarrow Za)$ which ultimately determines the $H_0 \rightarrow Za$ branching fraction. In short, the choice of $\lambda_3, \lambda_{P1}, \lambda_{P2}$ affects either mono-Higgs or mono- Z sensitivities (or both).

- Together with boundedness from below, other potential constraints are usually considered in the context of the 2HDM and apply in general, among them unitarity (see e.g. [18, 19]) and absolute stability of the electroweak vacuum (see e.g. [17]). In the present context we find these constraints are generically weaker than the boundedness from below condition and therefore disregard them in the following.
- The boundedness from below conditions are here evaluated at tree-level, but in a fully consistent treatment they should be evaluated including the effect of radiative corrections. This is however a much more involved process than what has been discussed above for the tree-level case (see e.g. [20]). In addition, the boundedness from below constraints discussed here are potentially sensitive to the existence of UV physics which our 2HDM+S simplified does not capture, and which could modify the above picture through the presence of higher-dimensional operators. Still, it is worth pointing out that for the 2HDM+S simplified model to be a good description of LHC phenomenology we require the new physics scale suppressing these effective operators to be above the TeV scale (since in our scans we are considering scalar masses up to ~ 1 TeV), and thus the presence of these high-energy operators is not expected to be of much help in case a runaway field direction exist at tree level in the 2HDM scalar potential.

4 Model kinematics and mapping to existing models

The signature and kinematic distributions of the 2HDM+a model at colliders are determined by the values assigned to the parameters described in the previous chapter. The model parameters can affect the total signal cross-section, the kinematic distributions, or both. In order to obtain a representative grid of benchmark points for collider searches and reduce this multi-dimensional parameter space, we scan ranges of the possible values of these parameters and observe the impact on the kinematic distributions for representative collider searches.

In this chapter, we will outline the existing experimental searches that can be used to search for this model, and present the distributions of the kinematic variables for each of the searches as a function of the free parameters of the model. We note that in the following we have chosen to fix the DM coupling y_χ to unity, and $\lambda_{P1} = \lambda_{P2} = \lambda_P = 3$ as explained in subsection 3.1.

4.1 Description of experimental searches

4.1.1 Signatures including a Higgs boson

Events with a 125 GeV Higgs boson, recently discovered with ATLAS and CMS [21, 22], and E_T^{miss} can indicate the production of Dark Matter candidates that recoil against the Higgs boson [23, 24]. The initial-state radiation (ISR) production of a Higgs boson is suppressed by the small Yukawa couplings of the Higgs boson to light quarks. Thus $h + E_T^{\text{miss}}$ searches such as [25, 26] directly probe potential new interactions of the Higgs and Dark Matter, as predicted by the 2HDM+a model [2, 5] due to the $a - A - h$ vertex.

$h(bb) + E_T^{\text{miss}}$ signature For the case where the Higgs boson decays into two b -quarks, such as studied in [25], the signal kinematics are studied at parton level. This allows a straightforward comparison to the model-independent results in [25], as described in subsection 6.1, and fast iteration over different model scenarios.

4.1.2 Signatures including a Z boson

Events with a Z boson and E_T^{miss} may signal the presence of invisible particles recoiling against the Z boson [27, 28]. LHC searches (e.g. [29, 30] for the most recent ones) have focused on invisible decays of the SM-like Higgs bosons or on topologies where the Z boson is produced as ISR from a quark. The ISR-based topologies generically favor radiation of a gluon or photon rather than a massive gauge boson, thus limiting the discovery sensitivity of a Z-based approach compared to monojet and mono-photon searches. In contrast, the model studied in this document generates the mono-Z signature dominantly via the all-bosonic H-a-Z vertex, which can lead to enhancements in the mono-Z sensitivity compared to jet and photon signatures.

Mono-Z (leptonic) signature Three consecutive stages of event selection are considered in the case the Z decays leptonically:

- Inclusive: Lepton p_T and η requirements corresponding to the typical experimental trigger acceptance are applied.

- Preselection: A dilepton candidate with an invariant mass in a window around the Z mass is required, and a minimum transverse momentum of the $\chi\bar{\chi}$ system is required.
- Final selection: Requirements on the main discriminating variables used in the relevant analyses are added: The angular separation in the transverse plane between the $\chi\bar{\chi}$ and $l^+ l^-$ systems $\Delta\Phi(l l, E_T^{\text{miss}})$, the relative transverse momentum difference between them $|p_{T,l} - E_T^{\text{miss}}|/p_{T,l}$ and the angular separation between the leptons $\Delta R(l l)$. Additionally, the E_T^{miss} requirement is tightened.

The exact event selection criteria are listed in the appendix, in [Table 2](#). The results in this and in the following section are at particle level.

Mono-Z (hadronic) signature The hadronic signature in $Z + E_T^{\text{miss}}$ events ($Z \rightarrow q\bar{q}$ decays in association with large missing transverse momentum) is complementary to the leptonic signature. Hadronic decays are more frequent than leptonic decays, but suffer from larger backgrounds. For these reasons, the Z (hadronic) + E_T^{miss} search is favored if the model include higher mass scalar and pseudoscalar bosons.

The event selection in this case changes depending on the production transverse momentum of the Z -boson, as in the case of the exchange of a high-mass CP-even H boson. If the Z -boson is boosted, then its hadronic decay products could be merged into a single jet, and the Z to QCD background discrimination can be improved by exploiting the presence of substructure within a single, large-radius jet (denoted by J). The *boosted* search is performed in addition to the *resolved* search, where the Z decay products are reconstructed as two separate small-radius jets (denoted by j).

For mono- $Z(\rightarrow q\bar{q})$ events intermediated by the exchange of a high-mass CP-even H boson, the Z -boson will be produced with a large transverse momentum and the hadronic decay products of such Z -boson could be merged into a single jet. Such “boosted” event topology is investigated by exploiting the reconstruction technique with a large-radius jet (denoted by J), in addition to more conventional “resolved” event topology where the Z decay products are reconstructed as two separate small-radius jets (denoted by j). The jet reconstruction and the following analysis are all performed at particle level after showering and hadronization implemented in Pythia 8.212 described above.

Two consecutive stages of event selection are considered for the boosted and resolved event topologies:

- Inclusive: minimal kinematic requirements are applied to a pair of small-radius jets (a single large-radius jet) for the resolved (boosted) event topology. These selection criteria are applied separately, i.e, not sequentially.
- Final selection: selection criteria are applied to the a number of variables. The invariant mass of the pair of small-radius jets or the single large-radius jet is required to be within a window around the Z mass. In addition, selection is applied to the azimuthal angular difference between the $\chi\bar{\chi}$ and the hadronic Z -boson system, $\Delta\Phi(jj \text{ or } J, E_T^{\text{miss}})$, and the magnitude of E_T^{miss} . These final selection cuts are applied sequentially to mimic a realistic analysis; in this study the boosted selection cuts are

applied first and then the resolved selection cuts are applied to those events that fail the boosted ones.

The exact event selection criteria are listed in the appendix, in [Table 3](#). The results in this and in the following section are at particle level.

4.1.3 Signatures including heavy flavor quarks

Heavy flavor final state can have sizable contributions to the production of the CP-even and CP-odd scalar mass eigenstates, due to the Yukawa structure of the couplings in the SM sector.

4.2 Kinematic distributions justifying the choice of parameter scan

4.2.1 Masses of the A , H , and a bosons (M_A , M_H , and M_a)

The **masses of the mediators M_A , M_H , and M_a of the pseudoscalars A and a and the scalar H** , which are the mediators of the resonant mono- h and mono- Z processes, affect the shape of the E_T^{miss} distribution of these processes. In the mono- Z and mono- H channels, the resonant production occurs through the $2 \rightarrow 1 \rightarrow 2$ processes $gg \rightarrow A \rightarrow ah$ and $gg \rightarrow H \rightarrow aZ$, respectively, with the light pseudoscalar decaying invisibly as $a \rightarrow \chi\chi$. In this case, the $A/H \rightarrow ah$ process produces a resonance in the invariant mass distribution of the final state system with a width determined by the widths of a , A/H , and of the SM bosons. This results in a peak in the transverse momentum distribution of the DM system, reconstructed as E_T^{miss} in the detector.

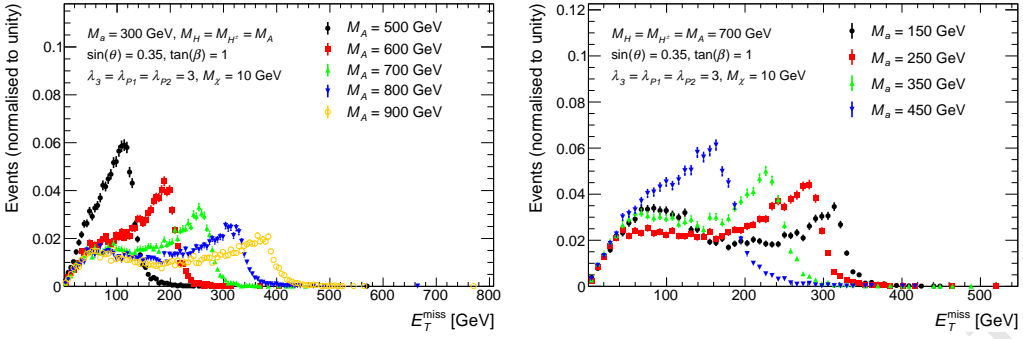
The location of this Jacobian peak can be calculated analytically starting from the masses of the particles involved in the decay [2]:

$$E_T^{\text{miss},\text{max}} \approx \frac{\sqrt{\left(M_{A/H}^2 - M_a^2 - M_{h/Z}^2\right)^2 - 4M_a^2M_{h/Z}^2}}{2M_{A/H}}. \quad (4.1)$$

Thus, increasing M_A results in a Jacobian peak at higher E_T^{miss} , as shown in [Figure 6a](#), [Figure 7](#) and [Figure 53](#). Conversely, models with higher M_a have a Jacobian peak at lower E_T^{miss} , as indicated in [Figure 6b](#) and [Figure 54](#). For $M_{A/H} \approx M_a + m_{Z/h}$, both the a and Z/h bosons are produced approximately at rest, leading to an event population with overall low boost. These qualitative trends are consistent with the distributions of the other main selection variables as shown in the appendix ([Appendix B](#)).

A potentially large fraction of the mono- h signal events is also produced in non-resonant $2 \rightarrow 3$ processes $gg \rightarrow h\chi\chi$, as in ??, leading to a broader distribution of the invariant mass of the decay products. Consequently, this results in a broader and softer E_T^{miss} distribution that is distinct from the Jacobian peak discussed above, and contributes to the off-peak features of [Figure 6b](#) and [Figure 6a](#).

The masses M_a and M_A influence the kinematics in the $t\bar{t} + E_T^{\text{miss}}$ signature as well. As shown in [Figure 10](#), the E_T^{miss} , and leading and trailing top quark p_T distributions



(a) E_T^{miss} distribution for points with different M_A and fixed $M_a = 300$ GeV. (b) E_T^{miss} distribution for points with different M_a and fixed $M_A = 700$ GeV.

Figure 6: Parton-level E_T^{miss} distribution of mono-Higgs events for different M_a and M_A , with $M_H = M_{H^\pm} = M_A$, $\sin \theta = 0.35$, $\tan \beta = 1$, $M_\chi = 10$ GeV and $\lambda_{P1} = \lambda_{P2} = \lambda_3 = 3$

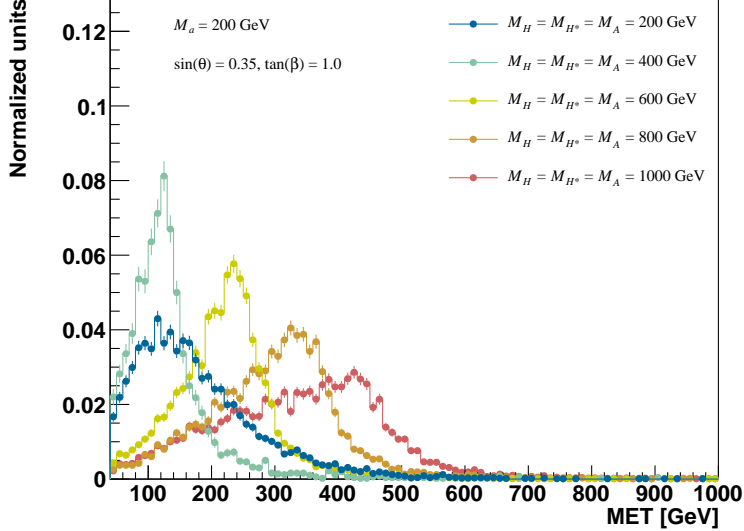


Figure 7: The E_T^{miss} distribution in signatures including a Z boson after preselection in the leptonic channel, with varying M_H values for fixed $M_a = 200$ GeV and $M_A = M_{H^\pm} = M_H$.

broaden with increasing M_a . Similarly, for values of $M_A < M_a$, as M_A increases, the kinematic distributions mentioned above also broaden, as shown in Figure 11.

Since the shape of the E_T^{miss} distribution affects the design of experimental searches, and to a large extent their sensitivity, *it is desirable to scan the M_A and M_a parameter space.*

In designing a search for evidence of this particular model, it may be useful to consider not only the E_T^{miss} , but also the transverse mass M_T ³ variable. The distributions of both

³The massless definition is used here: $M_T = \sqrt{2E_T^{\text{miss}} p_{T,Z} (1 - \cos(\Delta\phi))}$

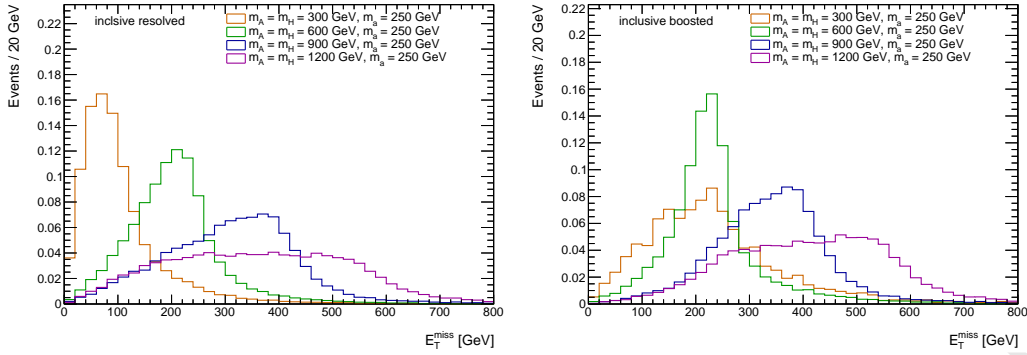


Figure 8: E_T^{miss} distributions in the resolved (left) and boosted (right) hadronic Z search, after applying the inclusive selection. The signal masses are chosen to be $M_H = 300, 600, 900$ and 1200 GeV with the fixed $M_a = 250$ GeV and $M_A = M_{H^\pm} = M_H$.

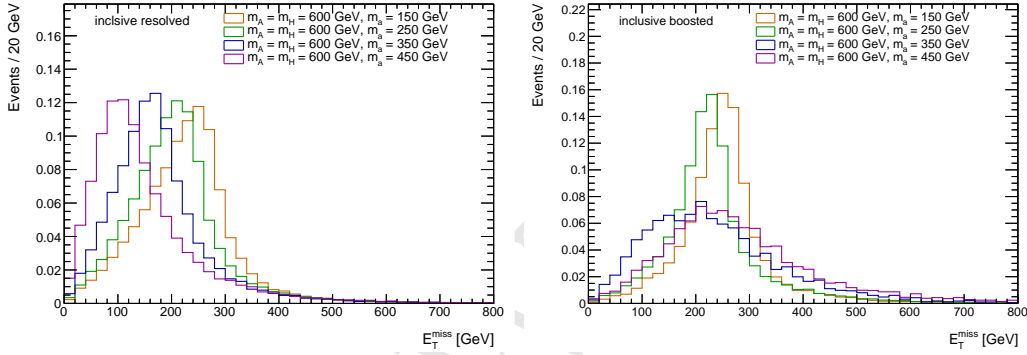


Figure 9: E_T^{miss} distributions in the resolved (left) and boosted (right) hadronic Z search, after applying the inclusive selection. The signal masses are chosen to be $M_a = 150, 250, 350$ and 450 GeV with the fixed $M_H = 600$ GeV ($= M_A = M_{H^\pm}$).

variables after final selection are shown in Figure 12 for the $Z+E_T^{\text{miss}}$ searches. Both distributions show Jacobian peak structures due to dominant effect of the diagram with resonant H exchange. In the case of $M_a < M_H$, the peak structure is more defined in the M_T distribution than in the E_T^{miss} , thus helping to distinguish a possible signal from background. Where the resonant diagram does not contribute, i.e. for $M_a \approx M_H$ or $M_a > M_H$, the M_T distribution does not show a significantly different structure from the E_T^{miss} distribution and will not provide an improved sensitivity.

For mono- h , the **mass of the heavy neutral scalar Higgs boson H** has an indirect effect on the rate and kinematics of the signal. This is caused by the dependence of the coupling strength of the $a - A - h$ vertex, and thus decay width of the pseudoscalar A , on M_H [2]. Therefore, a change of M_H can strongly affect the relative contribution of resonant versus non-resonant signal processes, as illustrated in Figure 13. For mono-Z, there is no corresponding effect of M_A on the resonant and non-resonant signal yields, since the $a - H - h$ vertex has a simpler structure with no M_A dependence.

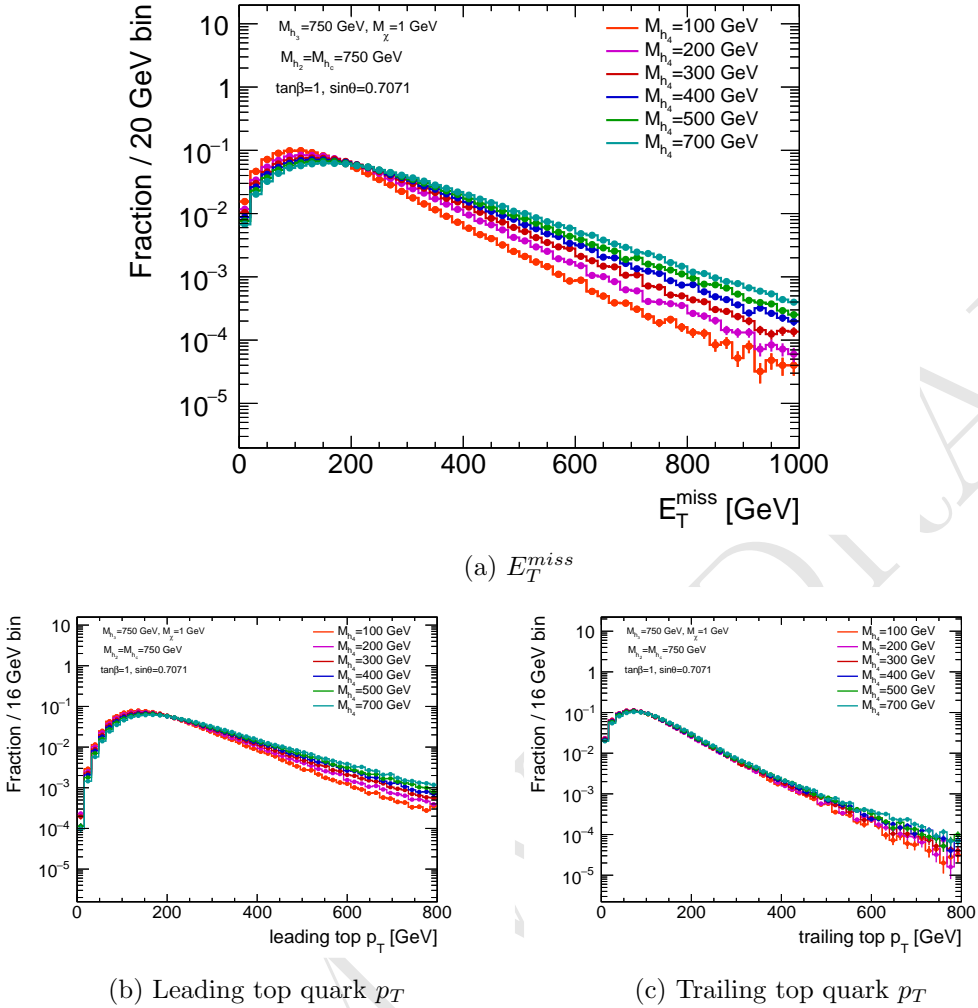


Figure 10: The E_T^{miss} , leading and trailing top p_T distributions for inclusive $t\bar{t} + \chi\bar{\chi}$ production for various values of M_a , with $M_A = 750$ GeV, $M_H = M_{H^\pm} = 750$ GeV, $\tan\beta = 1$, and $\sin\theta = 0.7071$.

The choice $M_H = M_A$ results in a detectable total cross section and a dominant contribution of the resonant mono- h signal process for many signal points. This choice allows us to test diverse E_T^{miss} distributions and results in about equal contributions to the sensitivity through the $Z + E_T^{miss}$ and $h + E_T^{miss}$ signatures, highlighting their complementarity. For this reason *the choice $M_H = M_A$ is adopted* for all scans.

The mass of the neutral scalar H^\pm does not affect the model kinematics, as shown in Appendix ???. Models with $M_{H^\pm} \neq M_H$ are moreover strongly constrained by electroweak precision measurements of the ρ parameter [2]. Therefore, for simplicity, the *neutral scalar H^\pm is assumed to be mass-degenerate to H* .

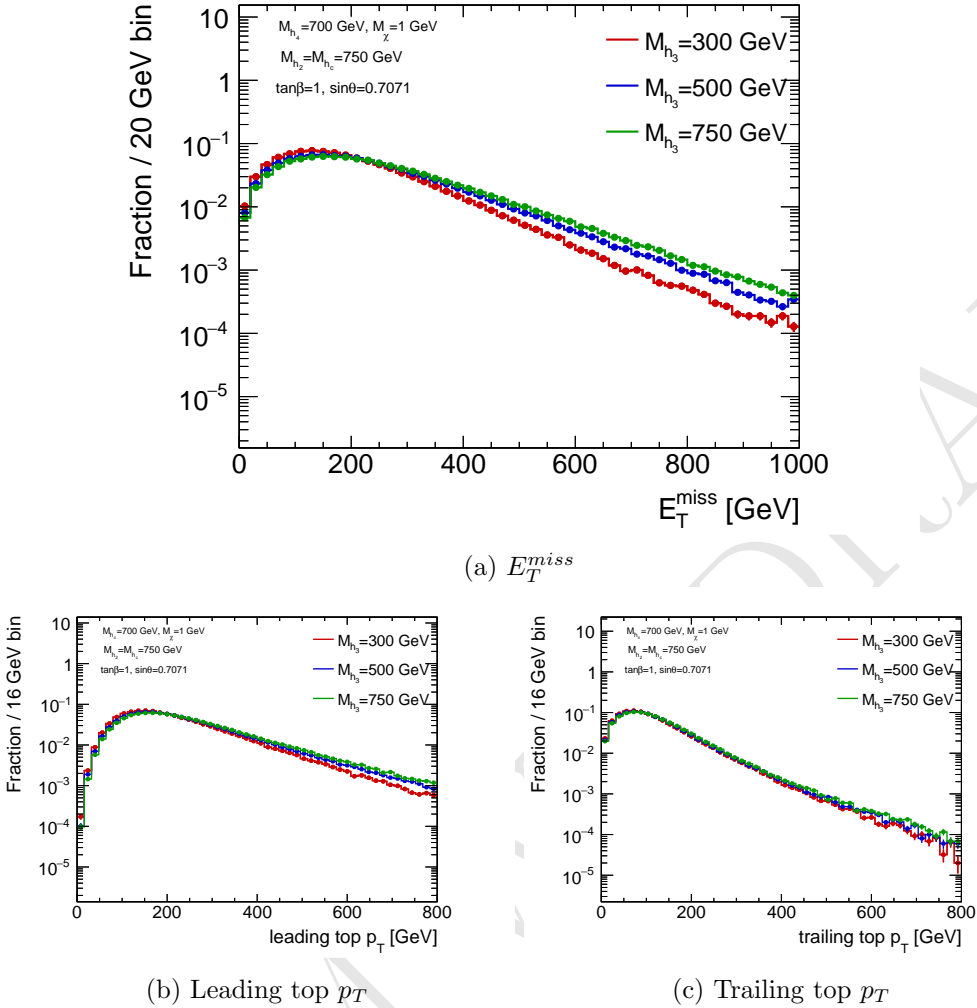


Figure 11: The E_T^{miss} , leading and trailing top p_T distributions for inclusive $t\bar{t} + \chi\bar{\chi}$ production for various values of M_A , with $M_A = 700$ GeV, $M_H = M_{H^\pm} = 750$ GeV, $\tan\beta = 1$, and $\sin\theta = 0.7071$, before any analysis selection.

4.2.2 Mixing angle between the two pseudoscalars A and a ($\sin\theta$)

The sine of the mixing angle between the two pseudoscalars A and a , $\sin\theta$, affects not only the cross section, but also the shape of the E_T^{miss} distribution in searches including a Higgs boson, as shown in Figure 17a. For the resonant diagram $gg \rightarrow A \rightarrow ah \rightarrow \chi\bar{\chi}h$, the product of cross section times branching ratios $\mathcal{B}(A \rightarrow ah)\mathcal{B}(a \rightarrow \chi\bar{\chi})$ scales with $\sin^2\theta \cos^6\theta$, while for the diagram $gg \rightarrow a \rightarrow A^*h \rightarrow \chi\bar{\chi}h$, the product of cross section times branching ratios $\mathcal{B}(a \rightarrow Ah)\mathcal{B}(A \rightarrow \chi\bar{\chi})$ scales with $\sin^6\theta \cos^2\theta$. This is shown in Appendix ???. Therefore, at small $\sin\theta$, the resonant diagram $A \rightarrow ah$ is the dominant production mode and the E_T^{miss} distribution has a Jacobian peak following Equation 4.1; while at large $\sin\theta$, the $a \rightarrow A^*h$ diagram starts to dominate and produces a second peak at a lower E_T^{miss} value.

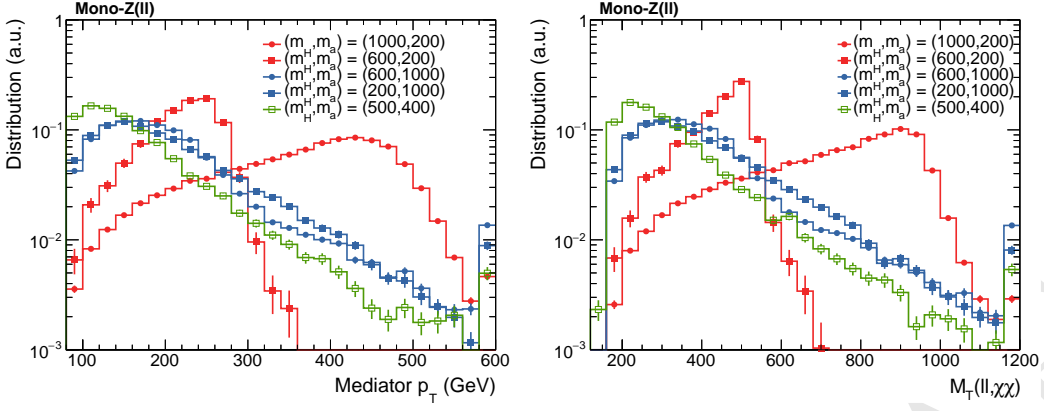


Figure 12: E_T^{miss} and M_T distributions after the full selection of $Z(\text{lep})+E_T^{\text{miss}}$ search. Both distributions show a peaked structure around M_H in the $M_H > M_a$ regime, reflecting the resonant production of H with a subsequent decay $H \rightarrow aZ$.

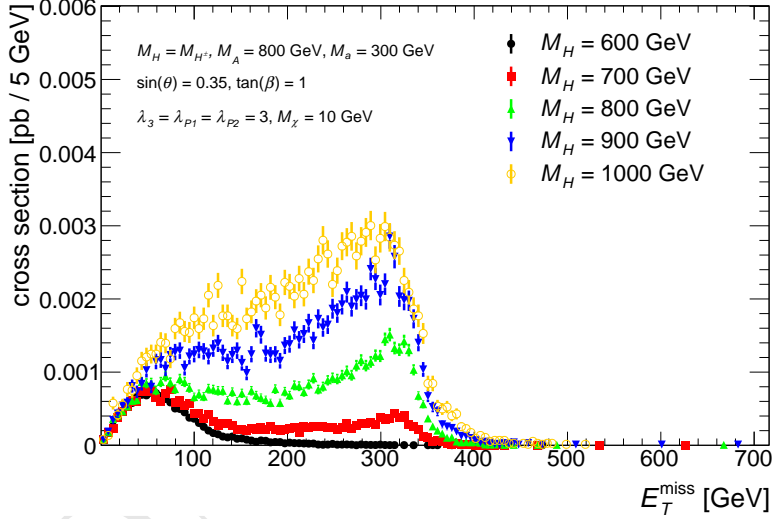


Figure 13: The E_T^{miss} distribution, accounting for the production cross section, of $h(bb)+E_T^{\text{miss}}$ signal events for five representative choices of $M_H = M_{H^\pm}$.

Figure 14: E_T^{miss} distribution in $h(bb)+E_T^{\text{miss}}$ and $Z+E_T^{\text{miss}}$ events for different M_H

Scans of the $\sin \theta$ parameter show they have minimal effect on the kinematic distributions for searches with a Z boson (Figure 17b).

In the $t\bar{t} + E_T^{\text{miss}}$ signature, the A (h_3 in the figure) and a (h_4 in the figure) mass peaks are quite narrow for values where $\sin \theta$ approaches 1, and $a \rightarrow \chi\bar{\chi}$ is the dominant $\chi\bar{\chi}$ production mode, as shown in Figure 15. However, no significant kinematic dependence on $\sin \theta$ is observed in the E_T^{miss} and top quark p_T as shown in Figure 16 before any analysis cuts are applied.

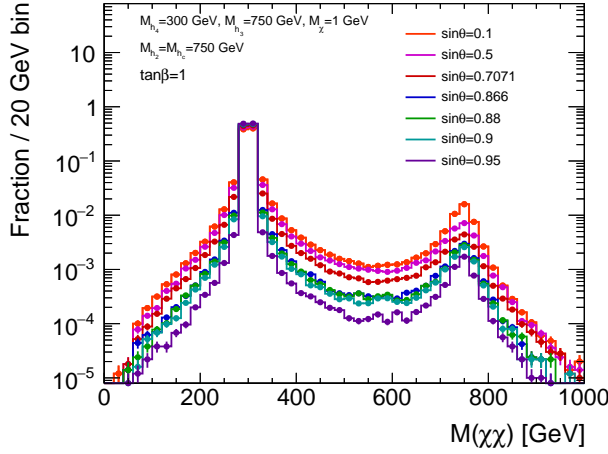


Figure 15: The mass distribution of the $\chi\bar{\chi}$ system for various values of $\sin \theta$, with $M_a = 300$ GeV, $M_A = 750$ GeV, $M_H = M_{H^\pm} = 750$ GeV, and $\tan \beta = 1$.

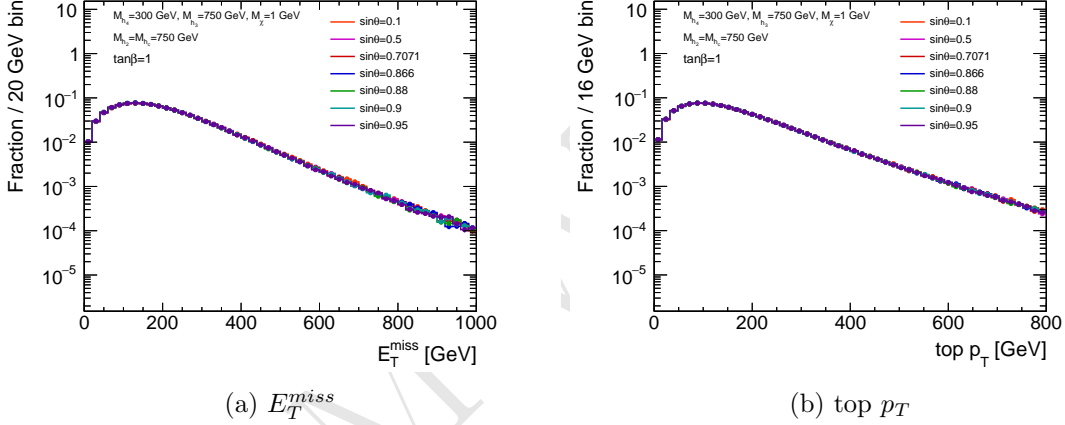
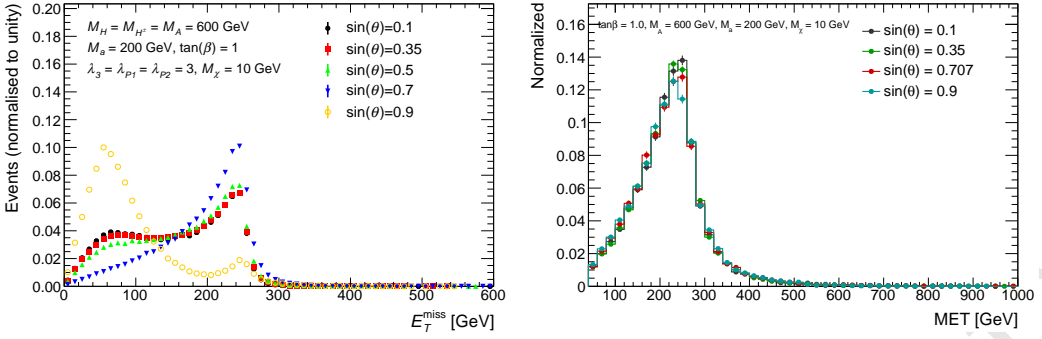


Figure 16: The E_T^{miss} and top p_T distribution for inclusive $t\bar{t} + \chi\bar{\chi}$ production for various values of $\sin \theta$, with $M_a = 300$ GeV, $M_A = 750$ GeV, $M_H = M_{H^\pm} = 750$ GeV, and $\tan \beta = 1$.

4.2.3 Ratio of the doublet vacuum expectation values ($\tan \beta$)

For mono- h signals, the shape of the E_T^{miss} distribution also has a non-trivial dependence on $\tan \beta$, as can be seen in Figure 18. As discussed in the sensitivity study later, at small $\tan \beta$, the Yukawa coupling to top quark is large and the signal production mode is dominated by the non-resonant 3-body process $gg \rightarrow h\chi\bar{\chi}$, which gives a broad and soft E_T^{miss} spectrum. As $\tan \beta$ increases, Γ_A decreases. With a more narrow A , the relative contribution of resonant A decays increases, and the Jacobian peak grows more pronounced, eventually dominating the E_T^{miss} spectrum. When the on-shell $A \rightarrow ah$ decay is kinematically forbidden, i.e. when $M_A < M_a + M_h$, the shapes of E_T^{miss} distributions become similar and the dependence on $\tan \beta$ almost disappears. For small values of $\tan \beta$ there is a slight softening and broadening of the E_T^{miss} distribution caused by the increased contribution



(a) E_T^{miss} distribution for five representative models with different $\sin \theta$ and fixed scans of $\sin \theta$ for fixed $M_A = M_H = M_{H^\pm} = M_A = M_H = M_{H^\pm} = 600$ GeV, $M_a = 600$ GeV and $M_a = 200$ GeV. 200 GeV.

(b) E_T^{miss} distribution after preselection for $\tan \beta = 1$, $M_A = 600$ GeV, $M_a = 200$ GeV, $M_\chi = 10$ GeV.

Figure 17: E_T^{miss} distributions in $h(bb) + E_T^{\text{miss}}$ and $Z(\text{lep}) + E_T^{\text{miss}}$ events for different $\sin \theta$. In both cases, $\tan \beta = 1$ and $M_\chi = 10$ GeV.

from non-resonant $Z + a$ production in $Z + E_T^{\text{miss}}$ searches.

In the $t\bar{t} + E_T^{\text{miss}}$ signature, and in the limit of small $\tan \beta$ values, the couplings of A (h_3 in the figure) and a (h_4 in the figure) to down-type quarks are heavily suppressed regardless of the Yukawa assignment. At LO, $t\bar{t} + \chi\bar{\chi}$ associated production is mediated through either CP-odd weak eigenstate, A or a , though it is shown in Figure 20 that $a \rightarrow \chi\bar{\chi}$ is the dominant production mode. Although the relative mediator contribution is dependent on $\tan \beta$, observables such as E_T^{miss} and top quark p_T only have a moderate kinematic dependence on $\tan \beta$ as demonstrated in Figure 21 before any analysis cuts. Other variables, such as the transverse mass M_T , are more affected by the contribution of the high mass mediator, as shown in Figure 21 after kinematic cuts.

The production cross-section for a, h, H and A are driven by top-quark loops in the gluon-fusion channel [31], as shown e.g. [as shown in the Feynman diagram], and enhanced for small values of $\tan \beta$. For this reason, and to highlight the complementarity of the $H + E_T^{\text{miss}}$ and $Z + E_T^{\text{miss}}$ signatures, the main focus of the parameter scans should be on the small $\tan \beta$ region. Setting $\tan \beta$ to unity leads to a sufficiently large on-shell contribution even at low masses. This in turn increases the number of events at higher E_T^{miss} , so that the $H + E_T^{\text{miss}}$ search can have a comparable sensitivity to the $Z + E_T^{\text{miss}}$ search even though it requires higher E_T^{miss} . Moreover, since the cross-section times branching ratio for the $b\bar{b} + E_T^{\text{miss}}$ signature is enhanced at high values of $\tan \beta$ (see Eq. 3.2 and 3.3 in Ref. [2]) it is desirable to perform a coarse scan in $\tan \beta$ as well.

It is interesting to note however that the relative total width for the heavy scalar H becomes unphysically large at high $\tan \beta$ when all scalars have the same mass, due to the very large $H \rightarrow aa$ rate. This can be cured by tuning the mass of the heavy scalar so that the coupling between the heavy scalar and the light pseudoscalar g_{Haa} becomes small for this scan only, therefore suppressing the $H \rightarrow aa$ rate that drives the width. An example of the heavy scalar width as a function of $\tan \beta$, with $M_H = M_A = 600$ GeV, $M_{H^\pm} = 664$

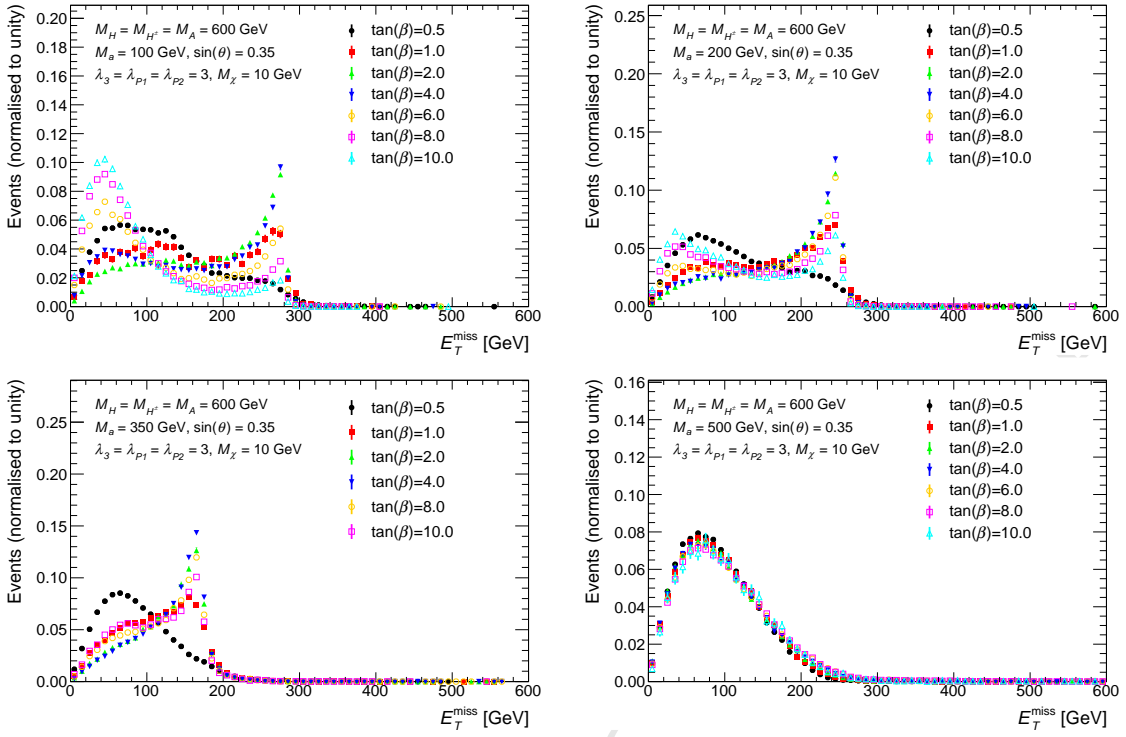


Figure 18: Missing transverse momentum distribution of $h \rightarrow bb + E_T^{\text{miss}}$ signal events at parton level with different $\tan\beta$ and fixed $M_A = M_H = M_{H^\pm} = 600 \text{ GeV}$, $M_\chi = 10 \text{ GeV}$, $\sin\theta = 0.35$, and $\lambda_{P1} = \lambda_{P2} = \lambda_3 = 3$. The values of M_a are set to 100, 200, 350, and 500 GeV, respectively. The shapes of the E_T^{miss} distributions for different $\tan\beta$ are similar when $M_A < M_h + M_a$. Note, in these figures, both the contributions of gg and $b\bar{b}$ initiated processes are included and a combined histogram is produced according to their corresponding cross sections.

GeV, $\sin\theta = 0.35$, $M_\chi = 10 \text{ GeV}$ and $g_{\text{DM}} = 1$ is shown in Fig. 22.

Even though this choice of parameters for this scan introduces a specific tuning and therefore model-dependence, it can be justified by noting that the trilinear scalar couplings are very sensitive to changes in the model’s masses and couplings, and this in turn changes the decay partner of the heavy scalar and of the Higgs partners. Furthermore, the Higgs width does not influence the $b\bar{b} + E_T^{\text{miss}}$ signal directly. Nevertheless, if this is tuning is not performed, particular care has to be taken at high $\tan\beta$ values to obtain reasonable results outside the narrow-width approximation, both for the generation of the signal and for the interpretation of the results.

4.3 Comparison with existing pseudoscalar models and recasting of HF+ E_T^{miss} search results

To date, simplified models of DM [1, 32] that add a single scalar or pseudoscalar mediator and the DM particle to the SM are used as benchmarks for the Run II CMS and ATLAS HF+ E_T^{miss} searches. These are called **DMsimp** models in the following. The kine-

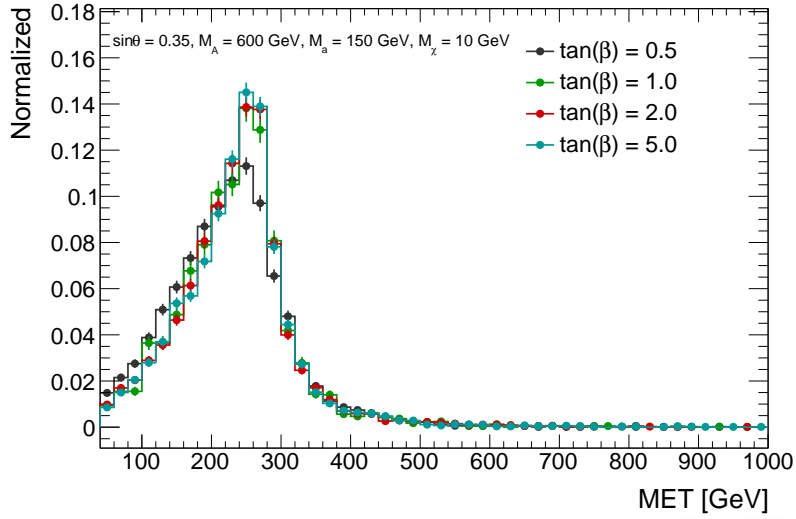


Figure 19: E_T^{miss} distribution after preselection for scans of $\tan \beta$ for fixed $M_A = 600$ GeV and $M_a = 150$ GeV. This parameter has little impact on the kinematic distributions, except for small values of $\tan \beta$ where there is a slight softening and broadening of the E_T^{miss} distribution caused by the increased contribution from the top box Feynman diagram.

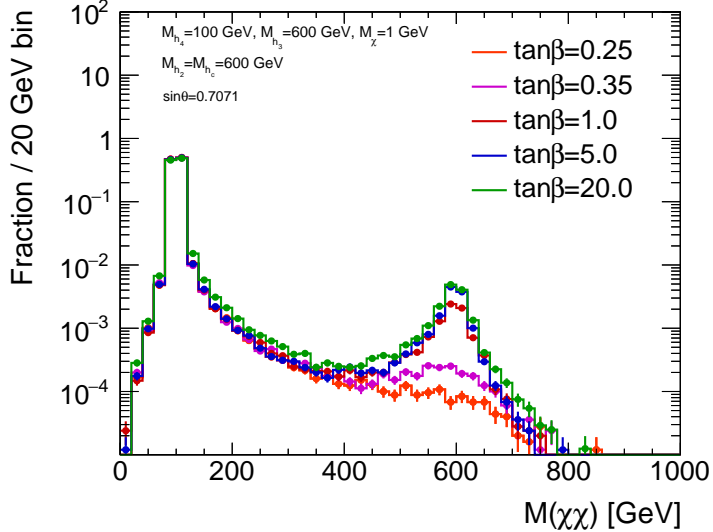


Figure 20: The mass distribution of the $\chi\bar{\chi}$ system for various values of $\tan \beta$, with $M_a = 100$ GeV, $M_A = 600$ GeV, $M_H = M_{H^\pm} = 600$ GeV, and $\sin \theta = 0.7071$.

matics and cross-section of the pseudoscalar DMsimp models can map directly onto those of the 2HDM+a model, when accounting for the contributions from the light and heavy pseudoscalar mediators.

The comparison of some of the relevant kinematic distributions between the pseudoscalar simplified model and the 2HDM+a model using two different values of M_a , is shown

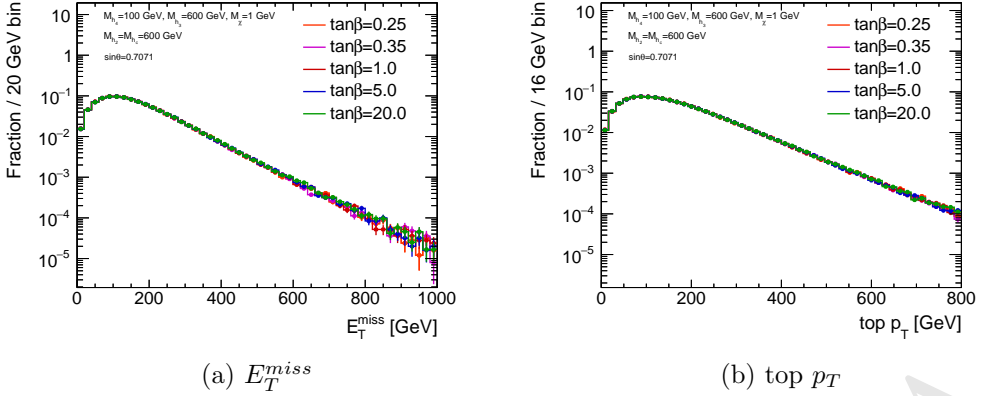


Figure 21: The E_T^{miss} and top p_T distribution for inclusive $t\bar{t} + \chi\bar{\chi}$ production for various values of $\tan\beta$, with $M_a = 100 \text{ GeV}$, $M_A = 600 \text{ GeV}$, $M_H = M_{H^\pm} = 600 \text{ GeV}$, and $\sin\theta = 0.7071$.

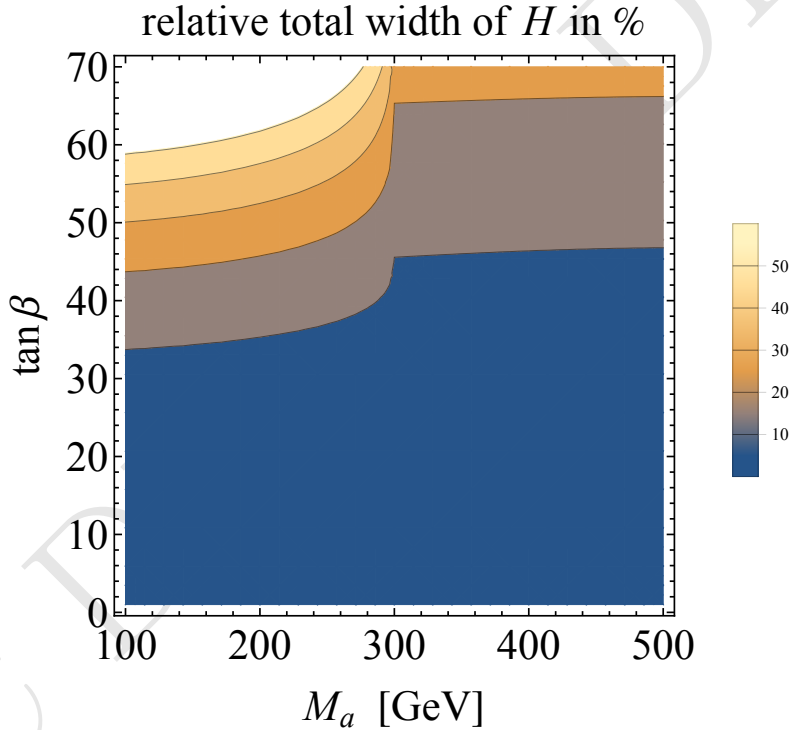


Figure 22: The width of the heavy scalar as a function of $\tan\beta$, with $M_H = M_A = 600 \text{ GeV}$, $M_{H^\pm} = 664 \text{ GeV}$, $\sin\theta = 0.35$, $M_\chi = 10 \text{ GeV}$ and $g_{\text{DM}} = 1$.

in Figure 24. In these figures, the parameters used are: $M_A = 600 \text{ GeV}$, $M_H = M_{H^\pm} = 600 \text{ GeV}$, $\sin\theta = 0.7071$, $\tan\beta = 1$, while M_a is either 100 or 600 GeV. The distributions for the two models agree when the mediator mass in the DMsimp model is set to M_a and the contribution from A decays is smaller since A is more massive than a .

The DMsimp model has only one mediator particle. Figure 25 shows that the 2HDM+a

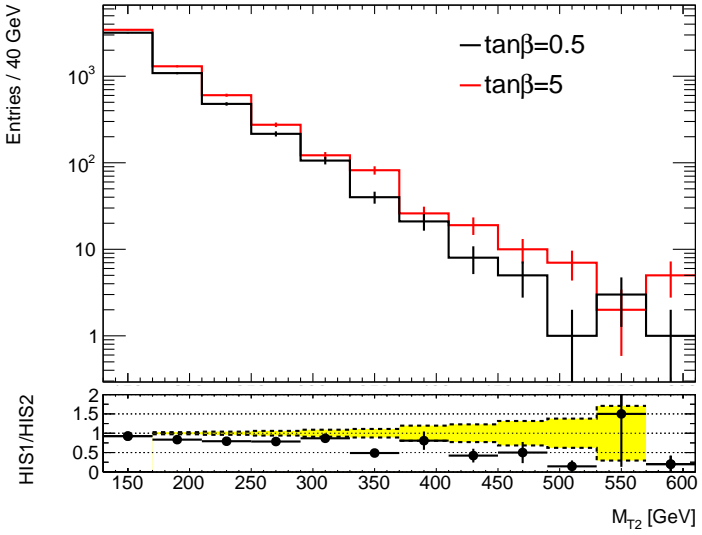


Figure 23: The M_T distribution in the $t\bar{t} + E_T^{\text{miss}}$ signature for different values of $\tan\beta$, after all selection cuts.

model can be represented as the sum of two contributions, one from the light pseudoscalar and the other one from the heavy pseudoscalar. This is because the HF+ E_T^{miss} signatures are dominantly produced in diagrams involving the invisible decays of the two CP-odd scalars. The 2HDM+a model is equivalent to the single pseudoscalar simplified model `DMsimp` when A is much heavier than a , and therefore the former does not contribute to the considered final state. However, when the two mediators are closer in mass, the $pp \rightarrow t\bar{t}A$ contribution becomes more relevant. This can be seen in Figure 26, where the two models are compared assuming $m(A) = 750$ GeV and two different values for $m(a)$. An excellent agreement is observed between `DMsimp` and 2HDM+a at parton-level variables sensitive to the helicity structure of the interaction between top and the mediator[33], if the invariant mass of the two DM particles in the 2HDM is smaller than 200(300) GeV for $m(a) = 150(300)$ GeV respectively. This gives confidence that, once the contribution from A production is identified and separated, it is possible to fully map the 2HDM+a kinematics to the existing `DMsimp` model.

The mapping that can be used to reinterpret existing searches that use the `DMsimp` model is achieved by taking, for each set of the parameters, the average of the selection acceptances for $m(A)$ and $M(A)$ obtained from the `DMsimp` model, weighted by the respective cross-section for A (σ_A) and a (σ_a) production:

$$Acc_{2HDM}(m(A), M(a)) = \frac{\sigma_a \times Acc_{DMsimp}(m(a)) + \sigma_A \times Acc_{DMsimp}(m(A))}{\sigma_a + \sigma_A} \quad (4.2)$$

The acceptance in this case is obtained as a parton-level implementation of the two-lepton analysis described in [arXiv:1710.11412]. The acceptance estimated in this way is shown as red triangles in Figure 27, and an excellent agreement can be seen with the

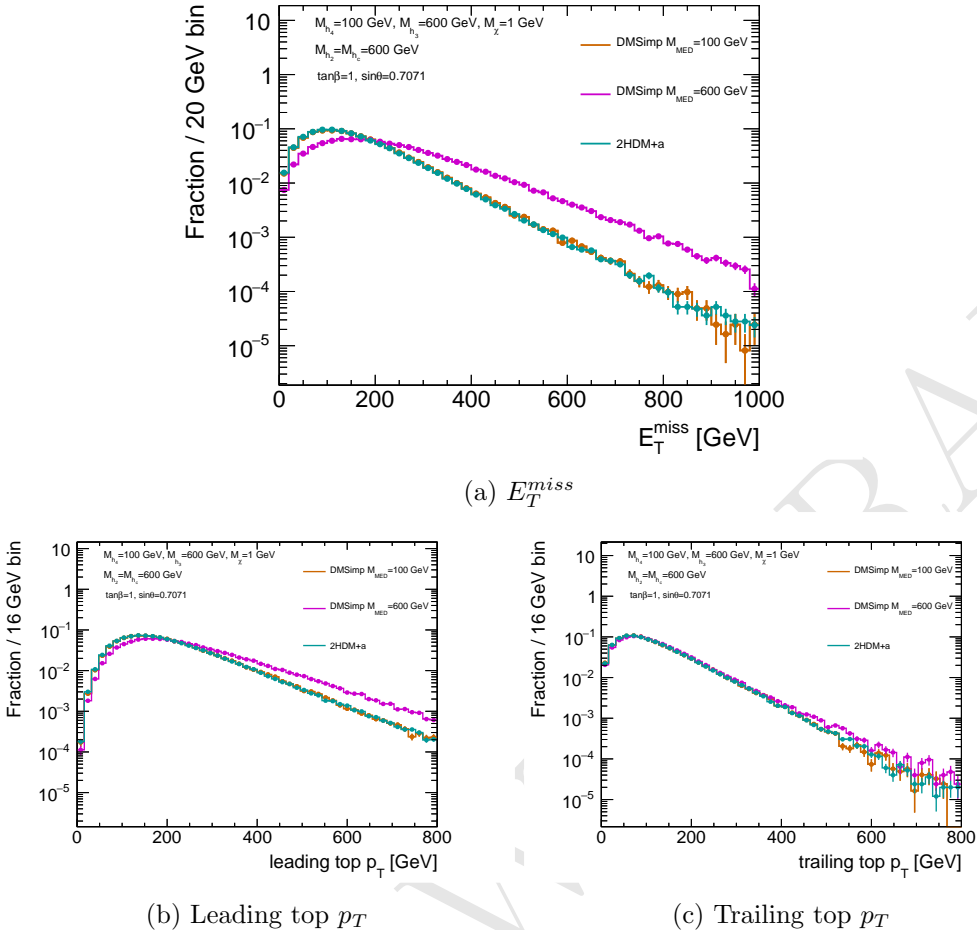


Figure 24: The E_T^{miss} , leading and trailing top p_T distributions for inclusive $t\bar{t} + \chi\bar{\chi}$ production for different values of M_a , with $M_A = M_H = M_{H^\pm} = 600$ GeV, $\tan \beta = 1$, $M_\chi = 1$ GeV and $\sin \theta = 0.7071$, compared to the DMsimp pseudoscalar model.

acceptances evaluated directly on the 2HDM samples. Further validation was performed also on the acceptances calculated as a function of $\sin\theta$ and $\tan\beta$. Finally, the formula was successfully tested also with $|M_A - M_a| \sim 50$ GeV, where interference between the production of the two bosons is possible.

5 Parameter grid

The studies in the previous section show that varying most of the model parameters lead to non-trivial modifications of the for the $H+E_T^{miss}$ and $Z+E_T^{miss}$ searches. We decide to investigate the model parameter space through two-dimensional and one-dimensional scans of five parameters: the light pseudoscalar mass (M_a), the heavy pseudoscalar mass (M_A) that we set equal to the mass of the heavy and charged Higgs bosons ($M_A = M_H = M_{H^\pm}$), the mixing angle $\sin \theta$, the ratio of VEVs of the Higgs doublets $\tan \beta$ and the dark matter particle mass M_χ . The benchmark model points that have been agreed within the DMWG

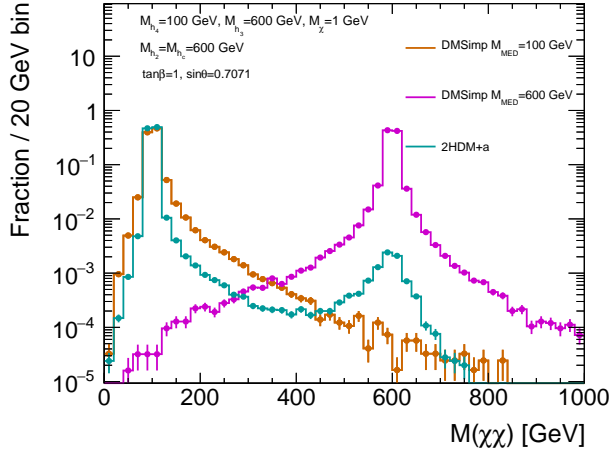


Figure 25: The mass distribution of the $\chi\bar{\chi}$ system for DMsimp pseudoscalar models with $M_a = 100$ GeV and $M_a = 600$ GeV, compared with 2HDM+a with $M_a = 100$ GeV, $M_A = 600$ GeV, $M_H = M_{H^\pm} = 600$ GeV, $\sin \theta = 0.7071$ and $\tan \beta = 1$. TODO: needs different markers.

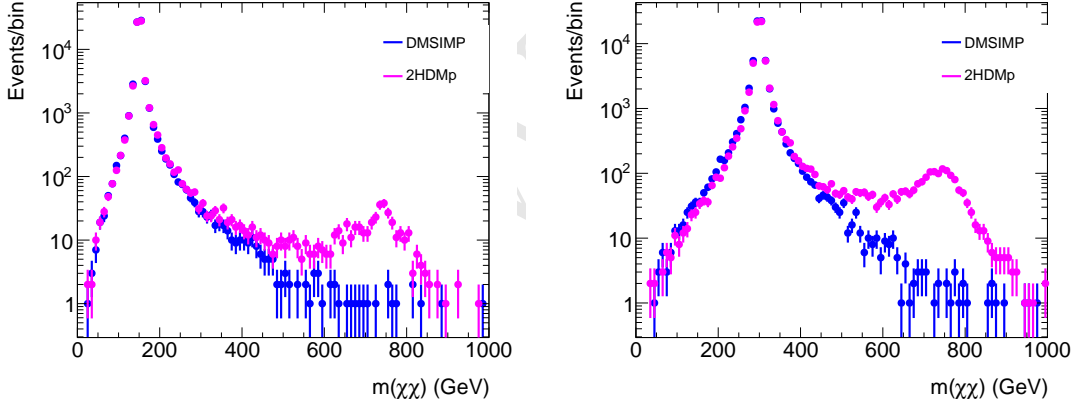


Figure 26: Comparison of $m(\chi\chi)$, the invariant mass of the two DM particles for the DMsimp (blue) and the 2HDMp model (magenta) with $m(A) = M_{med} = 750$ GeV. The plot on the left uses $M_a = 150$ GeV, while the plot on the right uses $M_a = 300$ GeV.

and are suggested here do not provide an exhaustive scan the entire parameter space of this model, but highlights many of the features that are unique of this model and showcases the complementarity of the various signatures.

Scan in the $M_a, M_A = M_H = M_{H^\pm}$ plane The main parameter grid proposed to investigate this model with LHC data spans combinations of the light pseudoscalar mass (M_a) and the heavy pseudoscalar mass (M_A) plane, fixing $M_A = M_H = M_{H^\pm}$. The mixing angle $\sin \theta$ is fixed to 0.35, to evade precision constraints. $\tan \beta$ is fixed to unity to obtain

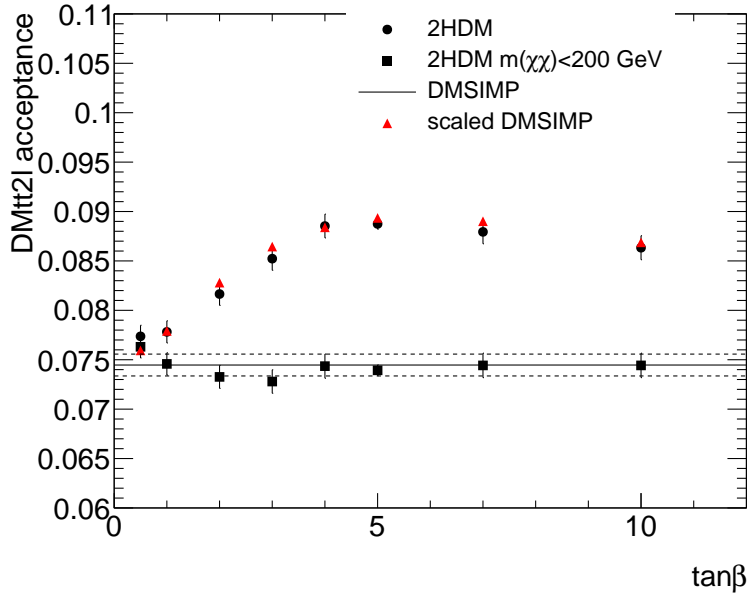


Figure 27: Acceptance of the two-lepton analysis as a function of $\tan\beta$ for the $2HDMp$ model (round markers), for the $2HDMp$ model considering only events with $m(\chi\chi) < 200$ GeV (square markers), and for the DMSIMP model (full line) for a mediator mass of 150 GeV. The two dashed lines indicate the statistical error of the DMSIMP. The value of $m(A)$ is fixed at 600 GeV, and $\sin\theta = 0.35$. The acceptance calculated from the DMSIMP acceptance rescaled following the prescription in Equation 4.2 (red triangles) is also shown.

a mixture of resonant and non-resonant processes for the $H+E_T^{\text{miss}}$ and $Z+E_T^{\text{miss}}$ searches. The DM particle mass is fixed to 10 GeV, to obtain cross-sections that are sufficiently large to be probed by Run-2 LHC searches. The spacing of the grid in M_a and M_A is left to the individual searches. The parameters $\sin\theta$, $\tan\beta$ and M_χ are scanned separately.

Scan in the M_a , $\tan\beta$ plane A two-dimensional scan in the M_a , $\tan\beta$ plane, fixing $M_A = M_H = M_{H^\pm} = 600$ GeV, is used to emphasize the complementarity of the $H+E_T^{\text{miss}}$ and $Z+E_T^{\text{miss}}$ searches with the heavy flavor + E_T^{miss} searches. The scan in M_a includes masses between 10 and 350 GeV, while the $\tan\beta$ scan includes $\tan\beta = 50, 45, 40, 35, 30, 25, 20, 15, 10, 5$, where the high- $\tan\beta$ points are of primary interest for the heavy flavor searches.

Scans in $\sin\theta$ Two one-dimensional scans in $\sin\theta$ are also suggested for further comparison of the $H/Z+E_T^{\text{miss}}$ and $b\bar{b}+E_T^{\text{miss}}$ analyses. In the first scan, resonant processes dominate with $M_A = M_H = M_{H^\pm} = 600$ GeV and $M_a = 200$ GeV, while in the second scan $M_A = M_H = M_{H^\pm} = 1000$ GeV and $M_a = 350$ GeV. For both scans, $\tan\beta$ and the DM mass are fixed to $\tan\beta=1$ and $M_\chi = 10$ GeV.

Scan in M_χ A one-dimensional scan in M_χ spanning from 1 GeV to 500 GeV, with fixed $M_A = M_H = 600$ and $M_a = 250$ GeV, is also suggested to connect this model to a standard cosmological history. Even though the model points with where the DM particle has a

mass above 100 GeV are not within immediate reach of Run-2 searches, the measured relic density is satisfied by this model at values of DM mass around 100 GeV, as shown in section 8.

6 Sensitivity studies

In the first part of this section we present the sensitivity estimates for two of the main signatures that are sensitive to the model, the Higgs+ E_T^{miss} and the $Z+E_T^{\text{miss}}$ signatures, in the parameter scans chosen for comparison. These estimates are based on the reinterpretation of existing results that contain different amounts of public information, using generator-level simulation of the chosen grid points. In the case of the Higgs+ E_T^{miss} from [25], model-independent limits are used for the reinterpretation, while for the $Z+E_T^{\text{miss}}$ signature an estimate of the sensitivity is obtained using generator-level information from signal and background simulations.

The second part of this section briefly outlines additional signatures that are also sensitive to this model. [to be completed]

Lastly, we show the projections for the sensitivity of searches of choice for the luminosity at the end of Run-2. [to be completed]

6.1 Studies of the $h(bb) + E_T^{\text{miss}}$ signature

The sensitivity estimates of the ATLAS and CMS $h(bb) + E_T^{\text{miss}}$ searches to the 2HDM+a scenarios are based on limits on the minimally model-dependent anomalous production of 125 GeV Higgs bosons in association with E_T^{miss} in [25]. As these limits are set in terms of the observed production cross-section of non-SM events with large E_T^{miss} and a Higgs boson, they can be compared directly to the cross-sections obtained from the 2HDM+a model after folding the detection efficiency ε times the kinematic acceptance \mathcal{A} of the event selection. This approach reduces the need for computing resources to simulate further event generation steps and detector response. The variable of interest for the sensitivity study of the $h(bb) + E_T^{\text{miss}}$ searches is the ratio between the parton-level cross-section $\sigma_i^{\text{parton}, h+\text{DM}}$ times the $H \rightarrow b\bar{b}$ branching ratio $\mathcal{B}^{\text{SM}, h \rightarrow bb}$ predicted by the SM for the 125 GeV Higgs boson, multiplied by the acceptance \mathcal{A} and detector efficiency ε , and the upper observed cross-section of the anomalous production of Higgs bosons in association with E_T^{miss} ($\sigma_i^{\text{obs}, h(bb)+E_T^{\text{miss}}}$):

$$\mathcal{S}_i \equiv \frac{\sigma_i^{\text{parton}, h+\text{DM}} \times \mathcal{B}^{\text{SM}, h \rightarrow bb} \times (\mathcal{A} \times \varepsilon)_i}{\sigma_i^{\text{obs}, h(bb)+E_T^{\text{miss}}}}, \quad (6.1)$$

where is the $h \rightarrow b\bar{b}$ branching ratio predicted by the SM for the 125 GeV Higgs boson. This quantity is summed over the i E_T^{miss} bins of the search, since the model will populate more than one E_T^{miss} bin at a time. A particular point in the space is excluded by the current search if $\mathcal{S}_i \geq 1$.

The expected sensitivity of $h(bb) + E_T^{\text{miss}}$ searches to the 2HDM+a model in the (M_a, M_A) plane is shown in Figure 28. The sensitivity decreases with increasing $M_A = M_H = M_{H^\pm}$ for $M_A \geq 1$ TeV because the fraction of resonant signal events drops. This

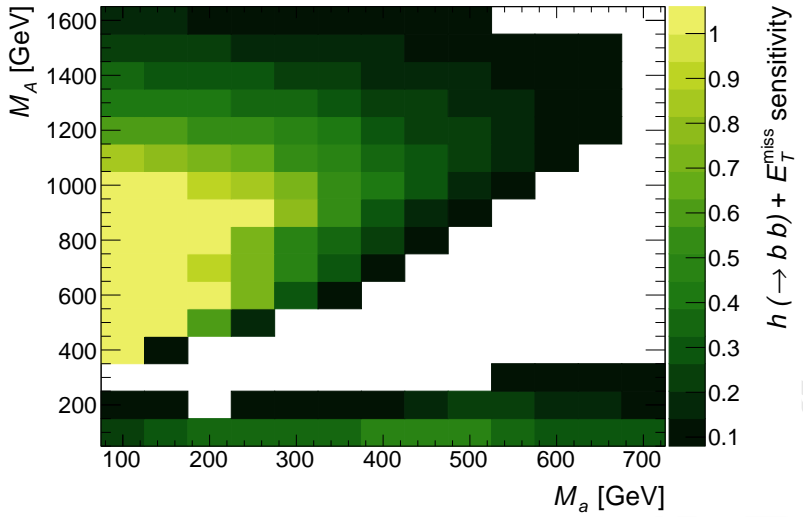


Figure 28: Sum over all E_T^{miss} -bins of the estimated sensitivity to $h \rightarrow bb + E_T^{\text{miss}}$ events as a function of (M_A, M_a) . The sensitivity, defined as the sum of Equation 6.1 over the E_T^{miss} bins, is based on the limits with reduced model dependence from Ref. [25]. The remaining parameters take the values $M_H = M_{H^\pm} = M_A$, $\sin \theta = 0.35$, $\tan \beta = 1$, $M_\chi = 10$ GeV and $\lambda_{P1} = \lambda_{P2} = \lambda_3 = 3$.

drop is caused by increasingly large Γ_A , which allows for an increasing fraction of non-resonant signal events, driven by events with very off-shell A . Near the mass diagonal $M_a = M_A$, there is little to no sensitivity. This is because the Jacobian peak moves to low E_T^{miss} for a small mass splitting $|M_A - M_a|$ (as shown in Equation 4.1, Figure 6a, and Figure 6b). Moreover, the coupling g_{Aah} is small when all Higgs bosons are nearly degenerate in mass, cf. Equation 4.12 in Ref. [2], resulting in a small total cross section and therefore a further decrease in sensitivity. The sensitivity above the mass diagonal, $M_A > M_a$, is larger than below the mass diagonal. Two parameter choices cause this asymmetry:

1. The choice of $M_A = M_H = M_{H^\pm}$ forces the neutral and charged CP -even scalars to have lower masses below the diagonal and higher masses above the diagonal, leading to configurations with a lower fraction of resonant signal events. One can use Figure 13 to exemplify this behaviour. Considering the symmetry between the two pseudoscalars, when the neutral and charged scalars $M_H = M_{H^\pm}$ are lighter than one of the two pseudoscalars (marked as A in the figure, but effectively representing a in the case of this scan because of the symmetry), one can see that non-resonant configurations are preferred. This also yields a reduced total cross-section.
2. The choice of $\sin \theta = 0.35 \neq 1/\sqrt{2}$ means that the mixing between the pseudoscalars A and a is asymmetric. A couples more strongly to SM particles than a , while the opposite happens to the DM fermion χ . The situation below the diagonal corresponds to the case of $\sin \theta = \sqrt{1 - 0.35^2} \approx 0.938$ and $M_A > M_a$. As it can be seen in

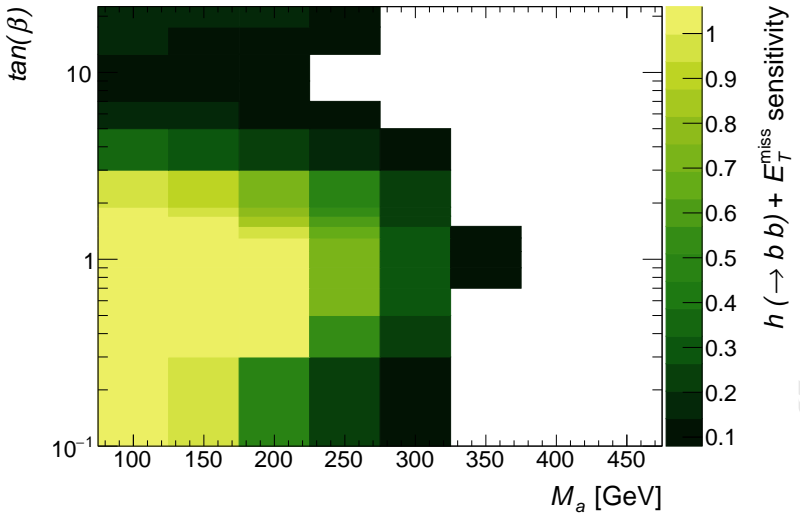


Figure 29: Sum over all E_T^{miss} -bins of the estimated signal sensitivity to $h \rightarrow bb + E_T^{\text{miss}}$ events as a function of $(M_a, \tan \beta)$. The sensitivity, defined as the sum of Equation 6.1 over the E_T^{miss} bins, is based on the limits with reduced model dependence from Ref. [25]. The remaining parameters take the values $M_H = M_{H^\pm} = M_A = 600$ GeV, $\sin \theta = 0.35$, $M_\chi = 10$ GeV and $\lambda_{P1} = \lambda_{P2} = \lambda_3 = 3$.

Figure 17a, this $\sin \theta$ configuration yields a higher fraction of non-resonant signal events with low E_T^{miss} , and correspondingly a lower sensitivity is found, as also seen in Figure 30.

The scan of the sensitivity in the $(M_a, \tan \beta)$ plane is shown in Figure 29. At very low $\tan \beta$, the Yukawa coupling to top quarks is large, and most of the signal events come from non-resonant processes, as can be seen from Figure 18. The non-resonant processes are characterised by soft E_T^{miss} , which lowers the kinematic acceptance and reduces the sensitivity of the search. For higher $\tan \beta$, the fraction of resonant events increases due to the reduced top Yukawa coupling, resulting in an increase of sensitivity. However, reducing the top Yukawa coupling also reduces the total production cross section. Above $\tan \beta \approx 1.2$, the sensitivity loss due to reduced cross section outpaces the sensitivity gain due to the resonant signal. At very high $\tan \beta (\geq 10)$, this trend is reversed again because the $\tan \beta$ enhancement⁴ of the coupling to b -quarks compensates for the small b -quark mass. At this point bb initiated processes start to dominate the production cross section and drive the increase in sensitivity.

The sensitivity as a function of $\sin \theta$ is shown in Figure 30. The sensitivity vanishes at $\sin \theta = 0$ and $\sin \theta = 1$, since those values correspond to no mixing between A and a , and thus no connection between the SM and the dark sector. For its intermediate values, the $\sin \theta$ parameter influences the couplings of the pseudoscalars to DM as well as to SM fermions, as well as the coupling strength of the trilinear scalar vertices such as g_{Aah} [2].

⁴The 2HDM+a scenario assumes a Yukawa sector of type II.

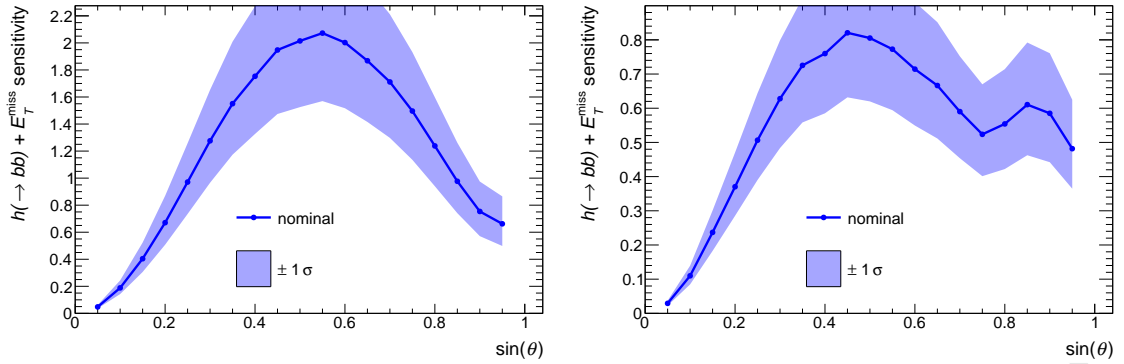


Figure 30: Sum over all E_T^{miss} -bins of the estimated signal sensitivity to $h \rightarrow bb + E_T^{\text{miss}}$ events as a function of the pseudoscalar mixing parameter $\sin \theta$, for $M_a = 200$ GeV and $M_H = M_{H^\pm} = M_A = 600$ GeV (left) as well as $M_a = 350$ GeV and $M_H = M_{H^\pm} = M_A = 1000$ GeV (right). The remaining parameters take the values $M_\chi = 10$ GeV, $\tan \beta = 1$, and $\lambda_{P1} = \lambda_{P2} = \lambda_3 = 3$. The sensitivity, defined as the sum of Equation 6.1 over the E_T^{miss} bins, as well as the uncertainty on the sensitivity (shaded blue) are based on the limits with reduced model dependence from Ref. [25] and the uncertainties described therein.

Increasing these couplings increases the total cross section, but it can also increase Γ_A and thereby decrease the resonant fraction of signal events and the overall search sensitivity. For this reason, the dependence of the sensitivity on $\sin \theta$ depends on the interplay of the couplings. As a consequence, the sensitivity curve as a function of $\sin \theta$ has more than one local maximum, as shown the right panel of Figure 30.

The sensitivity to models with varying M_χ is shown in Figure 31. Below the threshold of $M_\chi < M_a/2$, the sensitivity is constant since the E_T^{miss} distribution and the total signal cross section remain unchanged. The region at threshold $M_\chi = M_a/2 \pm 5\text{GeV}$ (shaded in red in Figure 31) is numerically unstable and should be avoided. Above threshold, the sensitivity drops rapidly because $M_\chi > M_a/2$ requires an off-shell $a^* \rightarrow \chi\chi$ decay, which is strongly suppressed by the typically narrow width of a . The width of a is substantially reduced once $a \rightarrow \chi\chi$ is kinematically inaccessible, as $\Gamma_{a \rightarrow \chi\chi}$ is a large contribution to the total width of a for $M_\chi \leq M_a/2$ [2]. There is a slight increase in sensitivity for $M_\chi \approx M_A/2$ when the $A \rightarrow \chi\chi$ decay hits its kinematic threshold, yet the absolute sensitivity remains negligible.

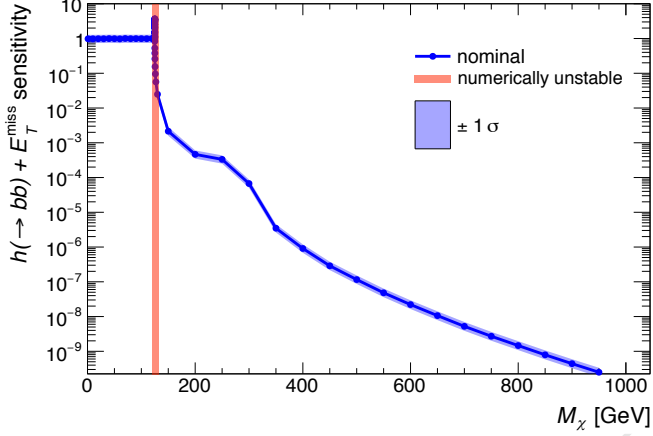


Figure 31: Sum over all E_T^{miss} -bins of the estimated signal sensitivity to $h \rightarrow bb + E_T^{\text{miss}}$ events as a function of the DM mass M_χ . The sensitivity, defined as the sum of Equation 6.1 over the E_T^{miss} bins, as well as the uncertainty on the sensitivity (shaded blue) are based on the limits with reduced model dependence from Ref. [25] and the uncertainties described therein. The remaining parameters take the values $M_a = 250$ GeV, $M_H = M_{H^\pm} = M_A = 600$ GeV, $\sin \theta = 0.35$, $\tan \beta = 1$, and $\lambda_{P1} = \lambda_{P2} = \lambda_3 = 3$. The sensitivity is constant below $M_\chi < M_a/2$, and rapidly drops for $M_\chi > M_a/2$. The sensitivity is resonantly enhanced for $M_\chi = M_a/2$.

6.2 Studies of the Z+E_T^{miss} signature

In the absence of generic limits on anomalous production of Z+E_T^{miss} events, the expected sensitivity of the Z+E_T^{miss} searches to this model is approximated comparing the number of generator-level signal events to the respective background estimates.

For the leptonic channel, the published background estimates corresponding to 36 fb⁻¹ of 13 TeV data [29] are used, and a reconstruction efficiency of 75% is assumed for signal events. The same selection cuts applied to data in [29] are applied to signal. Signal and background are binned in the same published E_T^{miss} bins, and a conservative background systematic uncertainty of 20% is assumed for $E_T^{\text{miss}} < 120$ GeV and 10% for $E_T^{\text{miss}} > 120$ GeV.

For the hadronic channel, $Z \rightarrow \nu\nu$ events in association with jets are simulated using Sherpa 2.2.1 [34] and the matrix elements are calculated up to 2 partons at next-to-leading order and up to 4 partons at leading order. Signal and background are scaled to 40 fb⁻¹ of 13 TeV data. The $Z(\rightarrow \nu\nu)$ +jets events are analyzed at particle level with the same criteria used for the signal. The number of $Z \rightarrow \nu\nu$ events after applying the cuts is increased by a factor 2 to conservatively account for the contribution from other backgrounds. This factor is based on the ATLAS dark matter search in the mono-Z hadronic signature using 3.2 fb⁻¹ of 13 TeV data ??.

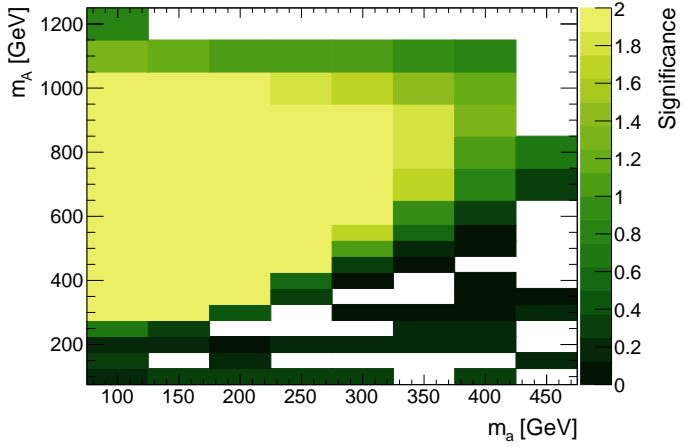


Figure 32: Expected significances for the $Z+E_T^{\text{miss}}$ leptonic signature in the (M_a, M_A) plane.

Following the Asimov approximation, the significance for individual bins is calculated as a Poisson ratio of likelihoods modified to incorporate systematic uncertainties on the background [35]:

$$Z'_{\text{bin}} = \sqrt{2 \cdot \left((s+b) \ln \left[\frac{(s+b)(b+\sigma_b^2)}{b^2 + (s+b)\sigma_b^2} \right] - \frac{b^2}{\sigma_b^2} \ln \left[1 + \frac{\sigma_b^2 s}{b(b+\sigma_b^2)} \right] \right)} \quad (6.2)$$

This metric has the advantage that it accounts for background systematics and is still valid for $s \gg b$. Similarly to the $h(bb) + E_T^{\text{miss}}$, case, the total significance is defined as the per bin significances summed in quadrature. The ATLAS and CMS experiments are expected to be sensitive to regions with significances greater than 2.

The expected sensitivity of $Z+E_T^{\text{miss}}$ searches to the 2HDM+a model in the (M_a, M_A) plane is shown in Figure 34 for the leptonic case, and Figure 35 for the hadronic case.

The sensitivity for the $Z+E_T^{\text{miss}}$ signatures in the $(M_a, \tan \beta)$ plane is shown in Figure 34

The leptonic $Z+E_T^{\text{miss}}$ search provides experimental coverage of this model for a broad part of the parameter space. The light pseudoscalar a can be probed up to mass values of ≈ 350 GeV, depending on the choice of parameters. Leptonic $Z+E_T^{\text{miss}}$ searches are mostly sensitive in the region of $\tan \beta < 4$. The hadronic $Z+E_T^{\text{miss}}$ search covers a smaller parameter space with respect to the leptonic search, but it is nevertheless complementary.

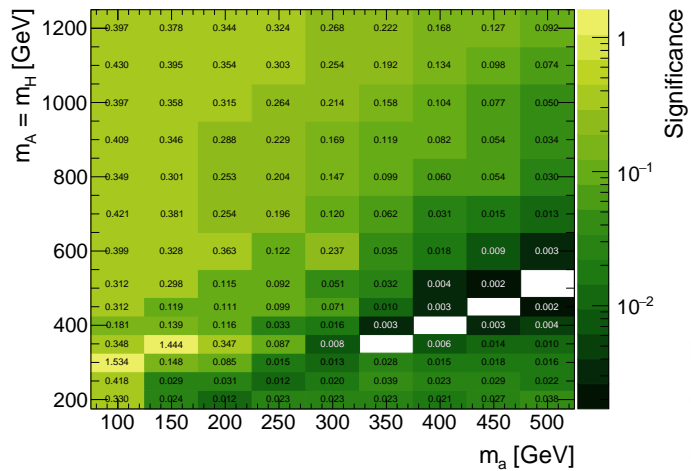


Figure 33: Expected significances for the $Z+E_T^{\text{miss}}$ hadronic signature in the (M_a, M_A) plane, combining both boosted and resolved analyses.

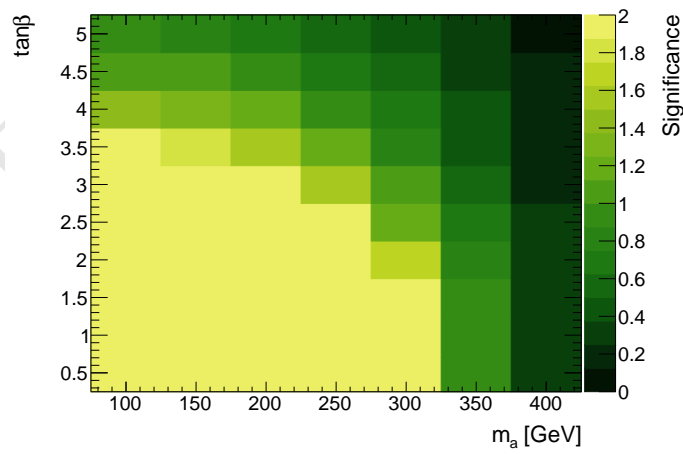


Figure 34: Expected significances for the $Z+E_T^{\text{miss}}$ leptonic signature in the $(M_a, \tan \beta)$ plane.

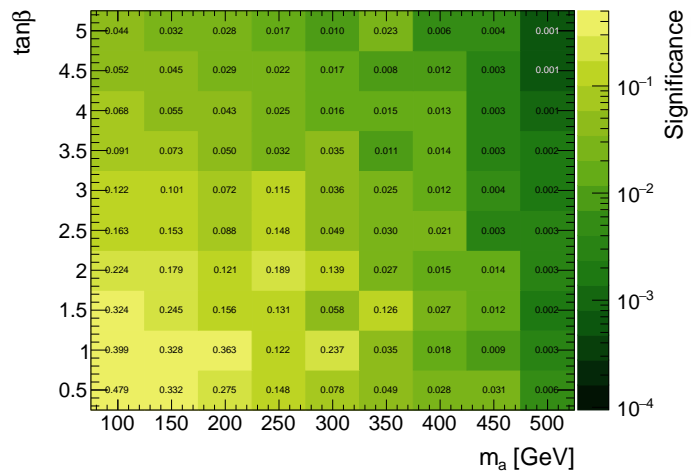


Figure 35: Expected significances for the $Z + E_T^{\text{miss}}$ hadronic signature in the $(M_a, \tan \beta)$ plane, combining both boosted and resolved analyses.

7 Sensitivity of the jet+ E_T^{miss} signature

The search for events with at least one jet and large missing transverse momentum in the final states can be also interpreted in the context of the 2HDM+a model. In this scenario the light pseudo-scalar mediator which decays in DM particles can be radiated from heavy quark loops providing such a signature. This channel is able to probe a phase space with low $\tan(\beta)$ and high $\sin \theta$ in which the cross-sections of this kind of processes are enhanced, as shown in Fig. 13 of [2]. Choosing $\tan(\beta) = 1$ for the studies in this whitepaper enhances signatures with heavy flavor quarks with respect to, as shown in the **Cross section plot to be included**, Z and H bosons

is larger than the value of the

benchmark selected in this whitepaper has a $\tan(\beta)$ that is larger than the value of approximately 0.5 that jet+ E_T^{miss} searches are currently sensitive to.

Since the models used for the interpretation of the jet+ E_T^{miss} search in terms of scalar DM mediators are the same used for the HF+ E_T^{miss} searches, it is possible to reinterpret the results of the search in terms of this model using the same rescaling strategy discussed in subsection 4.3.

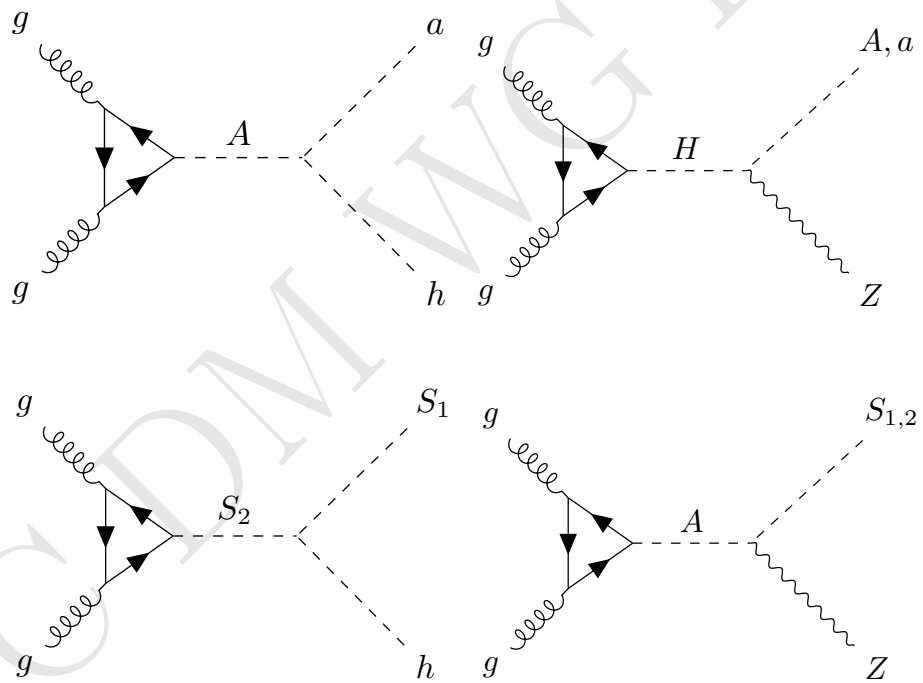


Figure 36: Feynman diagrams for resonant production signals signatures leading to mono-Z or mono-h.

7.1 Other signatures

7.1.1 Resonant Production at Collider (Comparison)

The cross section for a resonant production process, with final state X, where a spin-0 resonance S is produced and then decays, can be written as

$$\sigma(pp \rightarrow S \rightarrow X) = \frac{\Gamma(S \rightarrow X)}{M\Gamma_S} \sum_i C_i \Gamma(S \rightarrow i) = \frac{1}{Ms} \sum_i C_i \Gamma(S \rightarrow i) BR(S \rightarrow X) \quad (7.1)$$

where i are the possible initial states, C_i are weight factors that account for the protons PDFs and colour factors, and s is the center of mass energy squared $s = (13TeV)^2$.

The values of the C_i are as follows

$$C_{gg} = \frac{\pi^2}{8} \int_{M^2/s}^1 \frac{dx}{x} g(x) g\left(\frac{M^2}{sx}\right) \quad (7.2)$$

$$C_{q\bar{q}} = \frac{4\pi^2}{9} \int_{M^2/s}^1 \frac{dx}{x} \left(q(x) \bar{q}\left(\frac{M^2}{sx}\right) + q\left(\frac{M^2}{sx}\right) \bar{q}(x) \right) \quad (7.3)$$

Assuming gluon fusion production to be the dominant one, the ratio of the cross sections for the scalar and pseudoscalar model for mono-higgs and mono-Z will be

$$\frac{\sigma_S(pp \rightarrow S_2 \rightarrow \bar{\chi}\chi h)}{\sigma_P(pp \rightarrow A \rightarrow \bar{\chi}\chi h)} = \frac{\Gamma(S_2 \rightarrow gg)}{\Gamma(A \rightarrow gg)} \frac{BR(S_2 \rightarrow S_1 h)}{BR(A \rightarrow ah)} \frac{BR(S_1 \rightarrow \bar{\chi}\chi)}{BR(a \rightarrow \bar{\chi}\chi)} \quad (7.4)$$

$$\frac{\sigma_S(pp \rightarrow A \rightarrow \bar{\chi}\chi Z)}{\sigma_P(pp \rightarrow H \rightarrow \bar{\chi}\chi Z)} = \frac{\Gamma(A \rightarrow gg)}{\Gamma(H \rightarrow gg)} \frac{BR(A \rightarrow S_1 Z)}{BR(H \rightarrow aZ)} \frac{BR(S_1 \rightarrow \bar{\chi}\chi)}{BR(a \rightarrow \bar{\chi}\chi)} \quad (7.5)$$

The ideal situation to detect a mono-higgs/Z signal is to have such BR close to 1: if this is the case, the ratio of the signals becomes just the ratio of the widths

$$\frac{\sigma_S(pp \rightarrow S_2 \rightarrow \bar{\chi}\chi h)}{\sigma_P(pp \rightarrow A \rightarrow \bar{\chi}\chi h)} \sim \frac{\Gamma(S_2 \rightarrow gg)}{\Gamma(A \rightarrow gg)} \quad (7.6)$$

$$\frac{\sigma_S(pp \rightarrow A \rightarrow \bar{\chi}\chi Z)}{\sigma_P(pp \rightarrow H \rightarrow \bar{\chi}\chi Z)} \sim \frac{\Gamma(A \rightarrow gg)}{\Gamma(H \rightarrow gg)} \quad (7.7)$$

the width for a scalar or pseudoscalar particle to gluons are:

$$\Gamma(S \rightarrow gg) = \frac{g_S^2 \alpha_s^2 M}{16\pi^3} F_S \left(\frac{4m_t^2}{M^2} \right) \quad (7.8)$$

$$\Gamma(P \rightarrow gg) = \frac{g_P^2 \alpha_s^2 M}{16\pi^3} F_P \left(\frac{4m_t^2}{M^2} \right) \quad (7.9)$$

where

$$F_S(x) = x |1 + (1-x) \arctan^2 \frac{1}{\sqrt{x-1}}|^2 \quad (7.10)$$

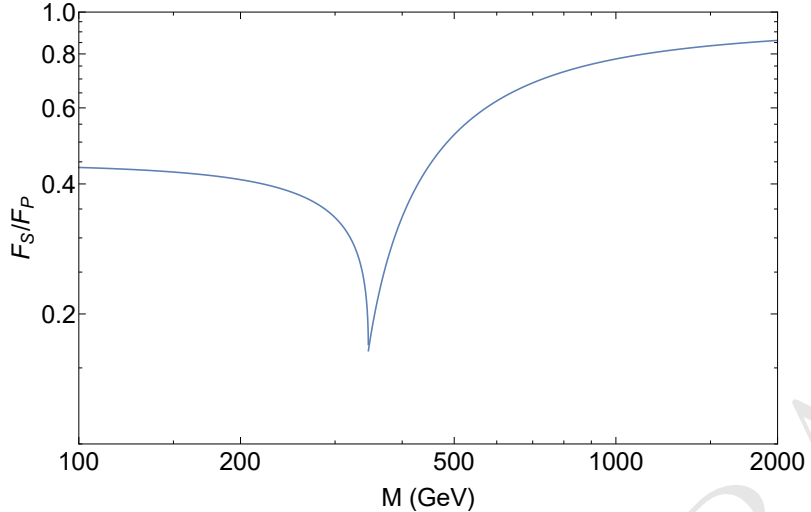


Figure 37: Ratio F_S/F_P as a function of the mass $M = M_A = M_{S_2}$.

$$F_P(x) = x \left| \arctan^2 \frac{1}{\sqrt{x-1}} \right|^2 \quad (7.11)$$

and $g_S = -y_t \sin \theta \epsilon_u$ for $S = S_2$, $g_P = y_t \epsilon_u$ for A in the scalar model, and $g_S = y_t \epsilon_u$ for $S = H$, $g_P = y_t \cos \theta \epsilon_u$ for A in the PS model. Note that the definition of the mixing angle is reversed in the scalar model comparing to the PS. So assuming equivalent mixing angle configurations, Eq. 7.6 and 7.7 reduce to

$$\frac{\sigma_S(pp \rightarrow S_2 \rightarrow \bar{\chi}\chi h)}{\sigma_P(pp \rightarrow A \rightarrow \bar{\chi}\chi h)} \sim \frac{F_S(\frac{4m_t^2}{M^2})}{F_P(\frac{4m_t^2}{M^2})} < 1 \quad (7.12)$$

$$\frac{\sigma_S(pp \rightarrow A \rightarrow \bar{\chi}\chi Z)}{\sigma_P(pp \rightarrow H \rightarrow \bar{\chi}\chi Z)} \sim \frac{F_P(\frac{4m_t^2}{M^2})}{F_S(\frac{4m_t^2}{M^2})} > 1 \quad (7.13)$$

The ratio F_S/F_P is shown in Fig. 37 as a function of the mass $M = M_A = M_{S_2}$.

8 Connection with cosmology

8.1 Pseudoscalar

An important requirement for models of dark matter is their consistency with existing astrophysical observations, namely the observed dark matter relic density. The relic density is driven by the annihilation cross-section of dark matter into SM particles. For a given model of dark matter-SM interactions, the annihilation cross-section is fully defined and a calculation of the resulting relic density can be performed.

8.2 Technical setup

The MADDM [36, 37] plugin for MG5_aMC@NLO is used to calculate the present-day relic density for this model. By modeling the thermal evolution of the cross-section during

the expansion of the early universe, the time of freeze-out is determined. All tree-level annihilation processes are taken into account, and the Yukawa couplings of all fermions are taken to be non-zero. The Feynman diagrams of annihilation processes taken into account in this calculation are shown in Fig. 38. Generally, the annihilation proceeds via single or double s-channel exchange of the pseudoscalars a and A , with subsequent decays. Since MADDM uses only tree-level diagrams, contributions from off-shell pseudoscalars can only be taken into account for the case of single s-channel mediation with direct decay of the pseudoscalar to SM fermions. If the pseudoscalar instead decays to other bosons or if the annihilation proceeds through double s-channel diagrams, the outgoing bosons are taken to be on-shell and their decays are not simulated.

In all scans presented here, the common parameter choices $\sin(\theta) = 0.35$, $m_h = 125\text{GeV}$, $g_\chi = 1$, $\lambda_i = 3$ are used.

8.3 Results

The relic density is shown for a scan in the M_a - M_χ plane in Fig. 39. For small values of M_χ below the mass of the top quark, DM is mostly overabundant. In this regime, annihilation to quarks is suppressed by the small Yukawa couplings of the light fermions. The observed relic density can only be achieved for $M_\chi \approx M_a/2$, where annihilation is resonantly enhanced, or for $M_\chi \approx (M_a + M_h)/2$, close to the threshold for the $\chi\chi \rightarrow ha$ process. Above the top threshold, annihilation into fermions becomes very efficient and DM is underabundant. As M_χ increases further, annihilation via single s-channel diagrams is increasingly suppressed and the relic density rises again. The observed density is reproduced again for $M_\chi \approx 1\text{TeV}$ at low M_a . For values of M_a beyond the LHC reach of a few TeV, the allowed parameter region at the top threshold $M_\chi \approx m_{\text{top}}$ stays independent of the value of M_a , indicating that a DM candidate that is mass degenerate with the top quark cannot be excluded by LHC searches alone.

The dependence of the relic density on the choice of M_χ is further explored by performing a one-dimensional scan, as shown in Fig. 40. The relic density shows clear structures corresponding to the previously discussed regions of resonant enhancement, as well as kinematic boundaries. Overall, the behavior is dominated by the low- M_χ suppression of the annihilation cross-section, the resonant enhancement at $M_\chi = M_a/2$ and the kinematic top thresholds. Other effects, such as resonant enhancement of $\chi\chi \rightarrow A$ annihilation are present, but only have small effects.

As a comparison to the collider constraints, the relic density for the M_a - M_A/M_H scan described in the experimental sections, is shown in Fig. 41. For the scan parameters chosen here, the regions where the relic density approximately coincides with the experimental value are located at relatively small values of $M_a < 30\text{GeV}$ or $M_A = M_H < 30\text{GeV}$, which may be in conflict with constraints from measurements of the properties of $h(125)$. The exact location of the allowed region is driven by the choice of M_χ , to which the collider searches are largely insensitive as long as the chosen value is small enough to allow DM production. Therefore, M_χ may be freely tuned to yield the desired value of the relic density without spoiling the experimental constraint. The corresponding $\tan\beta$ dependent scans are shown in Fig. 42. The choice of $\tan\beta$ acts as an overall modifier of the annihilation

cross-section and thus the relic density, and the effect is largely independent of the choice of M_a and M_χ . For a choice of $\tan \beta \approx 0.6$, the relic density becomes maximal and steadily decreases for larger and smaller values of $\tan \beta$. In the M_χ dependent scan, the reduction of the relic density at low (≈ 0.1) and high (≈ 3) values of $\tan \beta$ notably leads to the disappearance of the allowed and overabundant island around $M_\chi \approx M_a/2$.

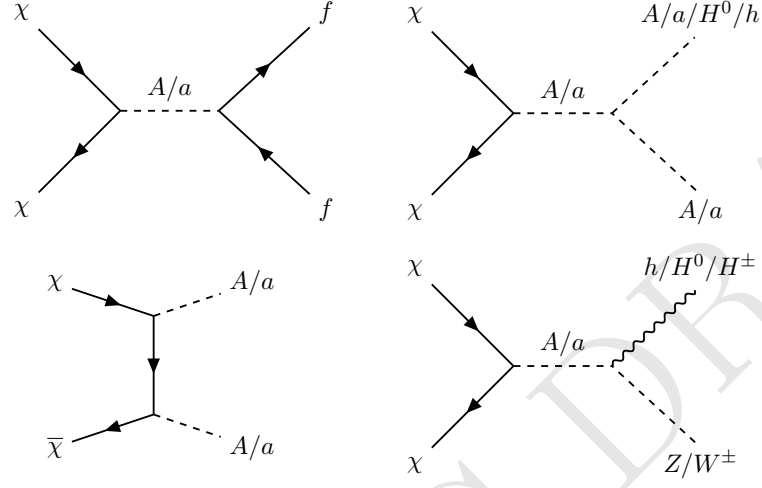


Figure 38: Annihilation diagrams taken into account in the relic density calculation.

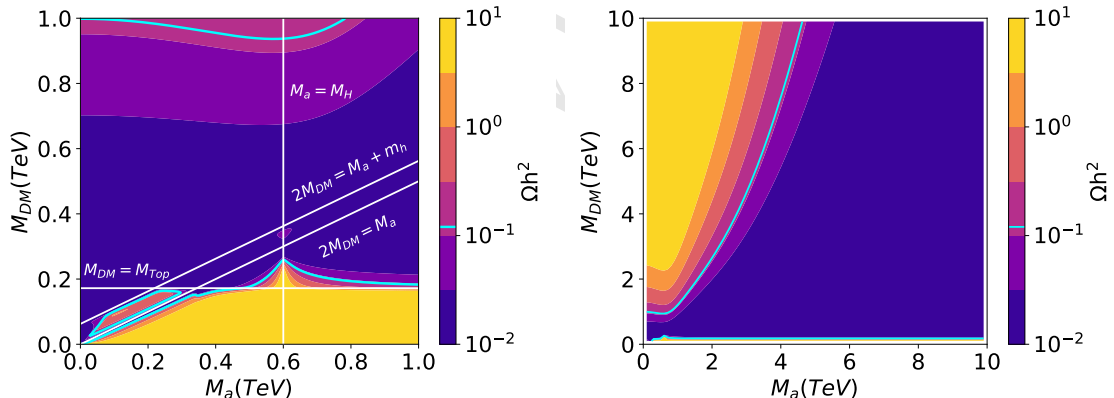


Figure 39: Predicted relic density for a two-dimensional scan of M_χ and M_a . The other parameters of the model remain fixed with $m_H = m_A = m_{H^\pm} = 600$ GeV and $\tan \beta = 1$, as well as the default choices described in the text. The color scale indicates the relic density, the cyan solid line shows the observed value of $\Omega h^2 = 0.12$. The color scale is truncated at its ends, i.e. values larger than the maximum or smaller than the minimum are shown in the same color as the maximum/minimum. While the left focuses on the mass region relevant to collider searches, the right panel shows the development of the relic density for a larger mass region.

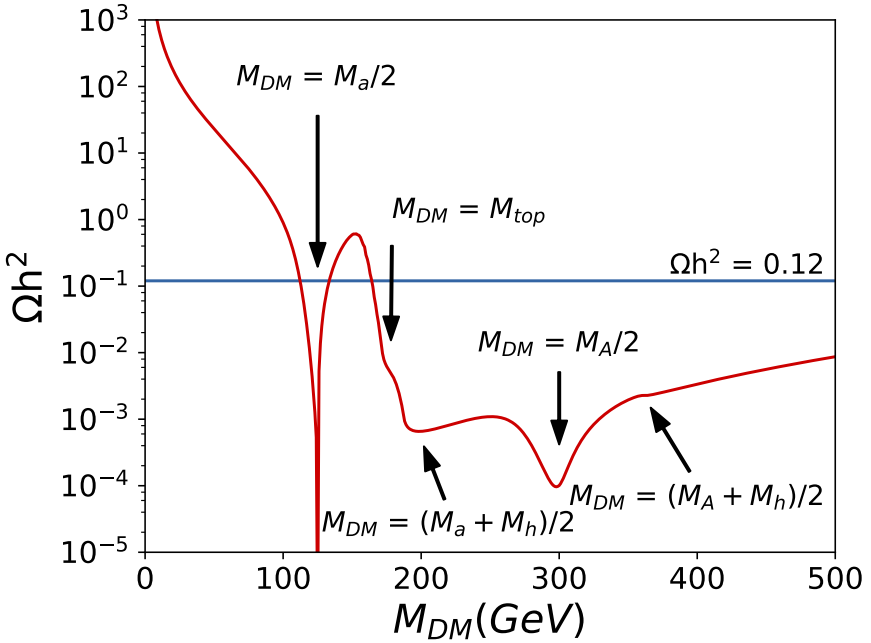


Figure 40: Relic density for a one-dimensional scan of M_χ . The other parameters of the model remain fixed with $m_H = m_A = m_{H^\pm} = 600$ GeV, $M_a = 250$ GeV and $\tan \beta = 1$, as well as the default choices described in the text. Various kinematic thresholds and regions of resonant enhancement are visible. Consistency with the observed value of $\Omega h^2 = 0.12$ is mainly controlled by the resonant enhancement of $\chi\chi \rightarrow a$, as well as the onset of $\chi\chi \rightarrow t\bar{t}$.

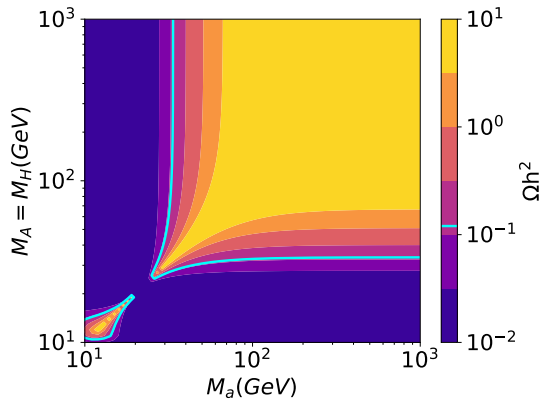


Figure 41: Predicted relic density for a two-dimensional scan of M_a and $M_A = M_H = M_{H^\pm}$. The other parameters of the model remain fixed with $M_\chi = 10$ GeV, $\tan \beta = 1$ as well as the default choices described in the text. The color coding is identical to Fig. 39.

8.4 Scalar

The 2HDM+S scenario has multiple DM annihilation channels. There are tree-level annihilations to fermion-antifermion pairs, scalars (the SM Higgs, the two neutral scalars,

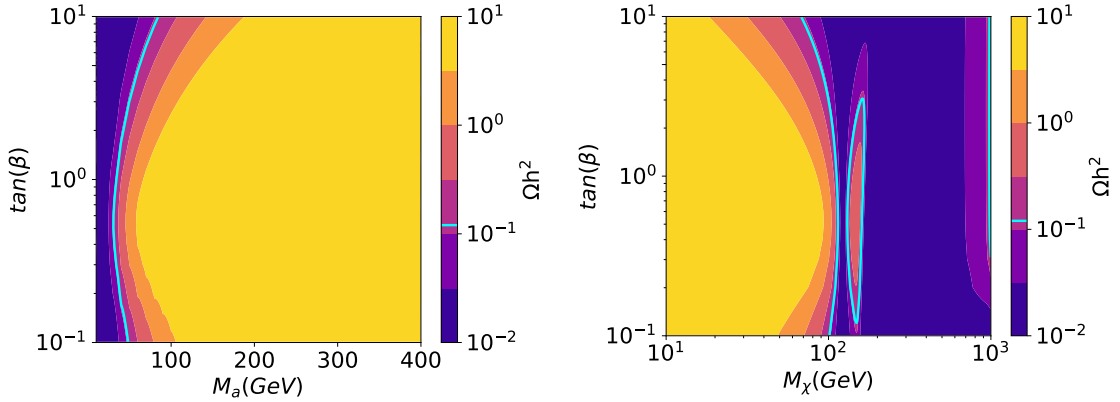


Figure 42: Predicted relic density for a two-dimensional scan of $\tan \beta$ and M_a (left), M_χ (right). In the case of the M_χ (M_a) dependent scan, $M_a = 250 \text{ GeV}$ ($M_\chi = 10 \text{ GeV}$) is used. The other parameters of the model remain fixed with $m_H = m_A = m_{H^\pm} = 600 \text{ GeV}$, as well as the default choices described in the text. The color coding is identical to Fig. 39.

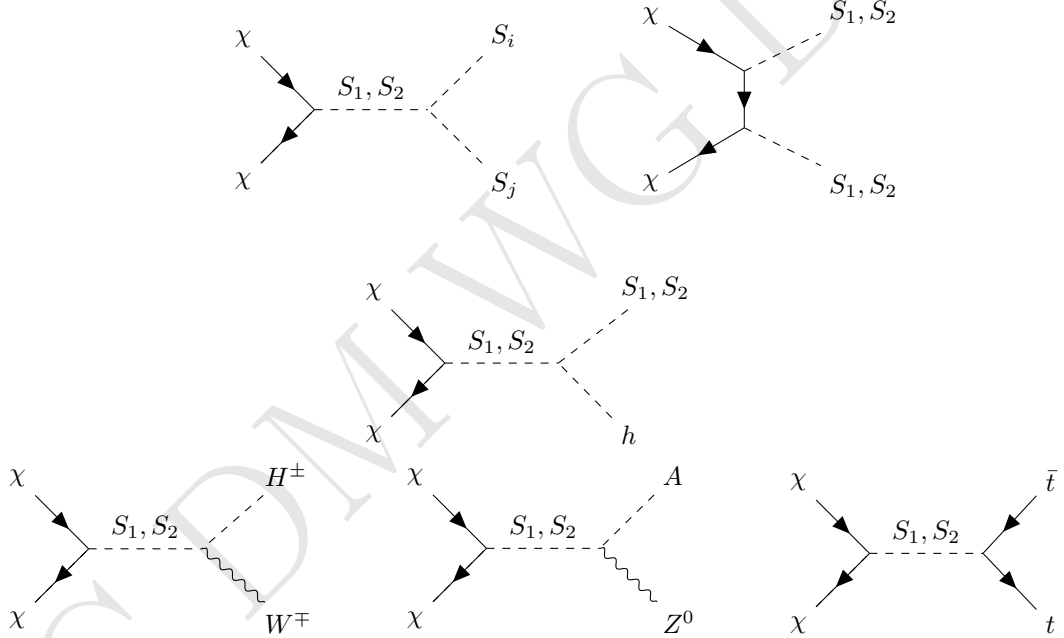


Figure 43: Dominant DM annihilation channels, where (S_i, S_j) is one of these scalar final states: (S_1, S_1) , (S_1, S_2) , (S_2, S_2) , (H^+, H^-) , (A, A) .

the pseudoscalar, and the charged scalars) and/or the electroweak gauge bosons, namely: $\bar{\chi}\chi \rightarrow \bar{f}f$, S_1S_1 , S_2S_2 , S_1S_2 , H^+H^- , H^+W^- , AA , AZ , S_1h , and S_2h – these are shown in Fig. 43. This is to be compared with a single mediator model in which only the $\bar{f}f$ and SS channels are present. Note that since all diagrams involve χ -scalar vertices (including those with gauge boson final states) they are all p -wave processes. As such, while we will easily be able to find parameters that accommodate the observed relic density, there will

be no constraints arising from indirect detection because the p -wave annihilation processes are highly velocity suppressed in the late universe.

If the DM particle is relatively light, such that annihilation to the scalars and electroweak bosons is kinematically forbidden ($m_\chi \lesssim 80\text{GeV}$), the only annihilation channels that remain open are the fermionic ones. This case is heavily constrained, as the dominant annihilation channel is then $b\bar{b}$, which is suppressed by the bottom Yukawa coupling and thus usually requires resonant enhancement to accommodate the correct relic density.

If, instead, the DM particle is heavy enough to annihilate to the Higgs, electroweak gauge bosons and/or the new scalars, then these final states will likely dominate due to the Yukawa suppression of annihilations to fermions (top excluded). Because all of these annihilations are governed by scalar and electroweak couplings – and exist due to gauge invariance, independent of the Yukawa couplings of the second doublet – they are also present, for example, in the limit where the second doublet is inert. This ability to produce the correct relic abundance independent of Yukawa structure means that DM can be adequately produced while avoiding any Yukawa dependent constraints (e.g. DD, neutral meson mixing, $b \rightarrow s\gamma$, $\mu \rightarrow e\gamma$, etc.).

We implemented the model in FeynRules⁵ [38, 39] and output the model with the CALCHEP interface [40]. We then used `micrOMEGAs` [41] to perform the relic density calculation, where we included 3 body final states with off-shell gauge bosons. We also double checked the results by calculating the annihilation cross sections, which are reported in [10]. In the case where the parameter values are away from resonances and annihilation thresholds, one can use the wave expansion of the cross sections. The p-wave coefficients of this expansion are also reported in [10].

Sommerfeld enhancement can significantly increase the DM annihilation cross section [42–44], provided at least one of the scalars is both sufficiently light compared to the DM, and strongly coupled to the DM particle. In practice, for the parameter range we consider, this leads to $\mathcal{O}(1)$ corrections to the cross section; a discussion is provided in [10].

The independent parameters present in the model are

$$m_\chi, \quad M_{S_1}, \quad M_{S_2}, \quad y_\chi, \quad \hat{\lambda}_4, \quad \hat{\lambda}_5, \quad \hat{\lambda}_{hHS}, \quad \hat{\lambda}_{HHS}, \quad \epsilon_u \quad \text{and} \quad \epsilon_d. \quad (8.1)$$

This set of parameters, through the minima condition and the diagonalization relations, together with the additional constraint $m_\chi = y_\chi v_s$, determine all other parameters of the model⁶. The scan is performed in the following range:

$$70\text{GeV} < m_\chi < 1\text{TeV}, \quad (8.2)$$

$$70\text{GeV} < M_{S_1} < M_{S_2} < 2\text{TeV}, \quad (8.3)$$

$$0 < y_\chi < 2, \quad (8.4)$$

$$|\hat{\lambda}_{hHS}| < 2, \quad (8.5)$$

$$|\hat{\lambda}_{HHS}| < 4, \quad (8.6)$$

⁵The FeynRules model file used is publicly available in the FeynRules model database.

⁶The phase of the DM Yukawa can always be reabsorbed, so one can chose y_χ and v_s to be both real and positive.

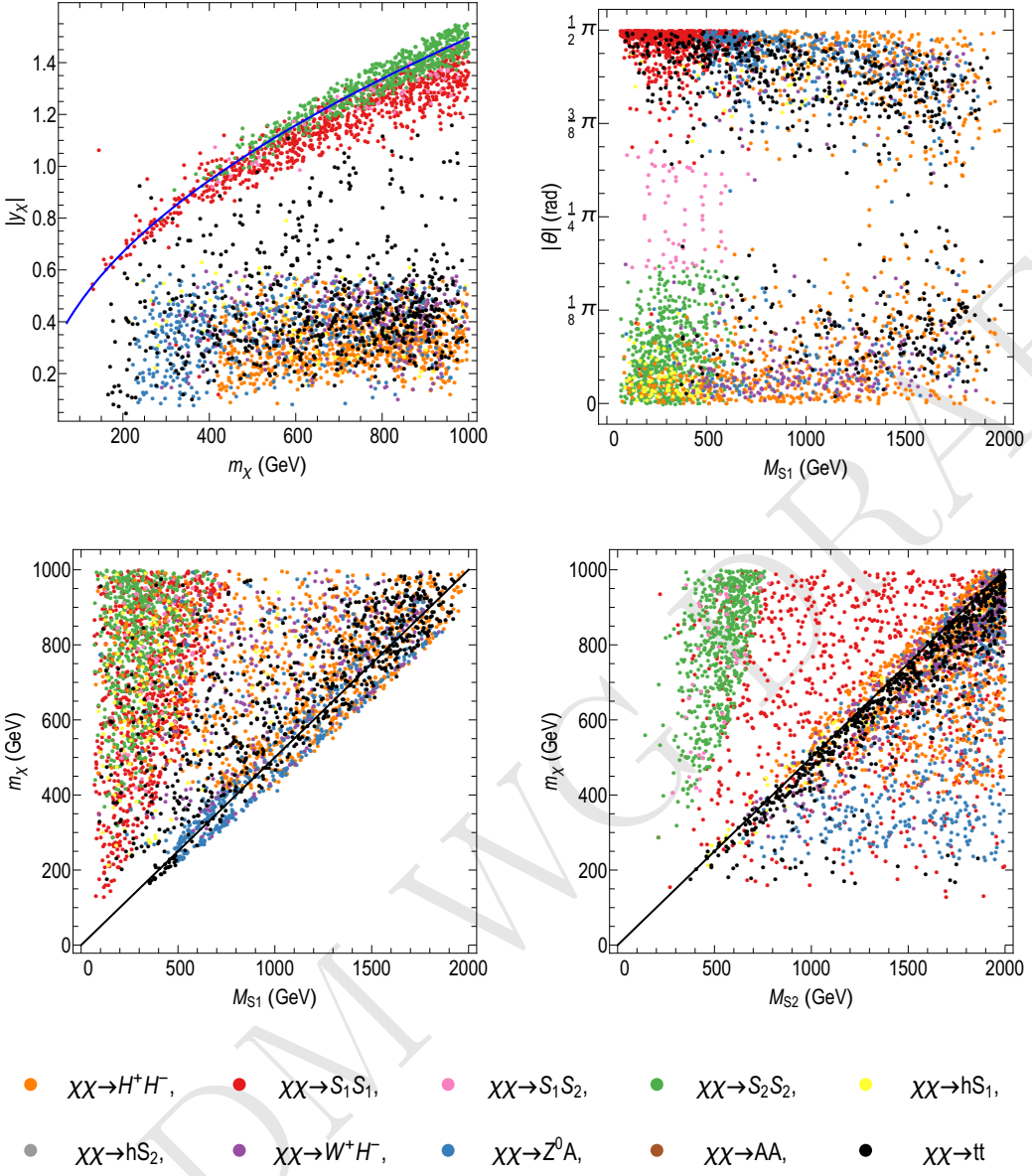


Figure 44: Points of our scan of parameter space that produce the correct relic density. The colours represent the dominant annihilation channel, as shown above. 15000 points are taken that survive the constraints, and of them only 25% of the H^+H^- channel and 10% of the S_1S_1 channel are shown for clarity. The black line in the lower panels indicate $m_\chi = 2M_{S_1, S_2}$, which is the resonance condition for the s-channel annihilation processes. The blue line in the top left panel represents the scaling expected for a cross section of $\langle\sigma v\rangle \sim y_\chi^4 v^2 / 16\pi^4 m_\chi^2$ which, in this model, applies to a pure $\bar{\chi}\chi \rightarrow S_i S_i$ scenario.

$$0 < \epsilon_u < 1, \quad (8.7)$$

while for $\hat{\lambda}_4$ and $\hat{\lambda}_5$ we scan over the region shown in [10]. These ranges for the couplings were chosen so that most of the points will satisfy unitarity and perturbativity bounds,

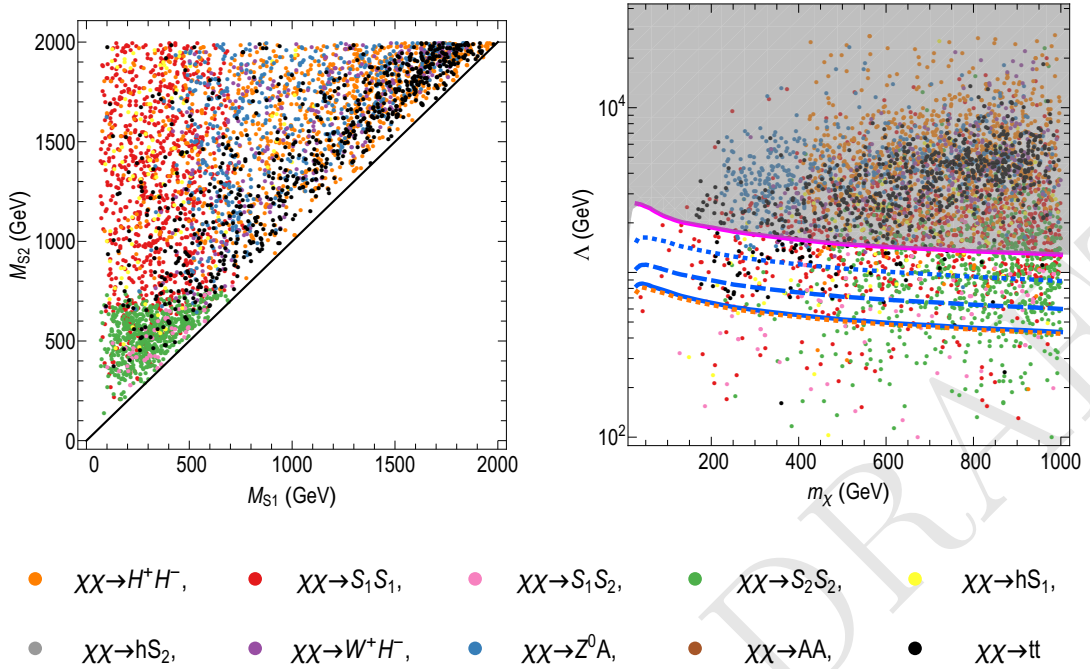


Figure 45: Points of our scan of parameter space that produce the correct relic density. The colours represent the dominant annihilation channel, as shown above. 15000 points are taken that survive the constraints, and of them only 25% of the H^+H^- channel and 10% of the S_1S_1 channel are shown for clarity. Λ is the effective cut-off scale for the DD effective operator; the dotted orange line represents the constraint from the LUX 2016 results [45], the solid blue represents the XENON1T experiment [46], the dashed blue the projection for the XENON1T experiment with $2t \cdot y$ of data taking, the dotted blue the projection for the XENONnT experiment with $20t \cdot y$ of data taking [47], and the magenta is the DD sensitivity at the “neutrino floor”[48].

which was checked via the scalar scattering matrices as in [3]. To achieve the right relic density, we will see that it will be in general necessary to have $m_\chi \gtrsim M_{S_1}$, and the inequality is strictly required for DM masses below the top mass, as otherwise all considered annihilation channels are closed. In this low DM mass region, however, one needs to take into account Higgs invisible constraints [49, 50]: 2-body decays forbid the region $2m_\chi < m_h$ and $2M_{S_1} < m_h$, while considering 3-body decays as well further pushes up the lower bound on M_{S_1} to nearly 100GeV. The Higgs invisible decays constraints can only be avoided in the $\theta \rightarrow \pi/2$ limit, but in such case the model approaches a decoupled dark sector which is phenomenologically uninteresting⁷. Taking into account these considerations, we have chosen in our scan a conservative lower bound for the DM mass and for the lightest scalar

⁷Relic density requirement can be satisfied in the limit of a decoupled dark sector, in which dark matter annihilates to light dark scalars. However, there would be no signals in collider or direct detection experiments. Moreover, indirect detection is prevented by the p-wave nature of annihilation to scalars, even if small couplings to the SM are included.

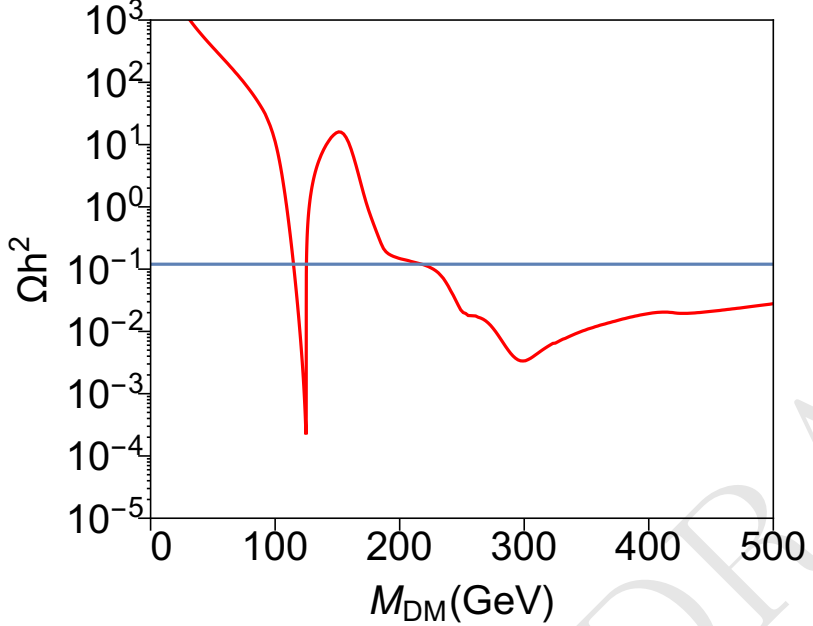


Figure 46: One-dimensional scan of the parameter space. We fix all other parameters, see the text for more details.

of 70GeV. Points are selected if they have a relic density between $0.1 < \Omega h^2 < 0.14$ and satisfy all bounds from flavour, unitarity, perturbativity, tree level vacuum stability, and DD constraints.

The relic density is insensitive to the value of ϵ_d , while the DD results depend on the relationship ϵ_d and ϵ_u . We set $\epsilon_d = \epsilon_u$ for the scans presented in Fig. 44 and Fig. 45 (with the exception of the right panel of Fig. 45, which enforces no DD constraint and hence has no ϵ_d dependence).

We have chosen to define S_1 to be the lighter of the 2 scalars, and allow θ to range from 0 to $\pi/2$. As one can always switch the two scalars by sending $\theta \rightarrow \pi/2 - \theta$, an equivalent choice would be to take $0 < \theta < \pi/4$ without requiring any mass ordering.

In Fig. 46 we show the value of the relic density obtained through thermal freezeout in a one-dimensional scan, where we kept fixed all parameters except the DM mass. We fix $M_{S_1} = 250\text{GeV}$, $M_{S_2} = M_A = M_{H^+} = 600\text{GeV}$, $\cos \theta = 0.35$ (equivalent to $\sin \theta = 0.35$ for the PS model), $y_\chi = 1$,

These choices of parameters, along with alignment conditions and $m_\chi = v_s y_\chi$, then fix

$$v_s = \frac{m_\chi}{y_\chi} = m_\chi, \quad (8.8)$$

$$\lambda_1 = \frac{m_h^2}{v^2} \sim 0.258, \quad (8.9)$$

$$\lambda_s = \frac{1}{4v_s^2} (M_a^2 + M_A^2 + (M_A^2 - M_a^2) \cos(2\theta)) \sim \frac{222.4^2 \text{GeV}^2}{m_\chi^2}, \quad (8.10)$$

$$\lambda_{12s} = \frac{(M_{S_1}^2 - M_{S_2}^2) \sin(2\theta)}{2vv_s} \sim -\frac{396.5 \text{GeV}}{m_\chi}, \quad (8.11)$$

$$\lambda_4 = \frac{1}{2v^2} (2M_A^2 - 4M_{H^+}^2 + M_{S_1}^2 + M_{S_2}^2 + (M_{S_1}^2 - M_{S_2}^2) \cos(2\theta)) \sim -0.60, \quad (8.12)$$

$$\lambda_5 = -\frac{1}{2v^2} (2M_A^2 - M_{S_1}^2 - M_{S_2}^2 + (M_{S_2}^2 - M_{S_1}^2) \cos(2\theta)) \sim -0.60, \quad (8.13)$$

$$\lambda_3 = \lambda_1 - \lambda_4 - \lambda_5 \sim 1.46. \quad (8.14)$$

9 Comparisons with non-collider experiments

9.1 Direct detection

The DD constraints for the scalar and pseudoscalar mediator scenario are very different. While the scalar features an unsuppressed SI scattering cross section, the pseudoscalar cross section is highly suppressed at tree level such that the dominant contribution arises from loop graphs.

9.1.1 Scalar

We will generate DD constraints using the 2016 LUX [45] and XENON1T [46] data, via an effective operator approach using tools from [51]. The scattering of DM with nuclei will be dominated by the tree-level exchange of S_1 and S_2 , resulting in a spin-independent scattering cross section. The only relevant nucleon operator is

$$O_1^N = \bar{\chi}\chi \bar{N}N, \quad (9.1)$$

and, by integrating out the mediators, we obtain a coefficient of [3]

$$c_N = m_N \frac{y_\chi \cos \theta \sin \theta}{v} \left(\frac{1}{M_{S_1}^2} - \frac{1}{M_{S_2}^2} \right) \left(f_{T_u}^N \epsilon_u + \epsilon_d \sum_{q=d,s} f_{T_q}^N + \frac{2}{9} f_{T_g} \frac{2\epsilon_u + \epsilon_d}{3} \right). \quad (9.2)$$

As there are contributions from exchange of the two scalars, with a relative negative sign, there is the possibility for destructive interference when the masses of S_1 and S_2 are comparable. In addition, depending on the choice of Yukawa structure, it is possible to have destructive interference between the up-type quarks and the down-type quarks in the nucleon. For the Type I and Type II Yukawa structure, the coefficients become

$$c_N^{\text{type I}} = m_N \frac{y_\chi \cos \theta \sin \theta}{v \tan \beta} \left(\frac{1}{M_{S_1}^2} - \frac{1}{M_{S_2}^2} \right) \left(\sum_{q=u,d,s} f_{T_q}^N + \frac{2}{9} f_{T_g} \right), \quad (9.3)$$

$$c_N^{\text{type II}} = m_N \frac{y_\chi \cos \theta \sin \theta}{v} \left(\frac{1}{M_{S_1}^2} - \frac{1}{M_{S_2}^2} \right) \left(f_{T_u}^N \cot \beta - \tan \beta \sum_{q=d,s} f_{T_q}^N + \frac{2}{9} f_{T_g} \frac{2 \cot \beta - \tan \beta}{3} \right). \quad (9.4)$$

For the Type II scenario, we see that the presence of destructive u - d interference is clearly visible in the right-hand bracket of 9.4. There is no such interference for Type I. If we adopt the values of f_{T_i} obtained by [52], we find that a ratio of $\epsilon_u \sim -1.6\epsilon_d$ (corresponding to $\tan \beta = \sqrt{|\frac{\epsilon_d}{\epsilon_u}|} \sim 0.8$ in a Type II scenario) will result in exact cancellation of the DD signal.

In Figure 47 we show the current DD exclusion from LUX [45] and XENON1T[46] together with the projections for XENON1T, XENONnT projections [47]. We also show the sensitivity for a cross section equivalent to the “neutrino floor” [48]. We find that DD excludes significant parameter space, unless the scalar masses are approximately degenerate. This can be seen in all 4 panels of Figure 47 where we see a narrow allowed region near $M_{S_1} \sim M_{S_2}$, between excluded regions at higher and lower M_{S_1} values. The excluded region in the upper LH plot (Type I) is somewhat larger than in the lower LH plot (Type II) lower due to the additional interference effect for the latter. Increasing $\tan \beta$ weakens the constraints for Type I because $|\epsilon_d| = |\epsilon_u| = 1/\tan \beta$ (upper right) and strengthens them for Type II because $|\epsilon_d| = |1/\epsilon_u| = \tan \beta$ (lower right).

9.2 Pseudoscalar

At tree level, the spin-independent scattering cross section is absent. The spin-independent cross section is non-zero, but highly suppressed due to a dependence on q_{tr}^4 . At loop level, however, a spin-independent cross section is generated through the diagrams in Fig. 48. The triangle diagrams in the left panel of Fig. 48 are proportional to m_q while the box diagrams in the central and right panels of Fig. 48 are proportional to m_q^3 , thus the box diagrams are sub-leading as found in [4] (except for Type II with $\tan \beta \gtrsim 50$). The triangle diagram does not depend on the Yukawa sector of the 2HDM. ** cite our paper in preparation**

Similarly as in the scalar model, in the PS model the mixing arises through a term $ib_P P\Phi_1^\dagger \Phi_2 + h.c.$. The resulting mixing angle is defined by

$$b_P = -\frac{(M_A^2 - M_a^2) \sin 2\theta}{2v} \quad (9.5)$$

The low energy effective operator generated at 1 loop is

$$\mathcal{L}_{eff} = -\frac{y_\chi^2 m_q m_\chi}{16\pi^2 m_h^2 v^2} G \left(\frac{m_\chi^2}{M_A^2}, \frac{m_\chi^2}{M_a^2}, \frac{m_h^2}{m_\chi^2}, \theta \right) \bar{\chi} \chi \bar{q} q \quad (9.6)$$

$$G(x, y, z, \theta) = F_1(x) \sin^2 \theta \hat{\mu}_{AAh} + F_1(y) \cos^2 \theta \hat{\mu}_{aah} + F_2(x, y) \sin 2\theta \hat{\mu}_{Aah} \quad (9.7)$$

$$F_1(x) = \int_0^1 dz \frac{x(1-z)z}{xz^2 - z + 1} = \frac{(6x-2) \log\left(\frac{\sqrt{1-4x}+1}{2\sqrt{x}}\right) + \sqrt{1-4x}((x-1)\log(x) - 2x)}{2\sqrt{1-4x}x} \quad (9.8)$$

$$\begin{aligned} F_2(x, y) &= \int_0^1 dz \frac{xyz \log\left(\frac{xyz^2-yz+y}{xyz^2-xz+x}\right)}{y-x} \\ &= \frac{1}{4xy(x-y)} \left(x^2((2y-1)\log(y) - 2y) + x^2\sqrt{1-4y} \left(\log(4y) - 2\log\left(\sqrt{1-4y}+1\right) \right) \right. \\ &\quad \left. - 2xy^2(\log(x)-1) + y^2\log(x) + \sqrt{1-4xy}^2 (2\log(\sqrt{1-4x}+1) - \log(4x)) \right) \end{aligned} \quad (9.9)$$

where the coefficients μ are given in terms of either the couplings in the $\Phi_{1,2}$ basis or in the $\Phi_{h,H}$ basis (indicated as $\hat{\mu}$), respectively:

$$\mu_{AAh} = z \left(\cos^2 \theta - \frac{2\lambda_3 v^2}{m_h^2} \right), \quad (9.11)$$

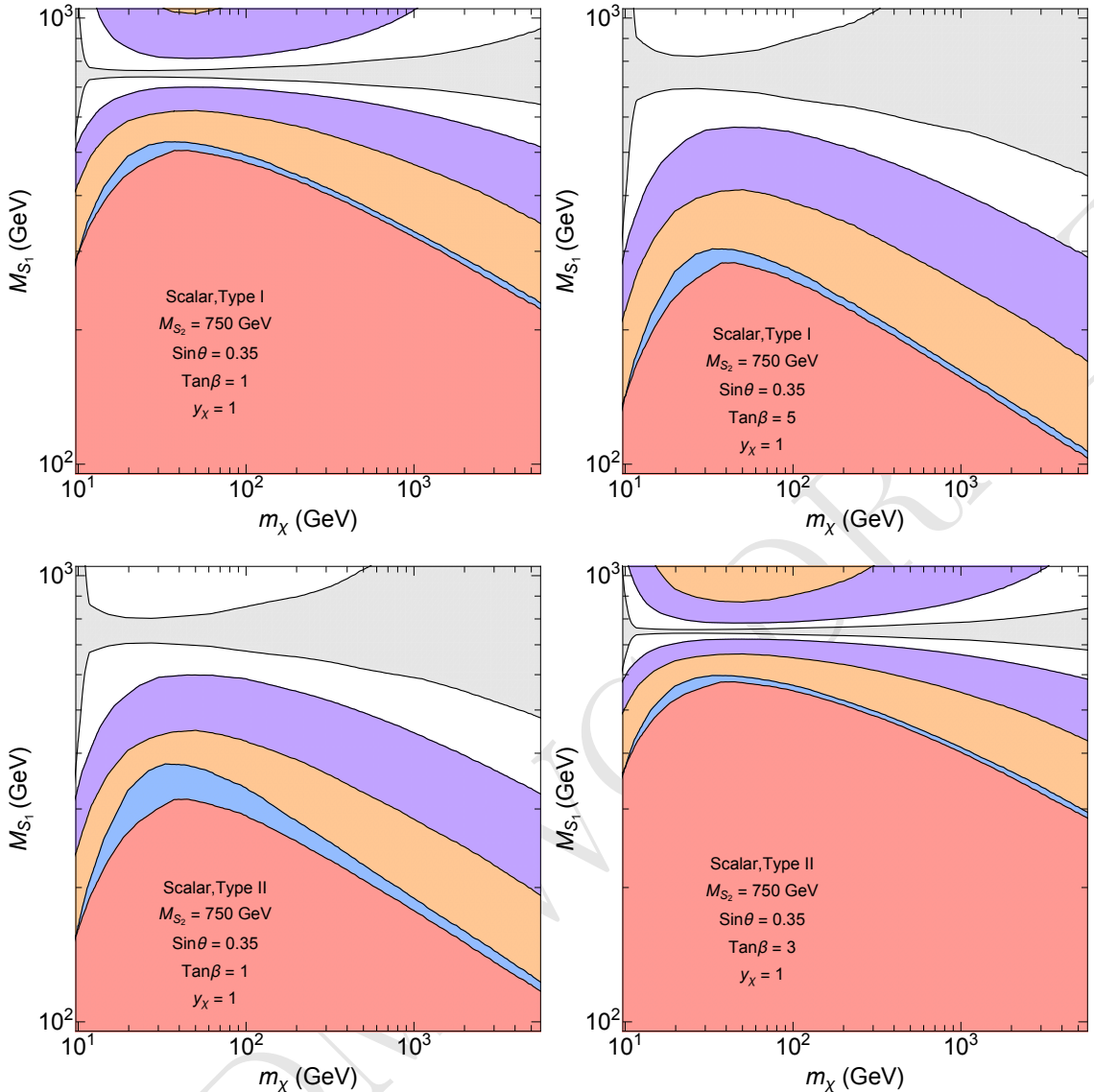


Figure 47: DD exclusion and projections for various experiments for the Scalar model. The various regions refer, in order, to LUX [45], XENON1T[46], XENON1T and XENONnT projections [47], and neutrino background [48]. The mixing angle is set to $\sin \theta = 0.35$, but results are equivalent also for $\cos \theta = 0.35$, while $M_{S_2} = 750\text{GeV}$ in all the panels.

$$\mu_{Aah} = -\frac{1}{2} \sin(2\theta) \left(\frac{1}{x} - \frac{1}{y} + z \right), \quad (9.12)$$

$$\mu_{aah} = 2 \sin^2(\theta) \left(\frac{1}{x} - \frac{1}{y} + \frac{z}{2} \right) - z \frac{2\lambda_3 v^2}{m_h^2}, \quad (9.13)$$

$$\hat{\mu}_{AAh} = -\frac{1}{2} \sin^2(2\theta) \left(\frac{1}{x} - \frac{1}{y} \right) - z \frac{\hat{\lambda}_{34-5} v^2}{m_h^2} \cos^2 \theta - z \frac{2\hat{\lambda}_{P_1} v^2}{m_h^2} \sin^2 \theta, \quad (9.14)$$

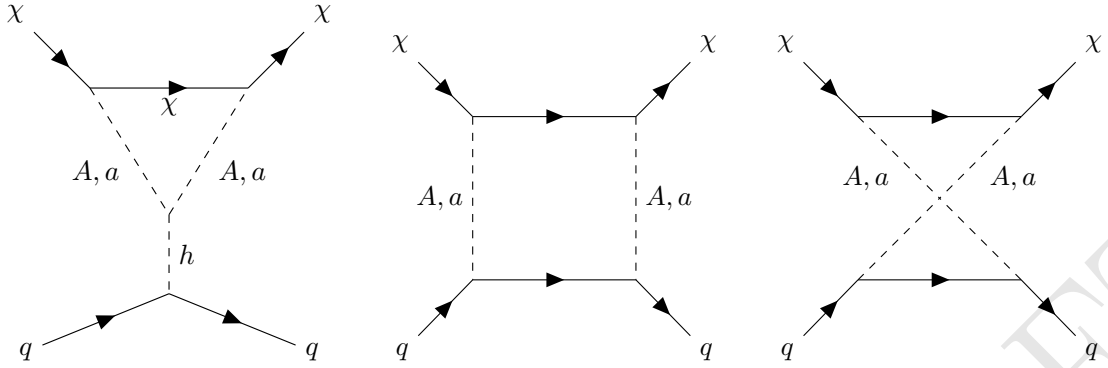


Figure 48: Spin-independent DM-nucleon scattering arises from the loop exchange of the mixing pseudoscalar mediators. Left panel: triangle diagrams. Central and right panel: box diagrams.

$$\hat{\mu}_{Aah} = -\frac{1}{4} \sin(4\theta) \left(\frac{1}{x} - \frac{1}{y} \right) + \frac{z}{2} \frac{(\hat{\lambda}_{345P} - 2\hat{\lambda}_{P_1})v^2}{m_h^2} \sin(2\theta), \quad (9.15)$$

$$\hat{\mu}_{aah} = \frac{1}{2} \sin^2(2\theta) \left(\frac{1}{x} - \frac{1}{y} \right) - z \frac{\hat{\lambda}_{34-5}v^2}{m_h^2} \sin^2 \theta + z \frac{2\hat{\lambda}_{P_1}v^2}{m_h^2} \cos^2 \theta, \quad (9.16)$$

The coefficient μ have been written under the assumption of alignment, and imposing $M_A = M_H = M_{H^+}$ and $\lambda_3 = \lambda_{P_1} = \lambda_{P_2}$, while the coefficients $\hat{\mu}$ are using no assumption other than the alignment condition. The interference structure arising from gauge invariance is only manifest in the latter case. Note that the terms proportional to z arise from the terms in the 2HDM potential proportional to $\lambda_{1,2,3,4,5,P_1,P_2}$ ⁸, and in general their coefficient will depend on all these couplings and the value of $\tan \beta$. However, here we consider two example cases: the first one, where $\hat{\lambda}_{34-5} = \hat{\lambda}_3 + \hat{\lambda}_4 - \hat{\lambda}_5 = \hat{\lambda}_1 = \frac{m_h^2}{v^2}$ and $\hat{\lambda}_{P_1} = \hat{\lambda}_{P_2} = 0$, and the second one with $\lambda_3 = \lambda_{P_1} = \lambda_{P_2} = 3$ and $\lambda_{4,5}$ set by the condition $M_H = M_A = M_{H^+}$.

DD for the pseudoscalar model are presented in Fig. 49 and 50 for the first and second benchmark point respectively. Limits are calculated using 9.6. The heavier pseudoscalar is set to $M_A = 750\text{GeV}$, and the mixing angles are fixed to $\sin \theta = 0.7$ in the left panel, $\sin \theta = 0.35$ in the right panel and $\cos \theta = 0.35$ in the bottom panel. In the first case, current limits are able to exclude the portion of parameter space with $20\text{GeV} \lesssim m_\chi \lesssim 200\text{GeV}$ and $M_a \lesssim 40\text{GeV}$. Projected limits for XENON1T and XENONnT could expand the excluded region to $10\text{GeV} \lesssim m_\chi \lesssim 1\text{TeV}$ and $M_a \lesssim 150\text{GeV}$. The presence of the neutrino floor will prevent to be able to probe this model for $M_a \gtrsim 300\text{GeV}$ or $m_\chi \gtrsim 3\text{TeV}$ with conventional DD experiments. The second case is quite similar to the first, with the limits just slightly weakened by the smaller mixing angle. In the last case, for $\cos \theta = 0.35$, current DD experiments can only probe a tiny portion of the parameter space, with $20\text{GeV} \lesssim m_\chi \lesssim 70\text{GeV}$ and $M_a \lesssim 4\text{GeV}$. We can see that indeed the whole region rules out by DD is contained in the region rules out by Higgs width constraints. Projected limits expand the range to up $M_a \sim 40\text{GeV}$ and $m_\chi \sim 400\text{GeV}$, while neutrino background makes inaccessible

⁸Relations between $\hat{\lambda}_i$ and λ_i can be found in [10].

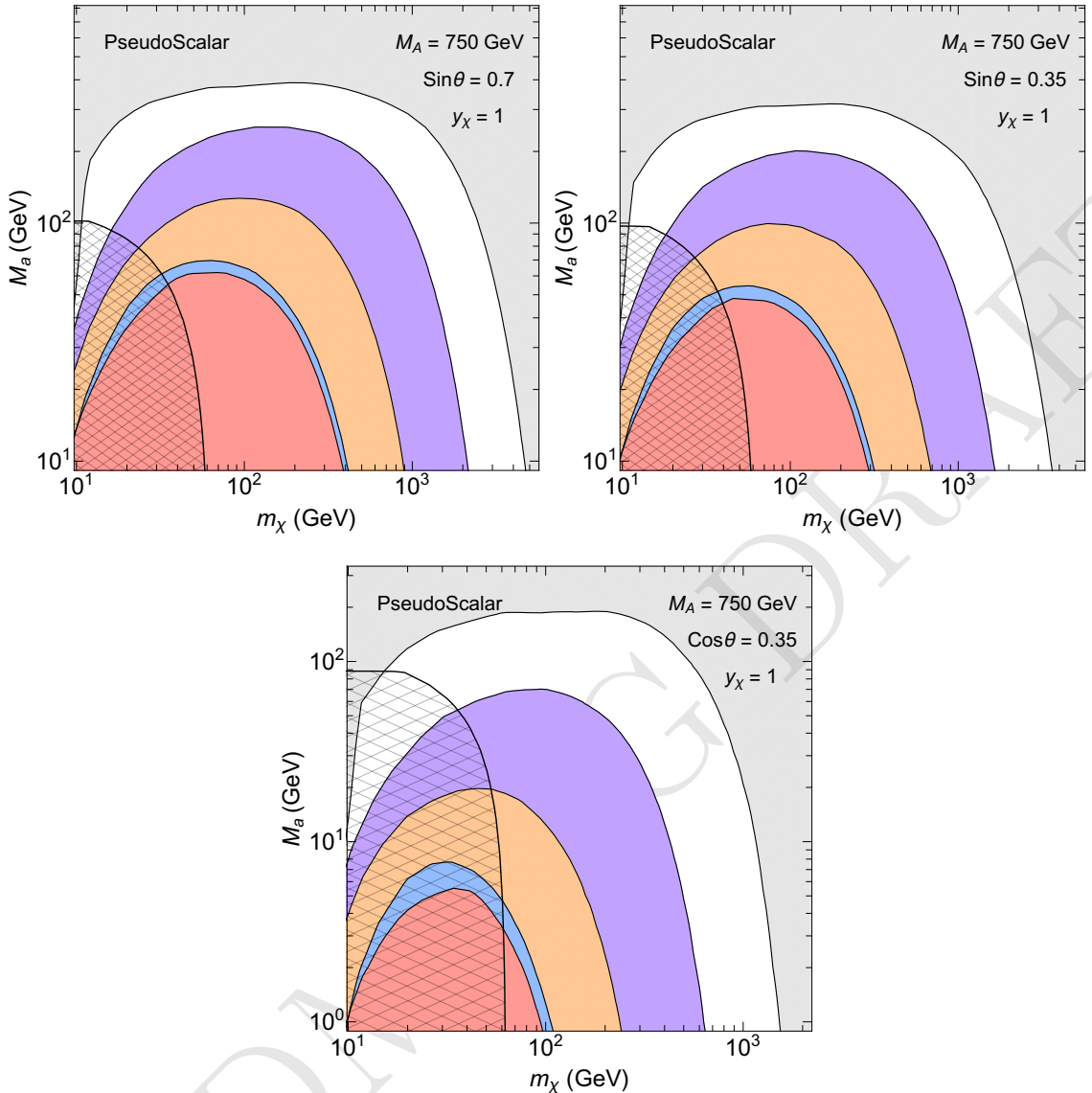


Figure 49: DD exclusion and projections for the first benchmark point for various experiments for the Pseudoscalar model. The various regions refer, in order, to LUX [45], XENON1T[46], XENON1T and XENONnT projections [47], and neutrino background [48]. Top Left panel uses $\sin \theta = 0.7$, top right panel uses $\cos \theta = 0.35$, bottom panel uses $\cos \theta = 0.35$, while $M_A = 750\text{GeV}$ in all the panels.

to DD the region beyond $M_A \gtrsim 100\text{GeV}$ or $m_\chi \gtrsim 1\text{TeV}$. In the 3 panels we also report limits from Higgs invisible BR [49, 50], coming from 2 and 3 body decays, as described in [2]. They rule out the low m_χ, M_a mass region.

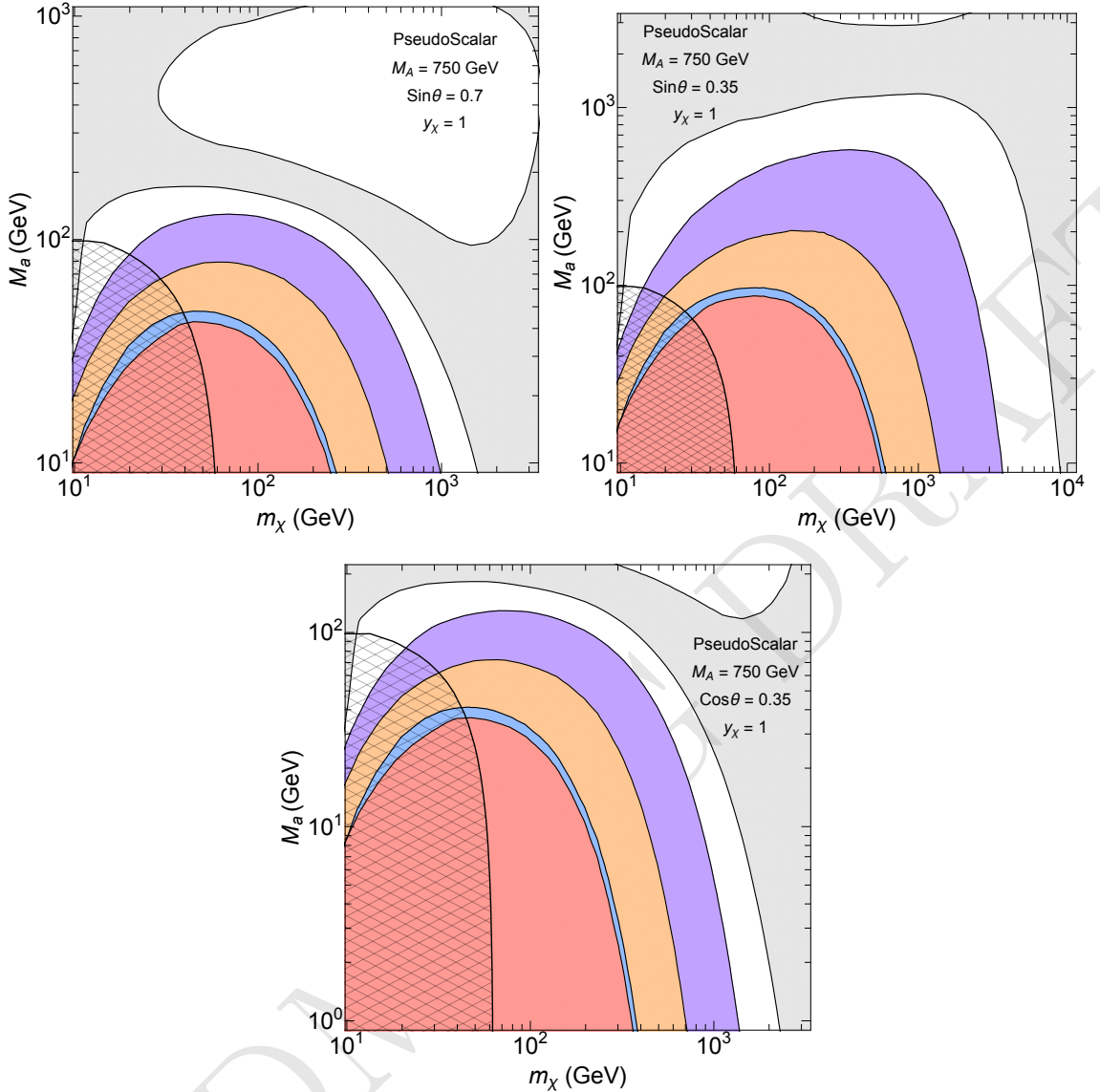


Figure 50: DD exclusion and projections for the second benchmark point for the first benchmark point for various experiments for the Pseudoscalar model. The various regions refer, in order, to LUX [45], XENON1T[46], XENON1T and XENONnT projections [47], and neutrino background [48]. Top Left panel uses $\sin \theta = 0.7$, top right panel uses $\cos \theta = 0.35$, bottom panel uses $\cos \theta = 0.35$, while $M_A = 750\text{GeV}$ in all the panels.

9.3 Indirect detection

Indirect detection signals for this model are quite complex, as an increasing number of distinct event topologies become kinematically accessible as well scan from light to heavy Dark Matter masses. Not only can the DM annihilate to various pairs of standard model particles, we see from figure 24 there are two more types distinct types of event topologies

with characteristic kinematics that change the number of final-state Standard Model particles in the event. There are processes where a single SM particle is produced in association with an unstable Higgs sector particle, and processes where two Higgs sector particles are produced which decay to 4 SM particles. Here we briefly describe the important mass thresholds involved in the processes. In many points in parameter space several annihilation channels will contribute to over-all photon flux and limits obtained from flux observation will require that these distinct spectra using a method similar to reference [53]. The total photon flux expected from DM annihilations will be

$$\Phi_\gamma = \frac{1}{4\pi} \sum_f \frac{\langle \sigma v \rangle_f}{2m_\chi^2} \int_{E_{\min}}^{E_{\max}} \left(\frac{dN_\gamma}{dE_\gamma} \right)_f dE_\gamma J, \quad (9.17)$$

where the the J -factor ($\text{GeV}^2\text{cm}^{-5}$) is the line of sight integral of the DM density ρ , integrated over a solid angle: $\Delta\Omega$, m_χ is the Dark Matter mass, and we must sum over all accessible partial annihilation rates $\langle \sigma v \rangle_f$, where f specifies the distinct final state. These predictions of total integrated flux may then be compared to observational measurements, for example of dwarf galaxies or the galactic center, which may constrain the partial annihilation rates and thus provide limits on the model parameters. In reference [53], complex models with several annihilation channels was constrained using the Fermi dwarf galaxy data, where the observations of each dwarf galaxy have stacked in a joint-likelihood analysis. Such a procedure would be optimal for setting limits on this model from existing observational data. Below we briefly describe the effect of various mass thresholds on the admixture of partial annihilation rates in our model.

For light Dark Matter masses, under about a 200 GeV threshold, the annihilation rate is dominated by b-quark pairs, as are the kinematically accessible particles that have the largest Yukawa coupling. This situation is a lot like the domination of a light Higgs boson decay rate by bottom quarks, though the Yukawa is not particularly large, it is the only non-hopeless kinematically accessible decay. A new annihilation into a Higgs and Z boson opens up when the threshold $m_{DM} \rightarrow m_h + m_Z$ is crossed. The next threshold to be crossed is $m_{DM} \rightarrow m_t$, where the di-top channel opens which may now dominate the annihilation rate. The next threshold to be crossed $2m_{DM} \rightarrow m_a + m_h$, where the light pseudo-scalar will decay to bottom quarks. The event is thus likely $2m_{DM} > 4b$, however the momentum distribution between the two pairs of bottoms will be asymmetric. It is expected that the total annihilation rate into this channel is appreciable since there is a large coupling between the Higgs and the pseudoscalar which also involves mass insertion. This type of event topology, $DM DM \rightarrow X + SM$, where X is a decaying hidden sector particle, has not been well studies on its own. New Higgs sector decays will open up as the threshold $2m_{DM} > m_V + m_H$ is crossed where V is the mass of a heavy vector boson, and H is a heavier Higgs sector field. Along with this the production models will begin to open in which the DM annihilated to two Higgs sector fields. The most important, and lowest threshold is $m_{DM} \rightarrow m_a$, where the annihilation channel into two pseudoscalars will open. After this threshold, we may cross the Threshold where DM annihilated to any pair of heavy(or one heavy and one light) Higgs sector field.

A few general notes are in order here. First, the effect of the new annihilation channels opening as thresholds are crossed may be witnesses in figure 26 which charts the relic density as a function of DM mass for fixed values of the Higgs-sector parameters. We can see, for example, the effect of the di-top channel turning on as the overall annihilation rate is enhanced and the relic density drops. We see a similar powerful effect as the threshold $2m_{DM} \rightarrow m_a + m_h$ is crossed. The dramatic drop in relic density demonstrates that this is an important annihilation channel which can compete or even dominate the list of partial annihilate rates. We also note the enhancement of the annihilate rate as the resonance thresholds $2m_{DM} = m_a, m_A$ are crossed, which will lead to stronger constraints from total photon flux measurements. Finally we note that the complexity of kinematics displayed in this model has not yet been well studies for models of DM annihilations. Some work has been done regarding shifts in the annihilation spectrum resulting a very symmetric process where DM pairs annihilate to 2 or more identical heavy states that then decay to pairs of SM particles [54]. Our model presents this as a possible annihilation process, along with others which have not yet been analysed. These include the asymmetric process where 2 decaying Higgs sector particles of differing masses are produced and other asymmetric processes where light SM particle is produced in association with a heavier Higgs sector particle. The full parameter space of this model presents a wide area of admixtures of annihilation channels, and thus many possibilities for total integrates photon spectra.

10 Conclusions

Appendix

A Details on MC generation

Mono-Higgs signature The studies of the $h(bb) + E_T^{\text{miss}}$ channel presented here are based on MC simulations with version 2.4.3 of MADGRAPH 5 [55] using a Universal Feyn-Rules Output [56] implementation of the 2HDM with a Yukawa sector of type II with DM mediator (2HDM+a), as provided by the authors of [2]. The NNPDF30_lo_as_0130 set of parton distribution functions (PDF) at leading order in the five-flavor scheme, which assumes a massless b -quark, with $\alpha_S(m_Z) = 0.130$ is used for these simulations [57]. For consistency, five-flavor scheme and $m_b = 0$ GeV are chosen for the matrix element (ME) computation in MADGRAPH 5.

The ME generated for the parton-level studies presented in the following is $gg \rightarrow h\chi\chi$ represented in ?? The only exception is the $M_a - \tan\beta$ scan which will be discussed in the following and is summarised in Figure 29. In this scan also the ME $bb \rightarrow h\chi\chi$ is generated because at high $\tan\beta$, the bb initiated process can have an amplitude of a similar magnitude as the gluon fusion initiated process from ?? [2]. The gluon fusion is dominant in all the remaining parameter space, therefore the bb initiated process and other negligible contributions are not considered explicitly for all the scans.

Table 2: Event selection requirements for the analysis of the Mono-Z signature with leptonic Z decays. The requirements are inspired to follow those used in typical experimental analyses.

Selection stage	Quantity	Requirement
Inclusive	lepton $ \eta $	< 2.5
	leading (trailing) lepton p_T	$> 25(20)$ GeV
Preselection	$ m_{ll} - m_{Z,\text{nominal}} $	< 15 GeV
	E_T^{miss}	> 40 GeV
Final selection	$\Delta\Phi(ll, E_T^{\text{miss}})$	> 2.7
	$ p_{T,ll} - E_T^{\text{miss}} /p_{T,ll}$	< 0.4
	$\Delta R(ll)$	< 1.8
	E_T^{miss}	> 80 GeV

Mono-Z signature: leptonic channel Simulated event samples for the leptonic mono-Z signature are produced with Madgraph5_aMC@NLO version 2.4.3, interfaced with Pythia version 8.2.2.6 for parton showering. The NNPDF3.0 PDF set is used at LO precision with the value of the strong coupling constant set to $\alpha_S(M_Z) = 0.130$ (NNPDF30_lo_as_0130). A five flavor scheme with a massless b-quark is used. Only contributions from gluon-gluon initial states and $l^+ l^- \chi\bar{\chi}$ final states are considered, where $l = e$ or μ . The bb initiated ME contribution is negligible for the range of $\tan\beta$ values studied. To increase calculation efficiency diagrams with an intermediate s-channel SM Higgs boson are explicitly rejected (generate $g g > xd\ xd\ l+\ l- / h1$).

Mono-Z signature: hadronic channel Simulation of mono-Z hadronic events is performed using a setup similar to that used for the leptonic events. The Madgraph5_aMC@NLO version 2.4.3, interfaced with Pythia version 8.212 for parton showering and the LO NNPDF3.0 with $\alpha_S(M_Z) = 0.130$ for PDF in the matrix element calculations, is used for the event generation. Only gluon-gluon initial states are considered for the production of mono-Z events. In contrast to the leptonic case, the Z-boson is explicitly required in the intermediate state ($g g > xd\ xd \sim z$) to ensure that non-Z hadronic events are suppressed in the produced sample. The MadSpin is used for the Z decay to maintain a proper spin correlation between the Z decay quarks.

B Additional kinematic distributions

Signatures including a Z boson

Z+ E_T^{miss} signature, leptonic channel Inclusive distributions of the invariant masses of the dilepton and $\chi\chi$ systems are shown in Figure 51 (before preselection). Independently of the parameters, the dilepton mass spectrum is centered at the Z peak, without any nonresonant contribution. The $M_{\chi\chi}$ distribution illustrates the signal contributions from different diagrams. For $M_A > M_a$, DM is dominantly produced from on-shell a bo-

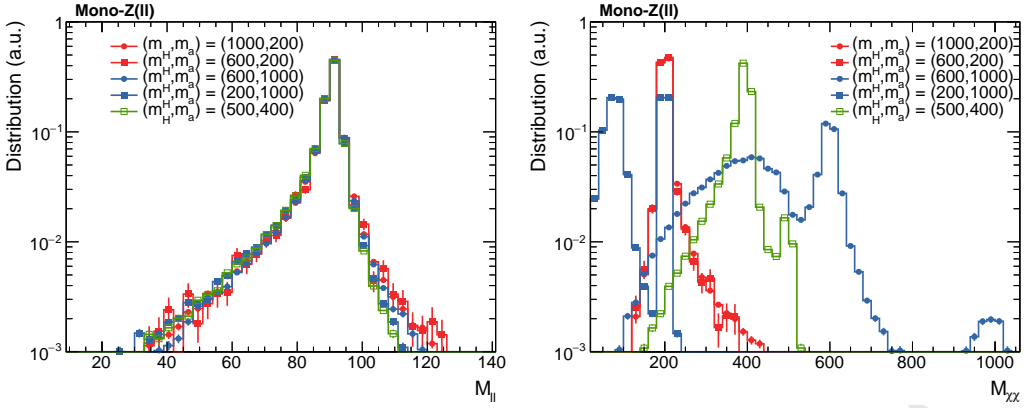


Figure 51: Distributions of the invariant mass of the dilepton (left) and $\chi\bar{\chi}$ systems (right) with no selection applied in addition to the generation cuts. The M_{ll} distribution is centered around the Z boson mass independent of the chosen parameter point, indicating that there is no contribution from γ^* exchange. The $M_{\chi\bar{\chi}}$ distribution

Table 3: Event selections used in the analysis for the mono-Z hadronic signature with $Z \rightarrow q\bar{q}$ decays. The requirements are inspired from those used in a typical experimental analysis. The j (J) stands for the small-radius (large-radius) jet in the resolved (boosted) analysis.

Selection stage	Quantity	Requirement
Inclusive resolved and boosted selections	Jet radius	$= 0.4$ (1.0)
	Jet $ \eta $	< 2.5 (2.0)
	Jet p_T	> 25 GeV (200)
	Number of jets	≥ 2 (1)
Final resolved and boosted selections	$ m_{jj \text{ or } J} - m_Z $	< 15 GeV
	$\Delta\Phi(jj \text{ or } J, E_T^{\text{miss}})$	> 2
	E_T^{miss}	> 100 (250) GeV

son production. In the inverted mass region $M_A < M_a$, the situation is reversed, and H diagrams dominate.

The distributions of some relevant variables for this search are shown in Figure 52, after preselection.

Z+ E_T^{miss} signature, hadronic channel The event selection criteria used in this analysis are listed in Table 3.

Figure 53 shows the kinematic distributions of mono-Z events after applying the inclusive selections, separately for the resolved and boosted topologies. The M_a is fixed to 250 GeV and the M_A is chosen to be 300, 600, 900 and 1200 GeV in the figure. When the M_A gets closer to M_a , the Z-boson is less boosted, causing the large-radius jet mass to be more populated at mass below ~ 30 GeV. When the $|M_A - M_a|$ becomes smaller than the Z-boson mass, the non-resonant production dominates as clearly seen in the E_T^{miss}

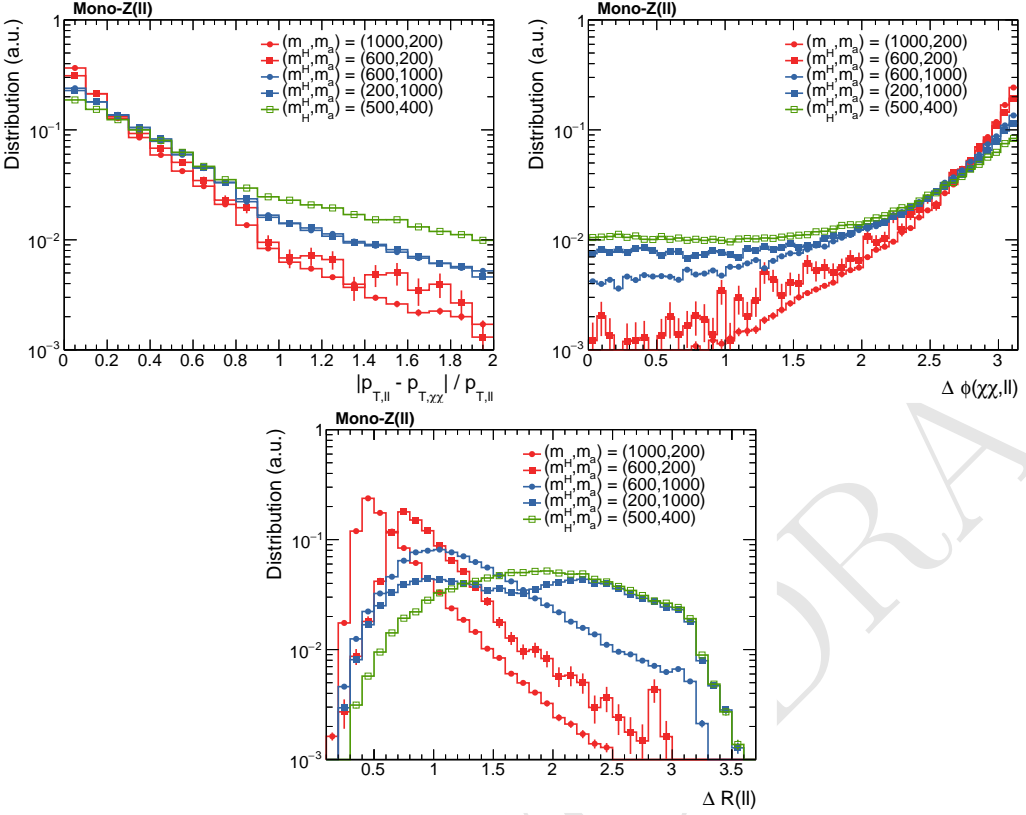


Figure 52: Distributions of the main selection variables after preselection: p_T balance (top panel), $\Delta\Phi$ (middle) and ΔR (bottom). The shown parameter points illustrate the different qualitative behavior in the three different mass regions.

spectrum for the resolved case. Figure 54 shows the same set of distributions when the M_A is fixed to 600 GeV and the M_a varies from 150 to 250, 350 and 450 GeV. The trend seen in Fig. 53 is also visible here when the M_a gets closer to M_A .

C Cross-section and acceptances for selected signatures

Signatures including a Z boson

Z+ E_T^{miss} signature, leptonic channel The overall cross-sections in the $\tan\beta$ and mass scans are shown in Fig. 55.

In the mass scan, maximal cross-sections are observed for the region of $M_a < M_A$ for values of $M_a \gtrsim 100$ GeV. Towards higher values of both M_a and M_A , the cross-sections fall off, reaching values smaller than 1 fb at $M_a \approx 450$ GeV or $M_A \approx 1.1$ TeV. In the $M_a \approx M_A$ -region, the cross-section is suppressed by destructive interference. For the region with inverted mass hierarchy $M_a > M_A$, cross-sections of the order of multiple fb are observed, as long as $|M_a - M_A|$ remains sufficiently large. In the $\tan\beta$ scan, cross-sections smoothly fall with increasing M_a as well as $\tan\beta$. Cross-sections are typically larger than 1 fb up to $\tan\beta \approx 5$. The M_a dependence is modulated by the value of $\tan\beta$: Crossing

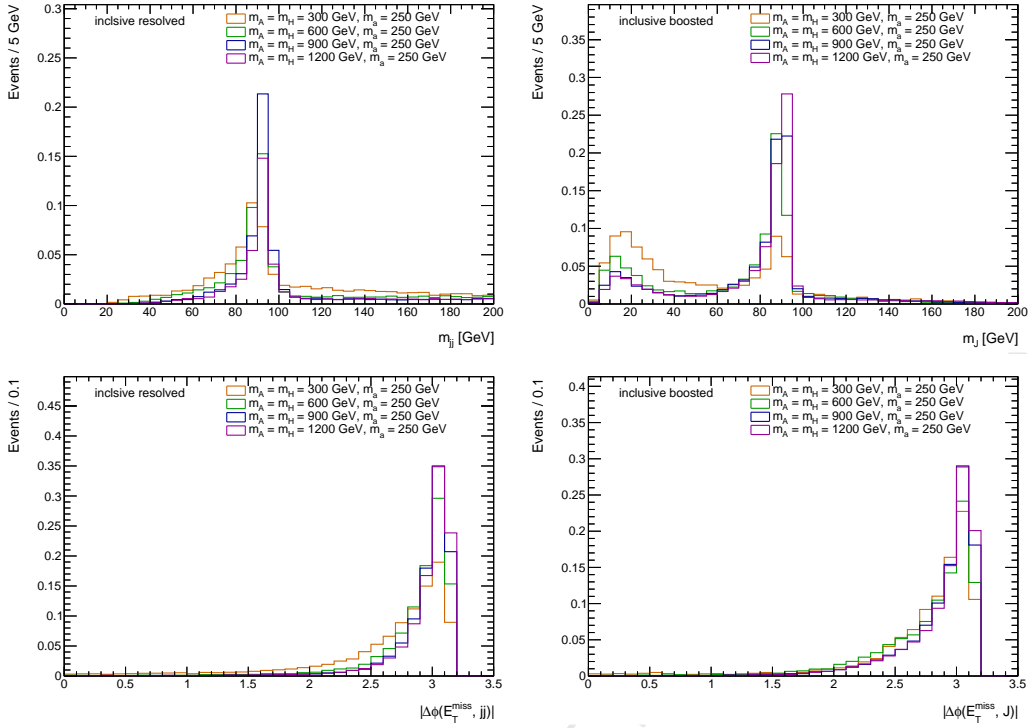


Figure 53: Dijet mass (top), $\Delta\Phi(jj, E_T^{\text{miss}})$ (bottom) distributions after applying the inclusive selections in the resolved analysis are shown on the left side. Large-radius jet mass (top), $\Delta\Phi(J, E_T^{\text{miss}})$ (bottom) distributions after applying the inclusive selections in the boosted analysis are shown on the right side. The signal masses are chosen to be $M_A = 300, 600, 900$ and 1200 GeV with the fixed $M_a = 250$ GeV.

the M_a range from 100 to 400 GeV, cross-sections are reduced by a factor ≈ 7 for small $\tan\beta \approx 1$, but only a factor ≈ 2 for higher values of $\tan\beta \approx 5$. In the $\sin\theta$ scan shown in Figure 56, cross sections depends on whether or not the $a \rightarrow \bar{t}t$ decays are accesible. For $M_a < 350$ GeV they are not accesible and cross section strictly increases with $\sin\theta$. For $M_a > 350$ GeV, the $a \rightarrow \bar{t}t$ decays become possible causing the cross section to decrease for large values of $\sin\theta$.

Z+ E_T^{miss} signature, hadronic channel Figure 57 shows the production cross-section for mono-Z events in the M_a (M_A) range between 100 and 500 GeV (200 and 1200 GeV). Shown on the left (right) is the cross-section in the M_a vs M_A (M_a vs $\tan\beta$) grid. Note that the $Z \rightarrow q\bar{q}$ branching fraction is not included in the cross-section. The production cross-section tends to vanish in the region where the M_a gets close to M_A , as shown by the empty points in the grid.

The signal acceptance for the four sets of event selections given in Table 3 is summarized in Fig. 58 in the M_a vs M_A grid. Note again that the resolved and boosted selection criteria are applied separately for the inclusive case, while for the final selections the boosted criteria are applied first and then the resolved ones to those failing the boosted criteria. For the inclusive case, the mass dependence on the acceptance is weak for the

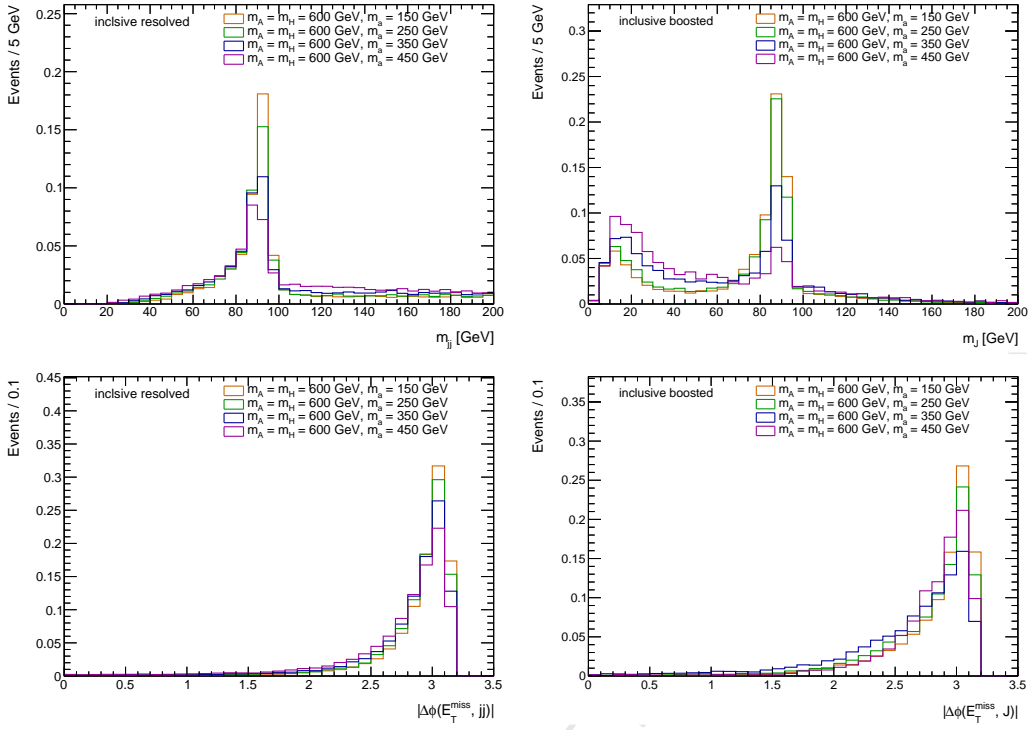


Figure 54: Dijet mass (top), $\Delta\Phi(jj, E_T^{\text{miss}})$ (bottom) distributions after applying the inclusive selections in the resolved analysis are shown on the left side. Large-radius jet mass (top), $\Delta\Phi(J, E_T^{\text{miss}})$ (bottom) distributions after applying the inclusive selections in the boosted analysis are shown on the right side. The signal masses are chosen to be $M_a = 150, 250, 350$ and 450 GeV with the fixed $M_A = 600 \text{ GeV}$.

resolved criteria while it is rather significant for the boosted criteria as the Z -boson is less boosted with decreasing M_A and hence less likely that the Z -decay products are merged into a single jet. The final boosted selections have acceptance larger than $\sim 20\%$ (40%) at $M_A > 800$ (1000) GeV and $M_a < 400 \text{ GeV}$. The final resolved selections can recover 10–20% of signal events which fail the boosted criteria in the same mass regions. At $M_A < 600 \text{ GeV}$ the signal acceptance is dominated by the resolved selection criteria.

The signal acceptance in the M_a vs $\tan\beta$ space is shown in Fig. 59. The conventions used in Fig. 59 are the same as those in Fig. 58. The signal acceptance is rather independent of $\tan\beta$ except at low $\tan\beta$ region; the acceptance tends to be slightly lower at $\tan\beta < 1$ than at > 1 for $M_a < \sim 250 \text{ GeV}$ while it's opposite for $M_a > \sim 250 \text{ GeV}$. The acceptance decreases with increasing M_a because the E_T^{miss} spectrum becomes softer with M_a , as shown in Fig. 54.

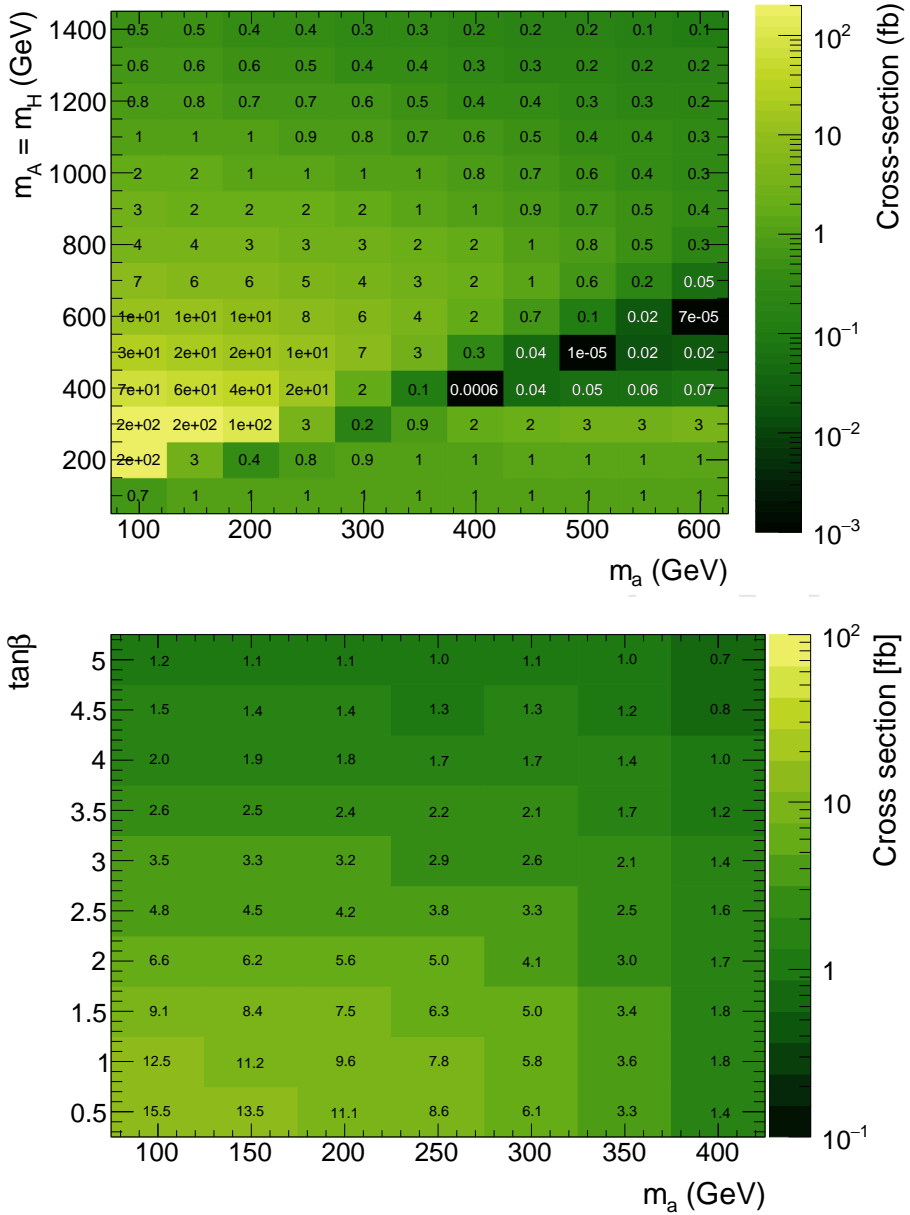


Figure 55: Inclusive cross-sections for $pp \rightarrow l^+l^-\chi\bar{\chi}$ in the M_a - M_A (top) and M_a - $\tan\beta$ scans (bottom).

D Studies of other models of scalar sector

E Inert Doublet Model

The Inert Doublet model [58–60] is another intriguing model that extends the scalar sector of the Standard Model, providing dark matter candidates. It contains two scalar doublets Φ_S, Φ_D , redressing five physical states h, H, H^\pm, A , where h corresponds to the Standard Model Higgs particle and all other states originate from the second doublet. An additional

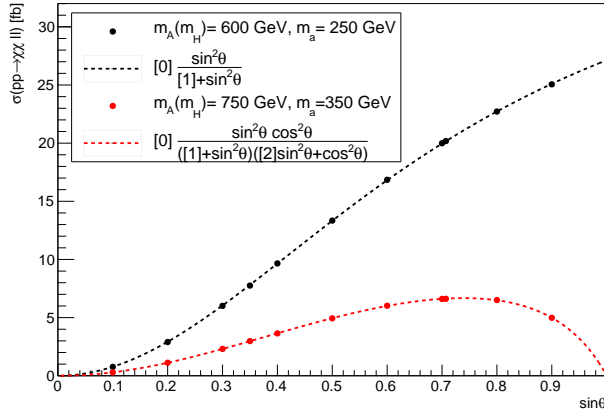


Figure 56: For two different mass points, this figure shows the cross section $pp \rightarrow \chi\chi\ell\ell$ as a function of $\sin \theta$. For $M_a < 350$ GeV, a decays solely to dark matter particles. As a consequence, the mixing angle only impacts the heavy scalar's branching fraction to aZ and cross section strictly increases with $\sin \theta$. For M_a above 350 GeV, $t\bar{t}$ decays become accessible, introducing additional $\sin \theta$ and $\cos \theta$ dependences for the branching fraction of $a \rightarrow \chi\chi$. For M_a above 350 GeV for large values of $\sin \theta$, there is a turnover point where the reduced $a \rightarrow \chi\chi$ branching fraction outweighs the increased $H \rightarrow aZ$ branching and the net cross section decreases.

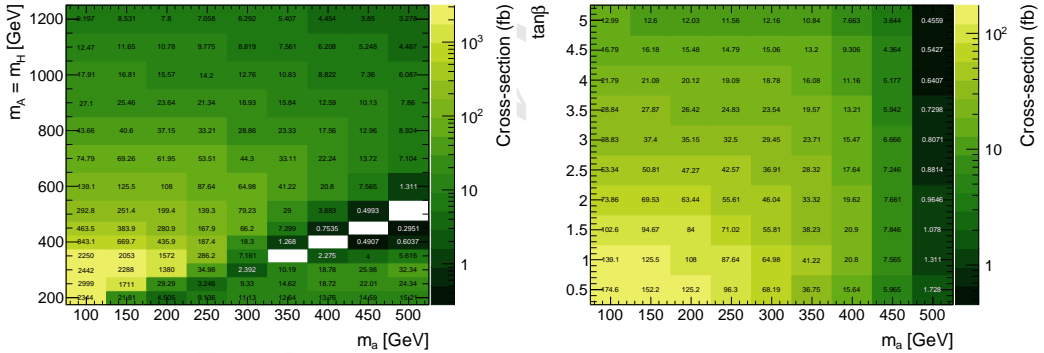


Figure 57: Inclusive cross-sections for the mono- Z hadronic events $pp \rightarrow Z(\rightarrow q\bar{q})\chi\bar{\chi}$ in the M_a vs M_A (left) and M_a vs $\tan \beta$ (right) grids. The $Z \rightarrow q\bar{q}$ branching fraction is not included in the cross-section.

Z_2 symmetry is imposed, with the discrete transformations defined as $\phi_D \rightarrow -\phi_D$, $\phi_S \rightarrow \phi_S$, SM \rightarrow SM. This leads to the following potential.

$$V = -\frac{1}{2} \left[m_{11}^2 (\phi_S^\dagger \phi_S) + m_{22}^2 (\phi_D^\dagger \phi_D) \right] + \frac{\lambda_1}{2} (\phi_S^\dagger \phi_S)^2 + \frac{\lambda_2}{2} (\phi_D^\dagger \phi_D)^2 + \lambda_3 (\phi_S^\dagger \phi_S) (\phi_D^\dagger \phi_D) + \lambda_4 (\phi_S^\dagger \phi_D) (\phi_D^\dagger \phi_S) + \frac{\lambda_5}{2} \left[(\phi_S^\dagger \phi_D)^2 + (\phi_D^\dagger \phi_S)^2 \right], \quad (\text{E.1})$$

with all parameters real (see e.g. [61]). After minimization, the model contains in total 7 free parameters which e.g. can be chosen as $(m_H, m_A, m_{H^\pm}, \lambda_2, \lambda_{345})$, where $\lambda_{345} \equiv \lambda_3 +$

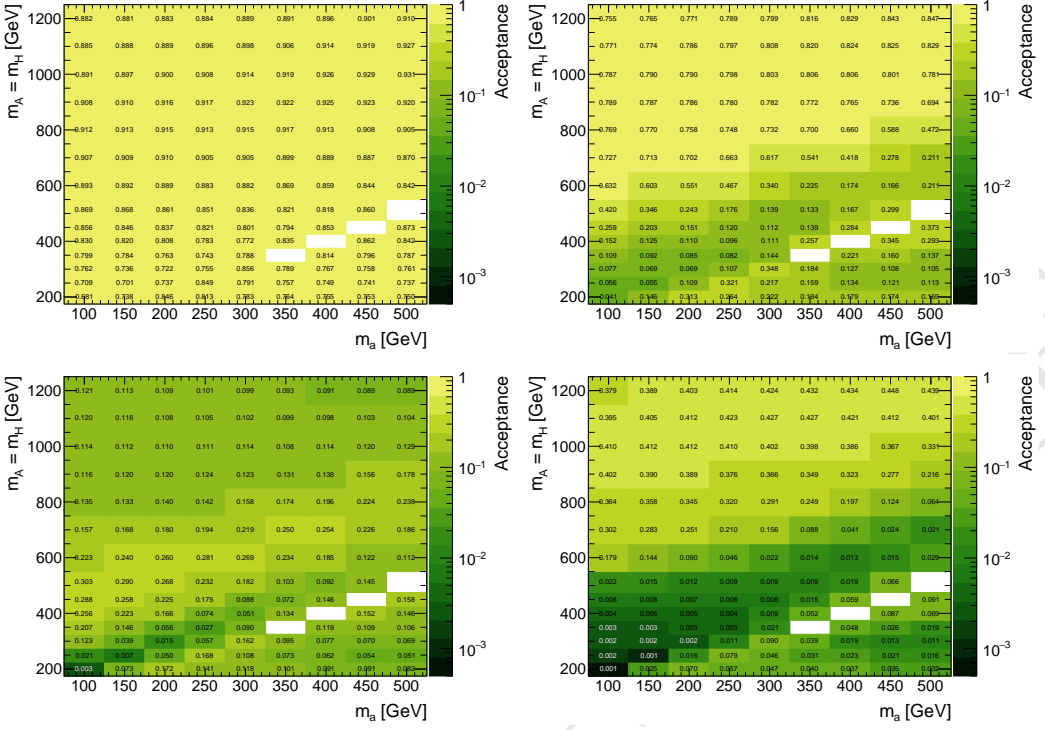


Figure 58: Acceptance for the inclusive (top) and final (bottom) selections for the mono- Z hadronic events $pp \rightarrow Z(\rightarrow q\bar{q})\chi\bar{\chi}$ in the M_a vs M_A grid. Shown on the left (right) is the acceptance for the resolved (boosted) analysis selections.

$\lambda_4 + \lambda_5$. The above Z_2 symmetry renders the lightest of the additional scalars stable, and the model therefore provides a good dark matter candidate. The following discussion focuses on H as the dark matter candidate. The model is subject to a large number of theoretical and experimental constraints, cf. e.g. [62–71] for recent discussions on the allowed parameter space. Most stringent constraints stem from direct detection experiments such as LUX [45] for large parts of the parameter space.

Due to the Z_2 symmetry, all scalars that originate from the second (dark) doublet can only be pair-produced. In addition, these dark scalars do not couple to fermions. The most prominent production channels are therefore Drell-Yan induced processes, i.e. the production of a single W or Z in the s-channel producing a pair of dark scalars. In principle AA final states can also be mediated via an h in the s-channel; however, the according couplings are strongly constrained from direct detection experiments, rendering the according contribution to the total cross section negligible. Therefore, the production cross sections for this model only depend on electroweak couplings as well as the masses of the produced dark scalars. Similarly, the dark scalars dominantly decay via $A \rightarrow ZH$ and $H^\pm \rightarrow W^\pm H$, with electroweak gauge bosons following SM decay patterns.

Total cross sections for scans as well as dedicated parameter points have been presented in [66, 68, 69]. Typical production cross sections for $Z + E_T^{\text{miss}}$ or $W^\pm + E_T^{\text{miss}}$ at the 13 TeV LHC are of the order of 30 fb, where no cuts have been applied. Production cross

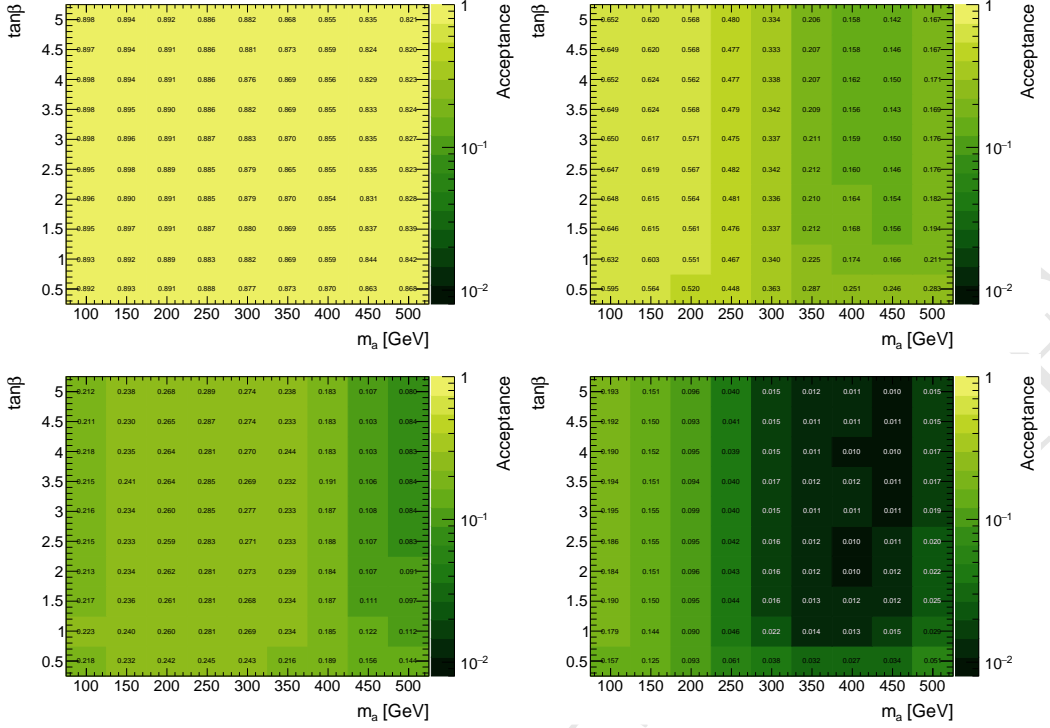


Figure 59: Acceptance for the inclusive (top) and final (bottom) selections for the mono- Z hadronic events $pp \rightarrow Z(\rightarrow q\bar{q})\chi\bar{\chi}$ in the M_a vs $\tan\beta$ grid. Shown on the left (right) is the acceptance for the resolved (boosted) analysis selections. The M_A is fixed to 600 GeV.

sections for diboson final states and E_T^{miss} are suppressed by an additional factor 3-10⁹.

The UFO model file for the Inert Doublet Model has been presented in [72] and can readily be interfaced with Madgraph to produce event samples at all levels. Collider studies of this model at the LHC as well as a Linear Collider framework have e.g. been discussed in [64, 73–77].

For the most dominant production channels, i.e. mono gauge-boson production with missing energy, the production mode differs from the model discussed above, cf. Figure 60 (the diagram for $H^\pm H$ production is analogous). Both the nature of the s-channel mediator as well as the decay topology differ. Therefore, although final state signatures are identical within the two models, it can be expected that different selection cuts need to be applied for signal enhancement. Possible search strategies can e.g. be adopted from improvements of experimental cuts for supersymmetric searches in multilepton final states (see [78] for a recast of this model using 8 TeV LHC data).

⁹In principle, also monojet searches could render insight on this model. However, the according production cross sections are proportional to λ_{345}^2 . The value of this parameter is highly constrained by direct detection experiments.

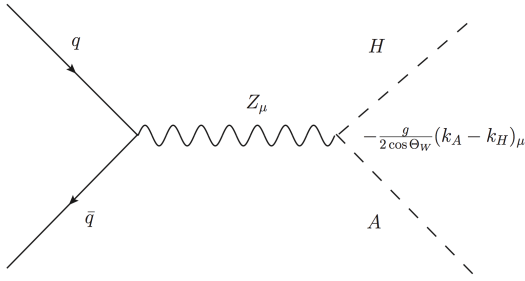


Figure 60: Feynman diagram for $Z + E_T^{\text{miss}}$ final states in the inert doublet model from HA production at a hadron collider, with $A \rightarrow ZH$. Production and decay are determined by electroweak SM couplings and masses m_A, m_H .

References

- [1] D. Abercrombie et al., *Dark Matter Benchmark Models for Early LHC Run-2 Searches: Report of the ATLAS/CMS Dark Matter Forum*, [arXiv:1507.00966](https://arxiv.org/abs/1507.00966).
- [2] M. Bauer, U. Haisch, and F. Kahlhoefer, *Simplified dark matter models with two Higgs doublets: I. Pseudoscalar mediators*, *JHEP* **05** (2017) 138, [[arXiv:1701.07427](https://arxiv.org/abs/1701.07427)].
- [3] N. F. Bell, G. Busoni, and I. W. Sanderson, *Self-consistent Dark Matter Simplified Models with an s-channel scalar mediator*, *JCAP* **1703** (2017), no. 03 015, [[arXiv:1612.03475](https://arxiv.org/abs/1612.03475)].
- [4] S. Ipek, D. McKeen, and A. E. Nelson, *A Renormalizable Model for the Galactic Center Gamma Ray Excess from Dark Matter Annihilation*, *Phys. Rev.* **D90** (2014), no. 5 055021, [[arXiv:1404.3716](https://arxiv.org/abs/1404.3716)].
- [5] J. M. No, *Looking through the pseudoscalar portal into dark matter: Novel mono-Higgs and mono-Z signatures at the LHC*, *Phys. Rev.* **D93** (2016), no. 3 031701, [[arXiv:1509.01110](https://arxiv.org/abs/1509.01110)].
- [6] D. Goncalves, P. A. N. Machado, and J. M. No, *Simplified Models for Dark Matter Face their Consistent Completions*, [arXiv:1611.04593](https://arxiv.org/abs/1611.04593).
- [7] M. Beltran, D. Hooper, E. W. Kolb, Z. A. Krusberg, and T. M. Tait, *Maverick dark matter at colliders*, *JHEP* **1009** (2010) 037, [[arXiv:1002.4137](https://arxiv.org/abs/1002.4137)].
- [8] P. J. Fox, R. Harnik, J. Kopp, and Y. Tsai, *Missing Energy Signatures of Dark Matter at the LHC*, *Phys. Rev.* **D85** (2012) 056011, [[arXiv:1109.4398](https://arxiv.org/abs/1109.4398)].
- [9] J. Goodman, M. Ibe, A. Rajaraman, W. Shepherd, T. M. Tait, et al., *Constraints on Dark Matter from Colliders*, *Phys. Rev.* **D82** (2010) 116010, [[arXiv:1008.1783](https://arxiv.org/abs/1008.1783)].
- [10] N. F. Bell, G. Busoni, and I. W. Sanderson, *Two Higgs Doublet Dark Matter Portal*, [arXiv:1710.10764](https://arxiv.org/abs/1710.10764).
- [11] A. Pich and P. Tuzon, *Yukawa Alignment in the Two-Higgs-Doublet Model*, *Phys. Rev.* **D80** (2009) 091702, [[arXiv:0908.1554](https://arxiv.org/abs/0908.1554)].
- [12] P. Tuzon and A. Pich, *The Aligned two-Higgs Doublet model*, *Acta Phys. Polon. Supp.* **3** (2010) 215–220, [[arXiv:1001.0293](https://arxiv.org/abs/1001.0293)].

- [13] A. Pich, *Flavour constraints on multi-Higgs-doublet models: Yukawa alignment*, *Nucl. Phys. Proc. Suppl.* **209** (2010) 182–187, [[arXiv:1010.5217](#)].
- [14] A. Peuelas and A. Pich, *Flavour alignment in multi-Higgs-doublet models*, [arXiv:1710.02040](#).
- [15] S. Gori, H. E. Haber, and E. Santos, *High scale flavor alignment in two-Higgs doublet models and its phenomenology*, *JHEP* **06** (2017) 110, [[arXiv:1703.05873](#)].
- [16] J. F. Gunion and H. E. Haber, *The CP conserving two Higgs doublet model: The Approach to the decoupling limit*, *Phys. Rev.* **D67** (2003) 075019, [[hep-ph/0207010](#)].
- [17] A. Barroso, P. M. Ferreira, I. P. Ivanov, and R. Santos, *Metastability bounds on the two Higgs doublet model*, *JHEP* **06** (2013) 045, [[arXiv:1303.5098](#)].
- [18] I. F. Ginzburg and I. P. Ivanov, *Tree-level unitarity constraints in the most general 2HDM*, *Phys. Rev.* **D72** (2005) 115010, [[hep-ph/0508020](#)].
- [19] B. Grinstein, C. W. Murphy, and P. Uttayarat, *One-loop corrections to the perturbative unitarity bounds in the CP-conserving two-Higgs doublet model with a softly broken \mathbb{Z}_2 symmetry*, *JHEP* **06** (2016) 070, [[arXiv:1512.04567](#)].
- [20] F. Staub, *Reopen parameter regions in Two-Higgs Doublet Models*, [arXiv:1705.03677](#).
- [21] **ATLAS** Collaboration, G. Aad et al., *Observation of a new particle in the search for the Standard Model Higgs boson with the ATLAS detector at the LHC*, *Phys. Lett.* **B716** (2012) 1–29, [[arXiv:1207.7214](#)].
- [22] **CMS** Collaboration, S. Chatrchyan et al., *Observation of a new boson at a mass of 125 GeV with the CMS experiment at the LHC*, *Phys. Lett.* **B716** (2012) 30–61, [[arXiv:1207.7235](#)].
- [23] L. Carpenter, A. DiFranzo, M. Mulhearn, C. Shimmin, S. Tulin, et al., *Mono-Higgs: a new collider probe of dark matter*, *Phys. Rev.* **D89** (2014) 075017, [[arXiv:1312.2592](#)].
- [24] A. A. Petrov and W. Shepherd, *Searching for dark matter at LHC with Mono-Higgs production*, *Phys. Lett.* **B730** (2014) 178–183, [[arXiv:1311.1511](#)].
- [25] **ATLAS** Collaboration, M. Aaboud et al., *Search for Dark Matter Produced in Association with a Higgs Boson Decaying to $b\bar{b}$ using 36 fb^{-1} of pp collisions at $\sqrt{s} = 13 \text{ TeV}$ with the ATLAS Detector*, [arXiv:1707.01302](#).
- [26] **ATLAS** Collaboration, M. Aaboud et al., *Search for dark matter in association with a Higgs boson decaying to two photons at $\sqrt{s} = 13 \text{ TeV}$ with the ATLAS detector*, [arXiv:1706.03948](#).
- [27] L. M. Carpenter, A. Nelson, C. Shimmin, T. M. Tait, and D. Whiteson, *Collider searches for dark matter in events with a Z boson and missing energy*, [arXiv:1212.3352](#).
- [28] N. F. Bell, J. B. Dent, A. J. Galea, T. D. Jacques, L. M. Krauss, et al., *Searching for dark matter at the LHC with a mono-Z*, *Phys. Rev.* **D86** (2012) 096011, [[arXiv:1209.0231](#)].
- [29] **ATLAS** Collaboration, M. Aaboud et al., *Search for an invisibly decaying Higgs boson or dark matter candidates produced in association with a Z boson in pp collisions at $\sqrt{s} = 13 \text{ TeV}$ with the ATLAS detector*, *Phys. Lett.* **B776** (2018) 318–337, [[arXiv:1708.09624](#)].
- [30] **CMS** Collaboration, A. M. Sirunyan et al., *Search for new physics in events with a leptonically decaying Z boson and a large transverse momentum imbalance in proton-proton collisions at $\sqrt{s} = 13 \text{ TeV}$* , [arXiv:1711.00431](#).
- [31] U. Haisch, F. Kahlhoefer, and J. Unwin, *The impact of heavy-quark loops on LHC dark matter searches*, *JHEP* **1307** (2013) 125, [[arXiv:1208.4605](#)].

- [32] M. Backovic, M. Krämer, F. Maltoni, A. Martini, K. Mawatari, and M. Pellen, *Higher-order QCD predictions for dark matter production at the LHC in simplified models with s-channel mediators*, *Eur. Phys. J.* **C75** (2015), no. 10 482, [[arXiv:1508.05327](#)].
- [33] U. Haisch, P. Pani, and G. Polesello, *Determining the CP nature of spin-0 mediators in associated production of dark matter and $t\bar{t}$ pairs*, [[arXiv:1611.09841](#)].
- [34] T. Gleisberg, S. Hoeche, F. Krauss, M. Schonherr, S. Schumann, F. Siegert, and J. Winter, *Event generation with SHERPA 1.1*, *JHEP* **02** (2009) 007, [[arXiv:0811.4622](#)].
- [35] G. Cowan, *Discovery sensitivity for a counting experiment with background uncertainty*, tech. rep., Royal Holloway, London, (2012). Available [online] <http://www.pp.rhul.ac.uk/~cowan/stat/medsig/medsigNote.pdf>.
- [36] M. Backovic, K. Kong, and M. McCaskey, *MadDM v.1.0: Computation of Dark Matter Relic Abundance Using MadGraph5*, *Physics of the Dark Universe* **5-6** (2014) 18–28, [[arXiv:1308.4955](#)].
- [37] M. Backovic, A. Martini, O. Mattelaer, K. Kong, and G. Mohlabeng, *Direct Detection of Dark Matter with MadDM v.2.0*, *Phys. Dark Univ.* **9-10** (2015) 37–50, [[arXiv:1505.04190](#)].
- [38] N. D. Christensen and C. Duhr, *FeynRules - Feynman rules made easy*, *Comput. Phys. Commun.* **180** (2009) 1614–1641, [[arXiv:0806.4194](#)].
- [39] A. Alloul, N. D. Christensen, C. Degrande, C. Duhr, and B. Fuks, *FeynRules 2.0 - A complete toolbox for tree-level phenomenology*, *Comput. Phys. Commun.* **185** (2014) 2250–2300, [[arXiv:1310.1921](#)].
- [40] N. D. Christensen, P. de Aquino, C. Degrande, C. Duhr, B. Fuks, M. Herquet, F. Maltoni, and S. Schumann, *A Comprehensive approach to new physics simulations*, *Eur. Phys. J.* **C71** (2011) 1541, [[arXiv:0906.2474](#)].
- [41] D. Barducci, G. Belanger, J. Bernon, F. Boudjema, J. Da Silva, S. Kraml, U. Laa, and A. Pukhov, *Collider limits on new physics within micrOMEGAs4.3*, [[arXiv:1606.03834](#)].
- [42] J. L. Feng, M. Kaplinghat, and H.-B. Yu, *Sommerfeld Enhancements for Thermal Relic Dark Matter*, *Phys. Rev.* **D82** (2010) 083525, [[arXiv:1005.4678](#)].
- [43] S. Cassel, *Sommerfeld factor for arbitrary partial wave processes*, *J. Phys.* **G37** (2010) 105009, [[arXiv:0903.5307](#)].
- [44] R. Iengo, *Sommerfeld enhancement: General results from field theory diagrams*, *JHEP* **05** (2009) 024, [[arXiv:0902.0688](#)].
- [45] **LUX** Collaboration, D. S. Akerib et al., *Results from a search for dark matter in the complete LUX exposure*, *Phys. Rev. Lett.* **118** (2017), no. 2 021303, [[arXiv:1608.07648](#)].
- [46] **XENON** Collaboration, E. Aprile et al., *First Dark Matter Search Results from the XENON1T Experiment*, [[arXiv:1705.06655](#)].
- [47] **XENON** Collaboration, E. Aprile et al., *Physics reach of the XENON1T dark matter experiment*, *JCAP* **1604** (2016), no. 04 027, [[arXiv:1512.07501](#)].
- [48] J. Billard, L. Strigari, and E. Figueroa-Feliciano, *Implication of neutrino backgrounds on the reach of next generation dark matter direct detection experiments*, *Phys. Rev.* **D89** (2014), no. 2 023524, [[arXiv:1307.5458](#)].
- [49] **ATLAS** Collaboration, G. Aad et al., *Constraints on new phenomena via Higgs boson*

- couplings and invisible decays with the ATLAS detector*, *JHEP* **11** (2015) 206, [[arXiv:1509.00672](#)].
- [50] CMS Collaboration, V. Khachatryan et al., *Searches for invisible decays of the Higgs boson in pp collisions at $\sqrt{s} = 7, 8,$ and 13 TeV*, *JHEP* **02** (2017) 135, [[arXiv:1610.09218](#)].
- [51] M. Cirelli, E. Del Nobile, and P. Panci, *Tools for model-independent bounds in direct dark matter searches*, *JCAP* **1310** (2013) 019, [[arXiv:1307.5955](#)].
- [52] P. Gondolo, J. Edsjo, P. Ullio, L. Bergstrom, M. Schelke, and E. A. Baltz, *DarkSUSY: Computing supersymmetric dark matter properties numerically*, *JCAP* **0407** (2004) 008, [[astro-ph/0406204](#)].
- [53] L. M. Carpenter, R. Colburn, J. Goodman, and T. Linden, *Indirect Detection Constraints on s and t Channel Simplified Models of Dark Matter*, *Phys. Rev.* **D94** (2016), no. 5 055027, [[arXiv:1606.04138](#)].
- [54] G. Elor, N. L. Rodd, T. R. Slatyer, and W. Xue, *Model-Independent Indirect Detection Constraints on Hidden Sector Dark Matter*, *JCAP* **1606** (2016), no. 06 024, [[arXiv:1511.08787](#)].
- [55] J. Alwall, R. Frederix, S. Frixione, V. Hirschi, F. Maltoni, O. Mattelaer, H. S. Shao, T. Stelzer, P. Torrielli, and M. Zaro, *The automated computation of tree-level and next-to-leading order differential cross sections, and their matching to parton shower simulations*, *JHEP* **07** (2014) 079, [[arXiv:1405.0301](#)].
- [56] C. Degrande, C. Duhr, B. Fuks, D. Grellscheid, O. Mattelaer, and T. Reiter, *UFO - The Universal FeynRules Output*, *Comput. Phys. Commun.* **183** (2012) 1201–1214, [[arXiv:1108.2040](#)].
- [57] NNPDF Collaboration, R. D. Ball et al., *Parton distributions for the LHC Run II*, *JHEP* **04** (2015) 040, [[arXiv:1410.8849](#)].
- [58] N. G. Deshpande and E. Ma, *Pattern of Symmetry Breaking with Two Higgs Doublets*, *Phys. Rev.* **D18** (1978) 2574.
- [59] Q.-H. Cao, E. Ma, and G. Rajasekaran, *Observing the Dark Scalar Doublet and its Impact on the Standard-Model Higgs Boson at Colliders*, *Phys. Rev.* **D76** (2007) 095011, [[arXiv:0708.2939](#)].
- [60] R. Barbieri, L. J. Hall, and V. S. Rychkov, *Improved naturalness with a heavy Higgs: An Alternative road to LHC physics*, *Phys.Rev.* **D74** (2006) 015007, [[hep-ph/0603188](#)].
- [61] I. Ginzburg, K. Kanishev, M. Krawczyk, and D. Sokolowska, *Evolution of Universe to the present inert phase*, *Phys.Rev.* **D82** (2010) 123533, [[arXiv:1009.4593](#)].
- [62] E. Dolle, X. Miao, S. Su, and B. Thomas, *Dilepton Signals in the Inert Doublet Model*, *Phys.Rev.* **D81** (2010) 035003, [[arXiv:0909.3094](#)].
- [63] B. Swiezewska and M. Krawczyk, *Diphoton rate in the inert doublet model with a 125 GeV Higgs boson*, *Phys.Rev.* **D88** (2013), no. 3 035019, [[arXiv:1212.4100](#)].
- [64] A. Arhrib, Y.-L. S. Tsai, Q. Yuan, and T.-C. Yuan, *An Updated Analysis of Inert Higgs Doublet Model in light of the Recent Results from LUX, PLANCK, AMS-02 and LHC*, *JCAP* **1406** (2014) 030, [[arXiv:1310.0358](#)].
- [65] M. Krawczyk, D. Sokolowska, P. Swaczyna, and B. Swiezewska, *Constraining Inert Dark Matter by $R_{\gamma\gamma}$ and WMAP data*, *JHEP* **1309** (2013) 055, [[arXiv:1305.6266](#)].

- [66] A. Ilnicka, M. Krawczyk, and T. Robens, *Inert Doublet Model in light of LHC Run I and astrophysical data*, *Phys. Rev.* **D93** (2016), no. 5 055026, [[arXiv:1508.01671](#)].
- [67] M. A. Diaz, B. Koch, and S. Urrutia-Quiroga, *Constraints to Dark Matter from Inert Higgs Doublet Model*, *Adv. High Energy Phys.* **2016** (2016) 8278375, [[arXiv:1511.04429](#)].
- [68] **LHC Higgs Cross Section Working Group** Collaboration, D. de Florian et al., *Handbook of LHC Higgs Cross Sections: 4. Deciphering the Nature of the Higgs Sector*, [arXiv:1610.07922](#).
- [69] A. Belyaev, G. Cacciapaglia, I. P. Ivanov, F. Rojas, and M. Thomas, *Anatomy of the Inert Two Higgs Doublet Model in the light of the LHC and non-LHC Dark Matter Searches*, [arXiv:1612.00511](#).
- [70] A. Ilnicka, M. Krawczyk, T. Robens, and D. Sokolowska, *IDM and not only*, *PoS CORFU2016* (2017) 030, [[arXiv:1705.00225](#)].
- [71] B. Eiteneuer, A. Goudelis, and J. Heisig, *The inert doublet model in the light of Fermi-LAT gamma-ray data: a global fit analysis*, *Eur. Phys. J.* **C77** (2017), no. 9 624, [[arXiv:1705.01458](#)].
- [72] A. Goudelis, B. Herrmann, and O. Stal, *Dark matter in the Inert Doublet Model after the discovery of a Higgs-like boson at the LHC*, *JHEP* **1309** (2013) 106, [[arXiv:1303.3010](#)].
- [73] M. Gustafsson, S. Rydbeck, L. Lopez-Honorez, and E. Lundstrom, *Status of the Inert Doublet Model and the Role of multileptons at the LHC*, *Phys. Rev.* **D86** (2012) 075019, [[arXiv:1206.6316](#)].
- [74] M. Hashemi, M. Krawczyk, S. Najjari, and A. F. arnecki, *Production of Inert Scalars at the high energy e^+e^- colliders*, [arXiv:1512.01175](#). [JHEP02,187(2016)].
- [75] P. Poulose, S. Sahoo, and K. Sridhar, *Exploring the Inert Doublet Model through the dijet plus missing transverse energy channel at the LHC*, *Phys. Lett.* **B765** (2017) 300–306, [[arXiv:1604.03045](#)].
- [76] A. Datta, N. Ganguly, N. Khan, and S. Rakshit, *Exploring collider signatures of the inert Higgs doublet model*, *Phys. Rev.* **D95** (2017), no. 1 015017, [[arXiv:1610.00648](#)].
- [77] M. Hashemi and S. Najjari, *Observability of Inert Scalars at the LHC*, *Eur. Phys. J.* **C77** (2017), no. 9 592, [[arXiv:1611.07827](#)].
- [78] G. Belanger, B. Dumont, A. Goudelis, B. Herrmann, S. Kraml, and D. Sengupta, *Dilepton constraints in the Inert Doublet Model from Run 1 of the LHC*, *Phys. Rev.* **D91** (2015), no. 11 115011, [[arXiv:1503.07367](#)].